Cyrano Bergmann

Development and Test of a Transition Radiation Detector Prototype for CBM @ FAIR

- 2009 -

Experimentelle Physik

Aufbau und Funktionstest eines TRD Prototypen für CBM @ FAIR

Diplomarbeit
von
Cyrano Bergmann

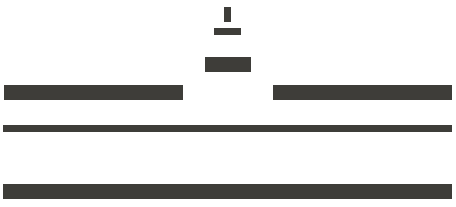

Westfälische
Wilhelms-Universität
Münster

- 2009 -

Contents

1. Facility for Antiproton and Ion Research

The **F**acility for **A**ntiproton and **I**on **R**esearch (FAIR) laboratory is designed to perform research in plasma physics, nuclear structure physics, biophysics, and medical science. FAIR will provide extremely high beam intensities compared to existing nuclear physics experiments at the same energy. The aim is to push the boundary of primary beam intensity by a factor of several hundred for the heaviest ions compared to present GSI beam intensity and energy.

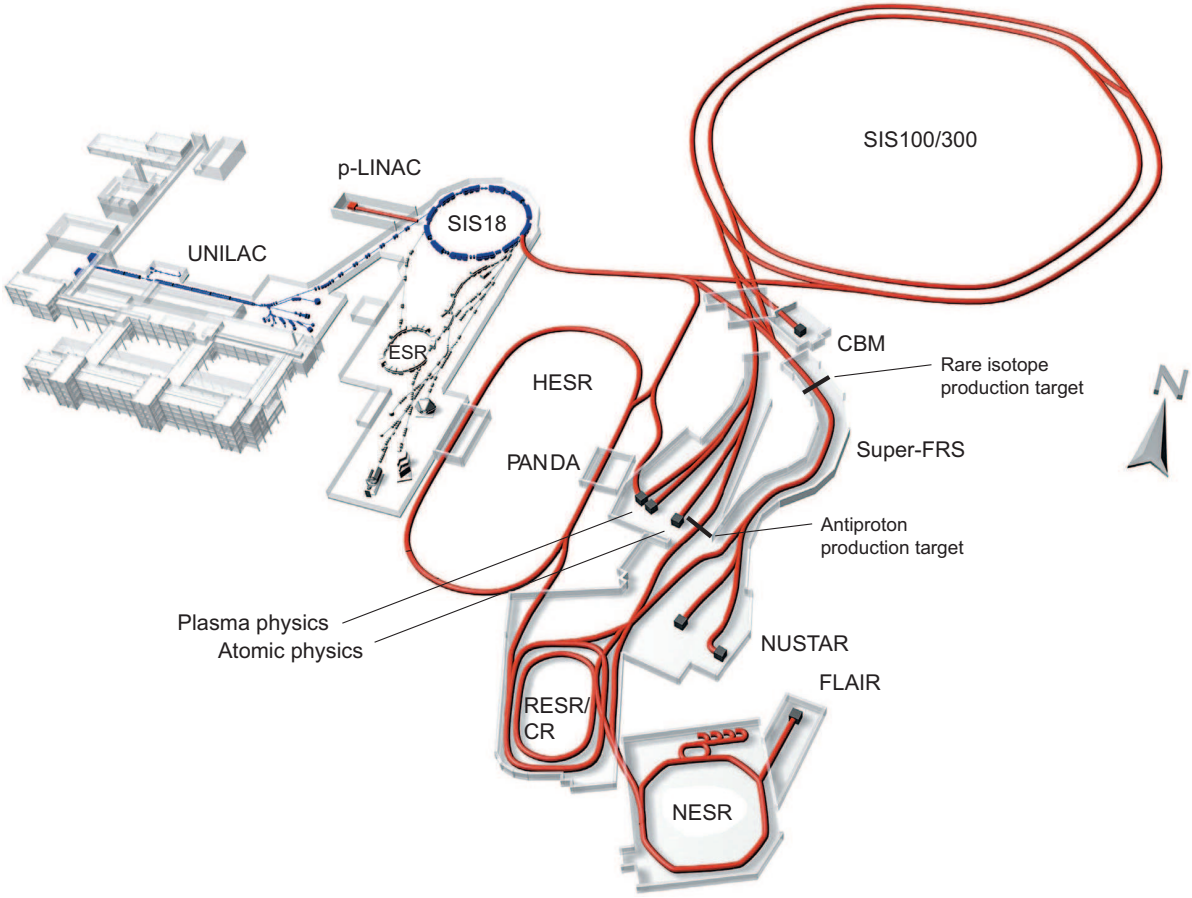

Fig. 1.1: Present layout of the the GSI facility (blue and black) on the left hand side (*UNILAC*, *SIS 18*, *ESR*) and the planned FAIR facility (red) on the right hand side: the superconducting synchrotrons *SIS 100* and *SIS 300*, the collector ring *CR*, the accumulator ring *RESR*, the new experimental storage ring *NESR*, the superconducting fragment separator *Super-FRS*, the proton linac, and the high energy antiproton ring *HESR*. The experimental stations for plasma physics, relativistic nuclear collisions (*CBM*), radioactive ion beams (*Super-FRS*), atomic physics, and low-energy antiproton and ion physics (*FLAIR*) are also shown [KB09].

UNILAC and SIS 18, the existing GSI accelerators, will serve as injectors for the new synchrotrons (SIS 100/300) after an upgrade for higher intensities. The first experimental station of the new future facility following the double-synchrotron is the **C**ompressed **B**aryonic **M**atter (CBM) experiment (see Fig. 1.1). Further down stream, a system of storage-cooler rings and other experiment stations, including a **Super**conducting nuclear **Fr**agment **S**eparator (Super-FRS) and an antiproton production target in the east, and a storage ring for antiprotons (**H**igh-**E**nergy **S**torage **R**ing (HESR)) is located next to

the existing GSI facility area in the west. Adjacent to the HESR and Super-FRS is the **C**ollector **R**ing (CR), and the **N**ew **E**xperimental **S**torage **R**ing (NESR) in the south. FAIR will provide beams of rare isotope ions from hydrogen to uranium and antiprotons with an unique intensity, quality and particle energies from 5 up to 35 AGeV for U^{92+}, which is twenty times higher than those available at GSI today.
Due to the intrinsic cycle times of the accelerator and storage-cooler rings, up to four research programs (CBM, $\overline{\text{P}}$ANDA, NUSTAR, and FLAIR (**F**acility for **L**ow-energy **A**ntiproton and heavy-**I**on **R**esearch)) can be run in parallel.
CBM is designed to investigate nucleus-nucleus collisions at highest baryon densities. The $\overline{\text{P}}$ANDA (**Antiproton An**nihilation at **Da**rmstadt) detector at the HESR will be used for hadron physics experiments using a cooled high-energy antiproton beam whereas the NUSTAR (**Nu**clear **St**ructure, **A**strophysics and **R**eactions) detectors (connected to the Super-FRS) will investigate the structure of unstable nuclei and will be used for experiments on nuclear astrophysics. There will be also experimental setups for plasma physics and atomic physics at FAIR.

1.1. CBM Experiment

The aim of the fixed target experiment CBM at FAIR is to investigate the phase diagram of highly compressed nuclear matter especially in the region of high baryon chemical potential , to screen for the deconfinement phase transition at high baryon densities and the **Q**uantum **C**hromo**d**ynamics (QCD) critical endpoint , to study the chiral symmetry restoration in superdense baryonic matter, and to study the nuclear equation of state at high baryon densities[1]. The existence of such super-dense nuclear matter is predicted inside of neutron stars. These extreme conditions are assumed to be reachable within the reaction volume of relativistic heavy-ion collisions. Different phases (shown in Fig. 1.2) of QCD like **Q**uark **G**luon **P**lasma (QGP) at high values of T and/or high values of μ_B, and the hadronic phase at low μ_B and low T values are supposed to be created by modulation of the beam energy and reaction system. The color-superconducting region at high μ_B and low T is supposed to exist within the core of neutron stars. At very high beam energies, as provided by the **R**elativistic **H**eavy-**I**on **C**ollider (RHIC) at Brookhaven and the **L**arge **H**adron **C**ollider (LHC) at CERN, matter is created at high temperatures similar to the early universe.

Chiral symmetry restoration might be researched by measuring dileptons originating from the decay of low mass (short-lived) vector mesons and photons. Since leptons interact only electroweakly, they are very little effected by the passage through the high density matter. For this purpose, they provide almost undistorted information on the conditions in the interior of the collision zone. It is expected that vector mesons will melt inside the fireball with the increase in baryon density at FAIR energies. Therefore, they will be an important observable to probe the dense medium. Another key observable for the CBM experiment is the measurement of hidden charm or charmonium. Particles containing charm quarks are produced in the early stage of the collision. At FAIR open and hidden charm production will be studied at beam energies close to the kinematic threshold. The production mechanisms of D and J/ψ mesons are expected to be sensitive to the conditions inside the early fireball. The observation of sequential melting of ψ'

[1] The interested reader may get more detailed information at the following places: [KB09], [FK04], [Kar99], [Sen06], [Sim01], [FK02], and [RCH04].

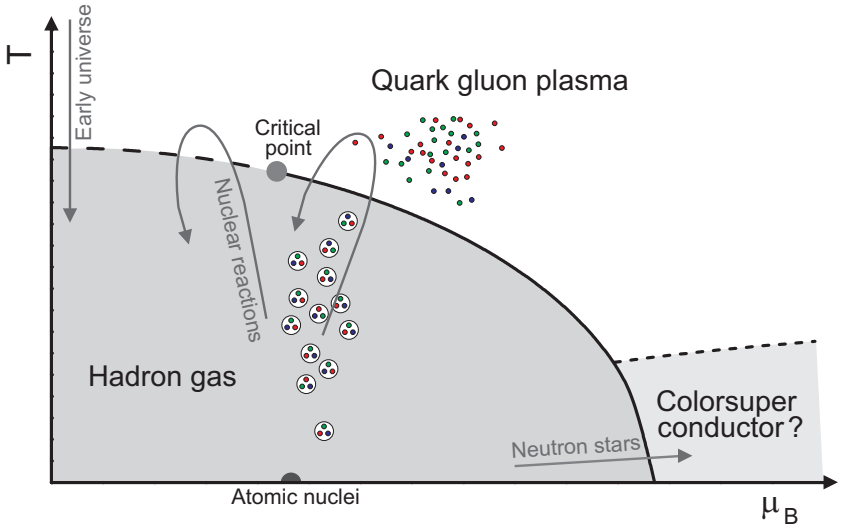

Fig. 1.2: Schematic phase diagram of QCD [KB05]. The dot on the μ_b-axis denotes the baryon density of normal nuclear matter. The three different expected regions of QCD: the hadronic phase (at low μ_B and low T), the QGP (at high T), and the color-superconducting region (at high μ_B, low T).

and J/ψ mesons at different temperatures, might serve as an indication for the onset of deconfinement. Since, no data on J/ψ production are available in nucleus-nucleus collisions at beam energies below 158 AGeV. Data on J/ψ and ψ' production at FAIR energies could help us to understand charmonium production and its relation to the matter created in heavy-ion collisions [K$^+$08]. In contrast to hadronic particles, photons only interact electromagnetically and have a long mean free path. Hence, photons do not interact after their production and leave the fireball undisturbed. The direct-photon yield is important for the diagnosis of QGP formation. Only the combination of FAIR with its high intensity beams and CBM designed specifically for heavy-ion collisions in the intermediate energy range will provide the capability of measuring all these probes. This leads to sufficient statistics for more detailed measurements of these probes as their collective effects may be visible for the first time at these energies. The experimental challenge of the CBM experiment is to identify hadrons and leptons in collisions with up to 1000 charged particles at event rates of up to 10 MHz. These measurements require fast and radiation hard detectors, online event-selection based on future CPU/GPU architectures, and a high-speed **D**ata **Acq**uisition (DAQ) system. The measurement of particles with open charm, which is based on the real time reconstruction of displaced vertices with an accuracy of 50 μm [CBM08], is particularly demanding.

1.2. CBM Detector Design

The current setup for the CBM experiment planned at FAIR consists of a high-resolution **S**ilicon **T**racking **S**ystem (STS) and a **M**icro-**V**ertex **D**etector (MVD), a **T**ime-**O**f-**F**light detector (TOF) made from timing **R**esistive **P**late **C**hambers (RPC), and an **E**lectromagnetic **Cal**orimeter (ECAL) based on lead/scintillator layers. The sketch on the left of Figure 1.3 shows the setup for electron measurement with a **R**ing **I**maging **Ch**erenkov (RICH) and three stations **T**ransition **R**adiation **D**etectors (TRD) with 3-4 layers each. In the right sketch of Figure 1.3 a muon detection system consisting of

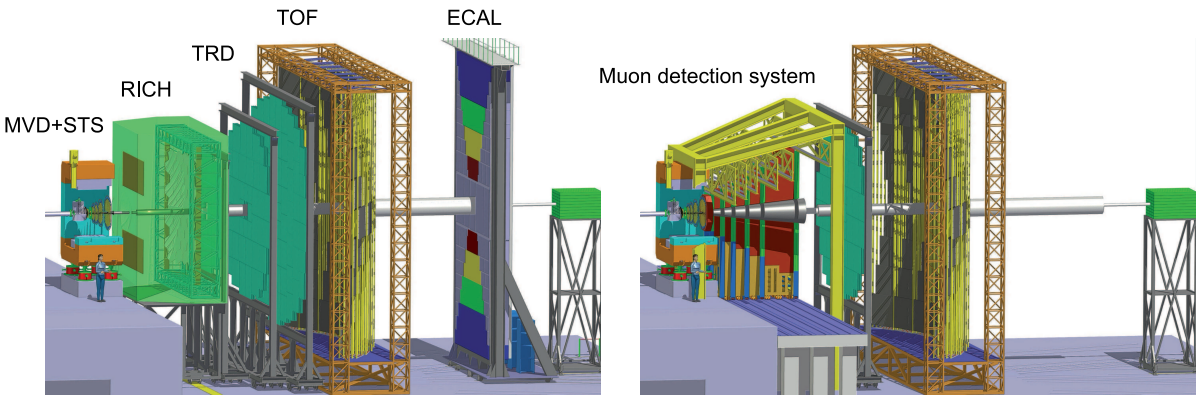

Fig. 1.3: Current setup for the CBM experiment planned at FAIR [Sen09].
The setup consists of consists of a high-resolution STS, a TOF made from RPCs, and an ECAL based on lead/scintillator layers. The sketch on the left shows the setup for electron measurement with a RHIC and three stations TRD with 3-4 layers each. In the right sketch a muon detection system consisting of hadron absorber layers and tracking detector layers is shown.

hadron absorber layers and tracking detector layers is shown. For the lepton measurement in CBM, two optional setup tasks are scheduled: the identification and reconstruction of electrons as well as the measurement of muons. A typical target used in the CBM experiment is a gold target of 250 μm thickness. The first detector component behind the target of CBM is a STS and a MVD located in a dipole magnet. STS consists of several layers of silicon microstrip detectors. It has to provide the track reconstruction and momentum determination. MVD is used to measure the position of the primary and secondary vertices with very high precision.
The next detector array behind STS and MVD is a RICH detector and a system of TRD which provide the electron identification. The TRD (5 m, 7.25 m, and 9.5 m behind the target) also is used as tracking detector for charged particles. The RICH is planned to be locomotive such that it can be replaced by a muon detection system. This muon detection system consists of hadron absorber layers (made of iron) sandwiched by large area tracking detector layers. The hadron identification is supported by a TOF measurement with a wall of timing RPCs. In addition, the TOF can be used to identify electrons at low momenta. An ECAL is used for the measurement of photons.

1.3. Transition Radiation Detector for CBM

The **T**ransition **R**adiation **D**etector (TRD) is used to identify electrons with a pion suppression factor of the order of 100 at an electron efficiency of 90% and for tracking of charged particles. **T**ransition **R**adiation (TR) is produced by electrons and positrons only in the expected particle momentum range ($\gamma > 1,000$), if a relativistic electron or positron traverses the radiator. This offers the possibility of separating electrons and positrons e.g. from pions. Up to now, the TRD is to be distributed into three stations, which are located at distances of 5 m, 7.25 m, and 9.5 m from the target. Each station consists of three to four layers which are composed of a radiator, in which the TR is produced by electrons, and a **M**ulti**w**ire **P**roportional **C**hambers (MWPC) detector operated with a Xe(85%) CO_2(15%) mixture, in which the energy loss of charged particles and the TR photons can be measured (see Chapter 2.3). A total active area of about

$600\,\mathrm{m}^2$ is covered by the TRD. One technical design goal of the TRD is to track all charged particles with a position resolution of 300-500 μm in x- and y-directions (perpendicular to the beam direction) within this area. For fixed-target experiments the central part of the detector is exposed to the highest counting rates. For the CBM-TRD this will be the inner part of the TRD with counting rates up to $100\,\mathrm{kHz/cm}^2$ due to high interaction rates of up to 1 GHz. In order to minimize possible space charge effects, the gas volume must be sufficiently thin but also wide enough to provide a sufficient e/π-separation, which is directly related to TR absorption within the gas volume.
Up to now, a detector built from straw tubes or a MWPC with pad readout have been under consideration for such a detector. Both TRD versions have been investigated as alternative designs. At present, the straw tubes are not considered as an option for the TRD anymore. This thesis deals with the MWPC based TRD.

2. Detector Principle

Charged particles and photons can only be detected through their energy loss due to their interaction with matter. This energy loss is fundamental to most particle and photon detectors. Depending on the required quantity, one can use different interaction processes of particle and detector.
Charged particles can be detected by their characteristic energy loss inside the detector when traveling through detector material. The energy loss is due to the electromagnetic interaction with atomic nuclei or electrons. This interaction leads to excitation or ionization of atoms in the detector material, or to the emission of bremsstrahlung, if the particle is scattered of nuclei. Hadrons can, in addition, lose energy through hadronic interactions like inelastic nuclear collisions, or nuclear excitations. Photons can interact, depending on the photon energy, with atomic electrons of the detector material via Compton scattering, or the photoelectric effect, or they convert into e^+e^- via pairproduction, if a minimum energy ($\geq 1.022\,\mathrm{MeV}$) is reached. Subsequently, the produced electrons and positrons can be detected, like other charged particles, through their energy loss.

2.1. Interaction of Charged Particles with Matter

The electromagnetic interaction of charged particles traversing a matter filled volume depends on the momentum of the particles. Moderately relativistic charged particles lose energy in matter primarily by ionization and atomic excitation. Electrons are an exception, they predominantly lose energy via bremsstrahlung. The mean specific energy loss for particles heavier than electrons is described by the Bethe-Bloch formula [A+08]:

$$-\frac{dE}{dx} = Kz^2\frac{Z}{A}\cdot\frac{1}{\beta^2}\left[\frac{1}{2}\ln\left(\frac{2m_ec^2\beta^2\gamma^2T_{max}}{I^2} - \beta^2 - \frac{\delta_{corr}(\beta\gamma)}{2}\right)\right]. \tag{2.1}$$

Symbol	Definition	Units or Value
α	Fine structure constant $e^2/4\pi\epsilon_0\hbar c$	1/137.035 999 11(46)
m_ec^2	Electron mass $\cdot c^2$	0.510 998 918(44) MeV
ze	Charge of incident particle	
Z	Atomic number of absorber	
A	Atomic mass of absorber	g/mol
K/A	$4\pi N_A r_e^2 m_e c^2/A$	0.307075 MeV cm^2/g for A=1 g/mol
p	particle momentum	MeV/c
I	Mean excitation energy	eV
β	Velocity in terms of the speed of light v/c	
γ	Lorentz factor $1/\sqrt{1-(v/c)^2}$	
$\delta_{corr}(\beta\gamma)$	Density effect correction to ionization energy loss	
$\hbar\omega_p$	Plasma energy $\sqrt{4\pi N_e r_e^3}m_ec^2/\alpha$	$28.816\,\rho\langle Z/A\rangle$eV
X_0	Radiation length	g/cm^2
E_c	Critical energy for electrons	MeV
$E_{\mu c}$	Critical energy for muons	GeV
m_P	Mass of the projectil	MeV/c^2

Symbol	Definition	Units or Value
m_T	Mass of the target	MeV/c^2
T_{max}	Maximum kinetic energy loss	MeV cm^2/g

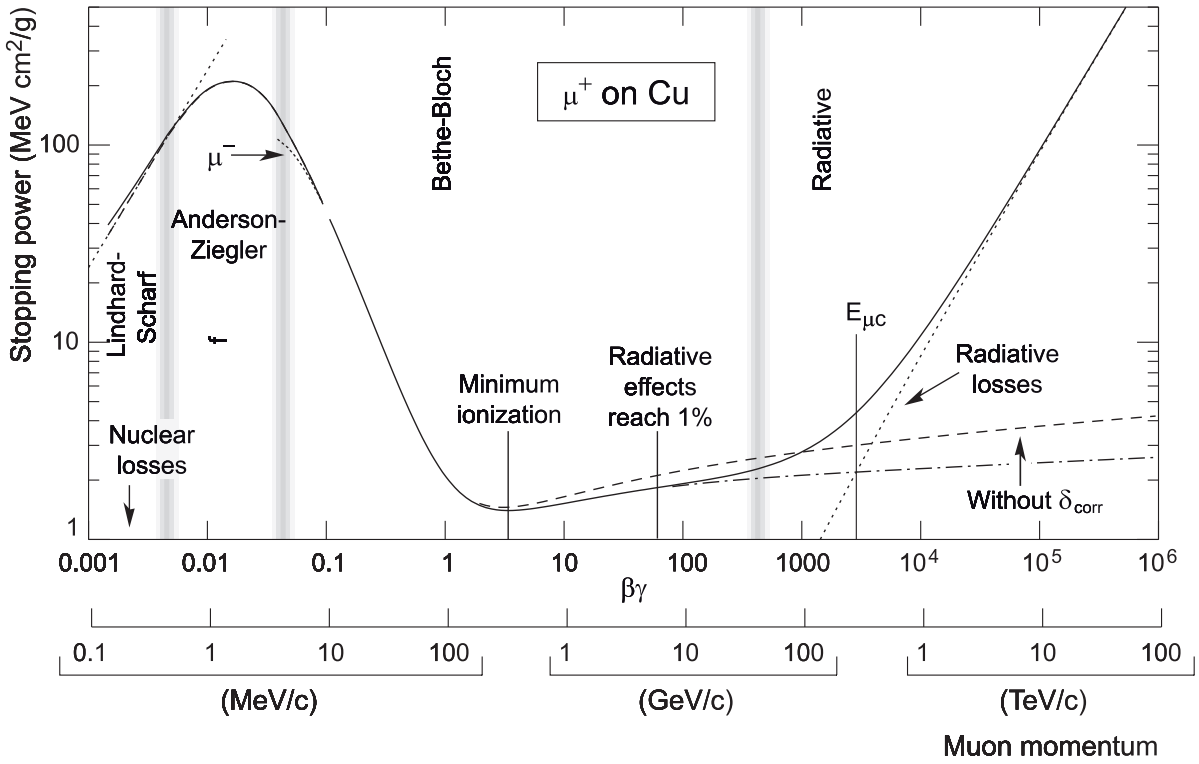

Fig. 2.1: Stopping power for positive muons in copper as function of $\beta\gamma = p/Mc$ over nine orders of magnitude in momentum (12 orders of magnitude in kinetic energy) [A$^+$08]. The curves with and without density-effect correction for the energy loss due to ionization and excitation are shown. The solid curve indicates the total energy loss which is the sum of the energy loss due to ionization and the energy loss due to bremsstrahlung.

The maximum kinetic energy loss T_{max}, that can be imparted to a free electron in one head-on collision, is given by [A$^+$08]:

$$T_{max} = \frac{2m_e p^2}{m^2 + 2\gamma m_e m + m_e^2}. \tag{2.2}$$

At non-relativistic energies, dE/dx is dominated by the over all $1/\beta^2$ factor and decreases with increasing particle momentum. The stopping power functions are characterized by a minimum at about $\beta\gamma = 3$ to 3.5 for materials with Z between 7 and 100. Particles at this region are known as minimum ionizing particles. The function as computed for muons on copper is shown by the solid curve in Fig. 2.1. In practical cases, most relativistic particles (e.g. cosmic-ray muons) have mean energy loss rates close to the minimum. As the energy increases beyond the minimum, the term $1/\beta^2$ becomes almost constant and the stopping power rises again due to the logarithmic dependence of the Bethe-Bloch formula. This relativistic rise canceled, however, by the density correction $\delta_{corr}(\beta\gamma)$ as shown in Figure 2.1. At higher energies, radiative effects begin to be important.
The Bethe-Bloch formula (Eq. 2.1) describes the average energy loss of charged particles

per path unit Δx. The exact energy loss fluctuates around this average value due to the fact that the energy loss is a statistical quantity. For thin materials the total energy loss is given by a small amount of interactions, each one with a very wide range of possible energy transfers. The resultant energy loss probability distribution (the distribution of $(-\frac{dE}{dx})\Delta x$) can be described by a Landau distribution. This distribution is skewed towards larger values (the Landau tail) for detectors of moderate thickness x. For thicker absorbers the distribution is less skewed. The distribution is roughly Gaussian for very thick absorbers, where the energy loss exceeds half of the original particle energy. However, an exact Gaussian shape is never reached. A long 'tail' at large energy losses is expected due to δ-ray emission (secondary knock-on electrons with kinetic energies $T \gg I$) or other processes. This large fluctuations of the mean can be reduced by taking a large number of samples. The most probable energy loss is $\langle \Delta E \rangle \sim \langle dE/dx \rangle L$ for a particle passing through a diluted material of the length L. The Landau distribution of deviations from the most probable energy loss $(\Delta E - \langle \Delta E \rangle)$, expressed in terms of fractional deviations of the mean loss about the most probable energy loss is [Gre00]:

$$\begin{aligned} P(\kappa) &= \frac{1}{\sqrt{2\pi}} \exp\left(\frac{1}{2}\left(\kappa + \exp(-\kappa)\right)\right), \\ \text{with } \kappa &\equiv \frac{(\Delta E - \langle E \rangle)}{\langle E \rangle}. \end{aligned} \tag{2.3}$$

The Bethe-Bloch equation (Eq. 2.1) has to be modified for electrons and positrons. The assumption that the incident particle remains undeflected during collision is invalid due to the small mass of the incident particle. Furthermore, the collision of bonded electrons and the incident electron is between indistinguishable, identical particles. Thus, the range of the kinetic energy extends only to half of the kinetic energy of the incident particle. At low energies electrons and positrons primarily lose energy by ionization, as well as Møller scattering, Bhabba scattering, and e^+ annihilation contribute, but decrease for higher energies. High-energy electrons predominantly lose energy by emitting

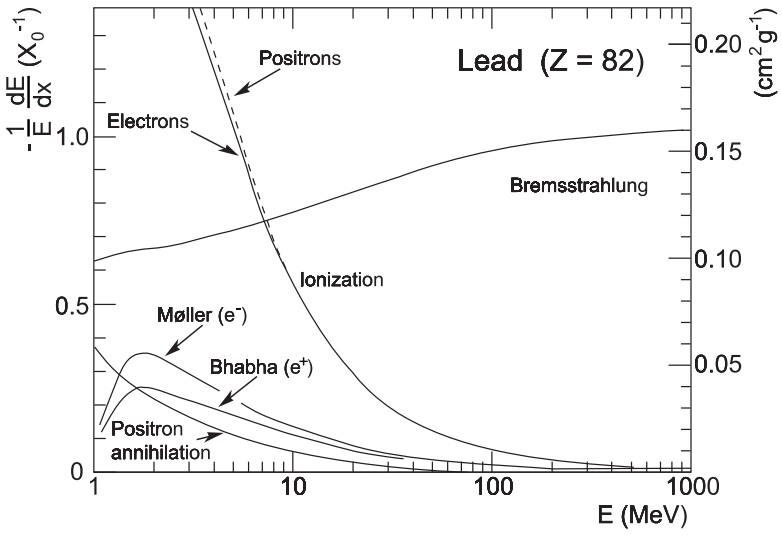

Fig. 2.2: Fractional energy loss per radiation length in lead as function of electron or positron energy for a radiation length of $X_0(Pb) = 6.37\,\mathrm{g/cm^2}$ [A$^+$08].

bremsstrahlung. Bremsstrahlung is emitted by an high-energy charged particle when it

is decelerated in the field of a nucleus. The process cross-section increases approximately linearly with the energy of the electron and quadratically with the atomic charge number Z of the medium. This effect dominates above the critical energy E_c; the energy where the losses due to ionization and bremsstrahlung for electrons are the same. E_c can be calculated for different projectile particles e.g. muons in solid, liquid, and gases by the following equations [Gru99],

$$\begin{aligned} E_{c,\text{solid, liquid}} &\approx \frac{610\,\text{MeV}}{Z+1.24} \cdot \left(\frac{m_P}{m_e}\right), \\ E_{c,\text{gas}} &\approx \frac{710\,\text{MeV}}{Z+0.92} \cdot \left(\frac{m_P}{m_e}\right). \end{aligned} \tag{2.4}$$

The mean distance over which a high-energy electron loses all but $1/e$ of its energy through bremsstrahlung is called radiation length X_0. The fractional energy loss in units of radiation length as function of the electron or positron energy for lead is shown in Figure 2.2. The radiation length in lead is $X_0(Pb) = 6.37\,\text{g/cm}^2$.

2.1.1. Cherenkov Radiation

Cherenkov radiation is electromagnetic radiation emitted when a charged particle passes through a medium at a constant speed greater than the speed of light in that medium. The electric field of a moving particle in a medium (refractive index n greater than 1), will interact with the medium. This electromagnetic interaction of the particle and the medium leads to the formation of a wave front (in analogy to a Mach cone) in the medium for a velocity $v > c/n$, where c is the speed of light (see Fig. 2.3). It is shown that the

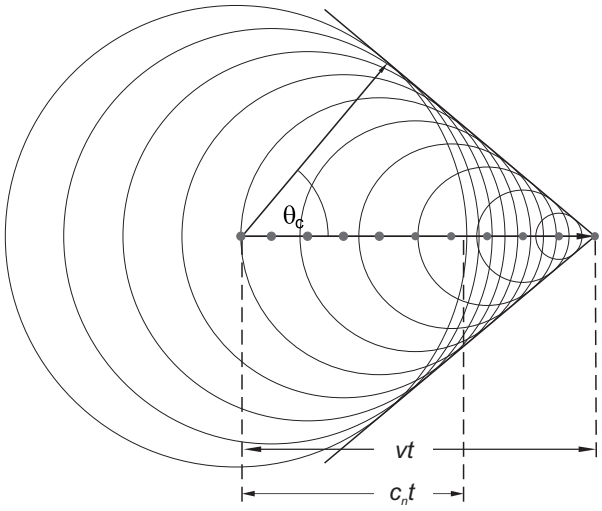

Fig. 2.3: Construction of the Cherenkov emission angle Θ_c via elementary waves emitted from each point of the partical trajectory adding up constructively along a line.

emitted wavelets from each point of the partical trajectory add up constructively along a line defined by the Cherenkov angle Θ_c with respect to the direction of the particle. The angle can be derived from the geometrical construction shown in Fig. 2.3:

$$\cos(\Theta_c) = \frac{c_n t}{vt} = \frac{1}{\beta n} \tag{2.5}$$

for $v > c_n$ and $\cos(\Theta_c) < 1$ if $\beta > 1/n$.
Due to the fact that the Cherenkov energy loss is negligible compared to the particle's energy, the Cherenkov radiation can be used for non-destructive detection and identification of particles. Cherenkov counters utilize one or more of the properties of Cherenkov radiation: the existence of a threshold for Cherenkov radiation [Gru99]

$$\begin{aligned} \beta_{thres} &= \frac{v_{thres}}{c} = \frac{1}{n} \\ \Rightarrow E_{thres} &= \frac{n}{\sqrt{n^2-1}} m_0 c^2, \end{aligned} \tag{2.6}$$

the dependence of Θ on the velocity $v = \beta c$ of the particle (see Eq. 2.5)

$$\Theta = \arccos\left(\frac{1}{n\beta}\right), \tag{2.7}$$

and/or the dependence of the number of emitted photons on the velocity of the particle with the charge z at a given wavelength λ is [A+08]

$$\frac{d^2N}{dxd\lambda} = \frac{2\pi\alpha z^2}{\lambda^2} \cdot \left(1 - \frac{1}{\beta^2 n^2(\lambda)}\right). \tag{2.8}$$

2.1.2. Transition Radiation

Transition **R**adiation (TR) was first noticed by Ginsburg and Frank in 1946. It can be emitted whenever a charged particle passes from one medium into another. Far from the boundary in the first medium the particle has a field characteristic of its motion and of the medium. Later, inside the second medium, its field configuration depends on its motion and the second medium. The field in the first and in the second medium differ due to the different electromagnetic properties of the media, even if the motion of the particle is uniform. Evidently the fields must reorganize themselves as the particle passes through the interface. During the reorganization of the fields some pieces of the fields are 'shaken off' as TR.

In a simple picture, transition radiation can also be regarded as being due to a changing dipole moment. This dipole moment is formed by the charged particle inside the first medium moving towards the second medium and its image charge inside the second medium moving in opposing direction. The image charge replaces the induced charge density at the interface, which is needed to match the boundary conditions. The dipole changes with time due to the motion of both particles. The pointing of the dipole vector changes direction and therefore is maximally accelerated, when the particles are crossing the interface - thus causing radiation. The following expressions for the relativistic case have been found [VEA00]:
The spectral dependence of TR intensity:

$$\frac{d^2W}{d\omega d\Theta} = \frac{2\alpha\hbar\Theta^3}{\pi} \cdot \left(\frac{1}{1/\gamma^2 + \Theta^2 + \omega_1^2/\omega^2} - \frac{1}{1/\gamma^2 + \Theta^2 + \omega_2^2/\omega^2}\right)^2. \tag{2.9}$$

The differential energy spectrum:

$$\frac{dW}{d\omega} = \frac{\alpha\hbar}{\pi}\left[\left(\frac{\omega_1^2 + \omega_2^2 + 2\omega^2/\gamma^2}{\omega_1^2 - \omega_2^2}\right) \cdot \ln\left(\frac{1/\gamma^2 + \omega_1^2/\omega^2}{1/\gamma^2 + \omega_2^2/\omega^2}\right) - 2\right]. \tag{2.10}$$

For the total radiation intensity emitted at a single interface:

$$W = \frac{\alpha\hbar}{\pi} \cdot \frac{(\omega_1 - \omega_2)^2}{\omega_1 + \omega_2}\gamma, \tag{2.11}$$

where $\omega_{1,2}$ are the plasma frequencies of the two media and Θ is the emission angle of the photon with respect to the particle trajectory. Some remarkable features of TR can be derived from these three equations for the relativistic case. The total energy lost by TR is proportional to γ of the particle. It shows that the linear dependence on γ of the TR spectrum can be used to separate charged particles with similar momentum but different mass, like electrons and pions. The typical emission angle of transition radiation photons is proportional to $1/\gamma$, strongly peaked in the forward direction and symmetric with respect to the crossing medium (see Fig. 2.4).

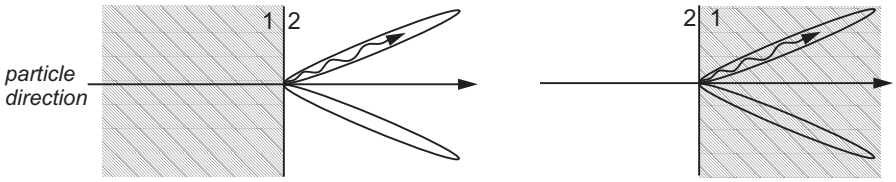

Fig. 2.4: Transition Radiation is strongly peaked into the forward direction and it is symmetric concerning the crossing medium [VEA00].

For a charged particle traversing a thin film with a width L, the wavelength of TR in the medium is λ' and the emission angle is Θ'. The optical path difference to an observation point O leads to a phase difference 2δ between waves produced from the entrance and exit point (A and B). An interference pattern can be seen due to the amplitudes A and $-A$ points A and B with an optical path length difference equivalent to the phase difference δ from the perspective of point O. The intensity I is given by [Gre00]

$$I = |A_A + A_B|^2 \approx 4\,|A|^2 \sin^2(\delta), \tag{2.12}$$

which is maximal for constructive interference, if $\delta \to \pi/2$, and minimal for destructive interference if, $\delta \to 0$. For a phase difference at the entrance and exit point of 180°, a sufficient optical path length difference [Gre00]

$$\delta \sim \frac{\omega L}{4c}\left(\left(\frac{\omega_p}{\omega}\right)^2 + \Theta^2 + \frac{1}{\gamma^2}\right) \tag{2.13}$$

is needed to avoid destructive interference. The double differential cross section for transition radiation is proportional to the finestructure constant α and is given by [Gre00]

$$\frac{d^2N_{TR}}{d\omega d\Omega} \sim \frac{\alpha}{\pi^2\omega}\Theta^2 \sin^2(\delta)\left[\left(\frac{1}{\delta}\right)^2 - \left(\frac{\omega L}{4c}\cdot\left(\Theta^2 + \frac{1}{\gamma^2}\right)\right)^{-2}\right]\cdot\left(\frac{\omega L}{2c}\right)^2. \tag{2.14}$$

The photon spectrum can be obtained by integrating Equation 2.14

$$\begin{aligned} \frac{dN_{TR}}{d\omega} &= \frac{2\alpha}{\pi\omega}\cdot\left[-1 + \left[\ln\left(1 + \frac{1}{y^2}\right)\right]\cdot\left(y^2 + \frac{1}{2}\right)\right], \\ \text{with} \qquad y &= \frac{\omega}{\gamma\omega_p}, \end{aligned} \tag{2.15}$$

where ω_p is the plasma frequency of the radiator material. The photon spectrum falls off rapidly for $y > 1$ or ω larger than $\gamma\omega_p$ being the characteristic frequency. A limiting case is $dN_{TR}/d\omega \to 2\alpha/\pi\omega[\ln(1/y)]$ for $y \ll 1$. One can assume from Equation 2.15 that $\alpha = 1/137$ TR photons per interface are emitted with energies of typically $\gamma(\hbar\omega_p)/3$. If a periodic sandwich of many foils is used, interference effects will produce a threshold effect in γ [Fab80]. In order to identify different electrons and pions a sufficient number of TR photon has to be generated by the electrons. Thus, a periodic arrangements of a large number of foils (so called radiator) are in use to generate these photons which are detected by X-ray detectors, e.g. MWPCs. Thin foils of lithium, polypropylene, polyethylene, or carbon are common radiator materials. Randomly spaced radiators are also in use, like foams, granules, or fiber mats.

2.2. Interaction of Photons with Matter

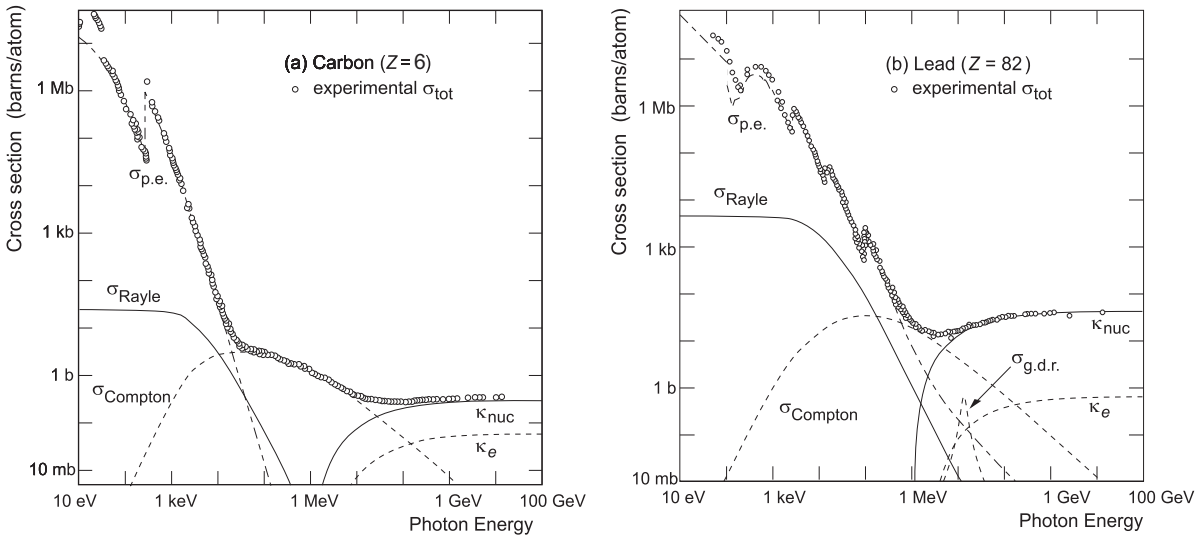

Fig. 2.5: Photon total cross section as a function of energy in carbon and lead [A+08]:
$\sigma_{p.e.}$ = atomic photoelectric effect (electron ejection, photon absorption),
$\sigma_{Rayleigh}$ = photoelectric effect (electron ejection, photon absorption),
$\sigma_{Compton}$ = incoherent scattering (Compton scattering off an electron),
κ_{nuc} = pair production, nuclear field,
κ_e = pair production, electron field,
$\sigma_{g.d.r.}$ = photo-nuclear interactions, most notably the Giant Dipole Resonance.

Similar to charged particles, the energy loss by electromagnetic interaction allows the detection of photons. The main difference between photon and charged particle interactions is that the photon is completely absorbed (photoelectric effect, pair production) or scattered at a large angle (Compton effect). The intensity I of a photon beam in matter is given by [Gru99]

$$I = I_0 \exp(-\mu x), \tag{2.16}$$

where I_0 represents the intensity without absorption and μ (mass attenuation coefficient) is related to the photon interaction cross section σ_i by [Gru99]:

$$\mu = \frac{N_A}{A} \sum_{i=1}^{3} \sigma_i. \tag{2.17}$$

Figure 2.5 shows the contributions of different interaction processes to the photon cross section in carbon and lead. The photoelectric effect dominates at low energies, but also Compton scattering, Rayleigh scattering (elastic scattering), and photo-nuclear absorption contribute. The conversion of the photon into an e^+e^- pair is possible in the electromagnetic field of a nucleus or an electron, if an energy of twice the electron mass is reached. Above a photon energy of 100 MeV pair production is the dominant process and saturates at some higher photon energy.

2.2.1. Photoelectric Effect

This effect results from the absorption of a photon by an atom and subsequent electron emission, which remains the initial atom as cation (shown in Fig. 2.6).

$$\gamma \quad + \quad atom \quad \rightarrow \quad \underbrace{atom^+}_{cation} \quad + \quad e^- \tag{2.18}$$

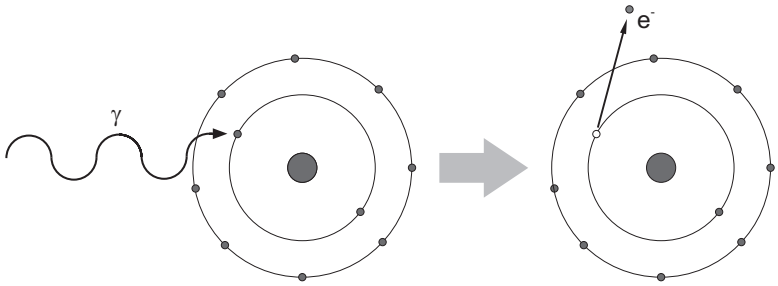

Fig. 2.6: Photoelectric Effect: Absorption of a photon by an atom and subsequent electron emission, which remains the initial atom as cation.

The photoelectric effect is of particular importance due to the fact that it is common practice for laboratory testing of proportional chambers to use X-ray emitting isotopes in the few keV region (equivalent to the typical energy loss of minimum ionizing particles in 1 cm gas), where the photoelectric effect is dominant (see Fig. 2.5).

Photoelectric absorption in an atomic shell i can take place only for photon energy $E_\gamma \geq E_i$. For higher photon energy, the contributions of all shells within $E_\gamma \geq E_i$ add up, which leads to a maximum in absorption, until a new main quantum number level is reached. For a new main quantum number level the absorption probability decreases rapidly with energy.

Absorption of a photon of the energy E_γ in a shell of the energy E_i results in the emission of a photoelectron of the kinetic energy $E_{kin,max}$ given by the maximum photon frequency ν_{max} and the work function W_A [Leo87]:

$$E_{kin,max} = h\nu_{max} - W_A, \tag{2.19}$$

where h is Planck's constant. The total energy and momentum can only be conserved for bound electrons. Therefore, the photoelectric effect always occurs on bound electrons with the nucleus absorbing the recoil momentum. The excited ion can then return to its ground state mainly through two competing mechanisms: fluorescence and Auger effect. For photon energies below MeV the cross section is characterized by absorption edges which correspond to thresholds for photo-ionization of various atomic levels. For

increasing photon energies this dependence goes as Z to the 4^{th} to 5^{th} power. Depending on Z of the material, the photoelectric effect is dominant up to energies of about 100 keV for low-Z materials like carbon with $Z = 6$, whereas it is dominant even up to energies of around 10 MeV for lead with $Z = 82$ (see also Fig. 2.5).

2.2.2. Compton Effect

The interaction of the photon with a quasi-free electron is called Compton scattering (see Fig. 2.7). A part of the photon momentum is transferred to the electron initially at rest:

$$\gamma \quad + \quad e^- \quad \rightarrow \quad \gamma \quad + \quad e^- \tag{2.20}$$

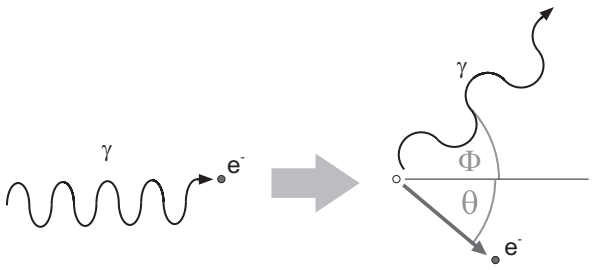

Fig. 2.7: Compton effect: scattering of the photon with a quasi-free electron,

Due to the energy loss the wavelength of the photon is increased after the scattering with a free electron [Sau77]:

$$\Delta\lambda = \frac{h}{m_e c}(1 - \cos\Phi), \tag{2.21}$$

where Φ is the scattering angle by which the photon direction has changed. The cross section for Compton scattering is proportional to the number of bound electrons and reaches its maximum for photon energies from about 100 eV to about 1 MeV (10 MeV) in carbon (lead) (see Fig. 2.5). The maximum recoil energy of the electron allowed by kinematics is given by [Leo87]:

$$T_{max} = h\nu\left(\frac{2\gamma}{1+2\gamma}\right) \quad \text{with} \quad \gamma = \frac{h\nu}{m_e c^2} \tag{2.22}$$

and is known as the Compton edge.

2.2.3. Pair Production

Pair production refers to the creation of an elementary particle and its antiparticle, usually from a photon (see Fig. 2.8). This is allowed, provided the photon energy is above the threshold of twice the particle mass (for electron and positron 1.022 MeV) and both energy and momentum are conserved:

$$\gamma \quad + \quad nucleus \quad \rightarrow \quad nucleus \quad + \quad e^- \quad + \quad e^+ \tag{2.23}$$

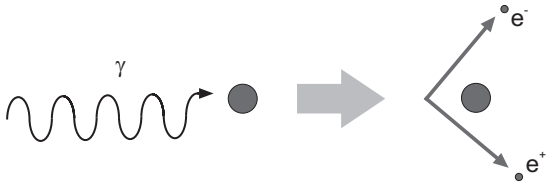

Fig. 2.8: Pair production: creation of an elementary particle and its antiparticle from a photon.

Therefore, a part of the momentum has to be transferred away from the e^+e^- pair. This can happen by exchanging a photon with a charged particle, which is most likely a nucleus (see Fig. 2.9). The cross section for pair production is proportional to Z^2. The cross section becomes independent of the photon energy for increasing energies, and screening of the electric field of the nucleus by the atomic electrons has to be taken into account.

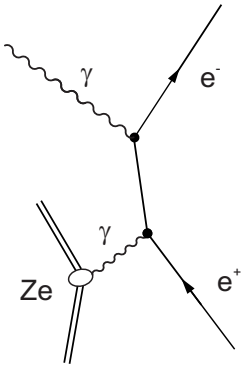

Fig. 2.9: Feynman diagram of pair production in the electromagnetic field of a nucleus with the charge $Z \cdot e$.

2.3. Multiwire Proportional Chambers

A **M**ulti**w**ire **P**roportional **C**hamber (MWPC) consists essentially of a set of thin, parallel, and equally spaced anode wires, symmetrically sandwiched between two cathode planes. Depending on the experimental requirements one usually choses a detector gas mixture consisting of a quenching gas like CO_2 and a noble gas like Xe or Ar. When a negative potential is applied to the cathodes and the anode is beeing grounded or a positive potential is applied to the wires and the cathodes are grounded, respectively, an electric field develops (See Fig. 2.10) which is approximatly given by [Kal06]:

$$E(y,z) = \frac{CV_a}{2\epsilon_0 s} \cdot \frac{\sqrt{1 + \tan^2\left(\frac{\pi y}{s}\right) \cdot \tanh^2\left(\frac{\pi z}{s}\right)}}{\sqrt{\tan^2\left(\frac{\pi y}{s}\right) + \tanh^2\left(\frac{\pi z}{s}\right)}}, \tag{2.24}$$

where C is the capacity per length unit, V_a is the applied anode voltage, the anode wire pitch s and the anode wire radius r_a:

$$C = \frac{2\pi\epsilon_0}{\frac{\pi h}{s} - \ln\left(\frac{2\pi r_a}{s}\right)}. \tag{2.25}$$

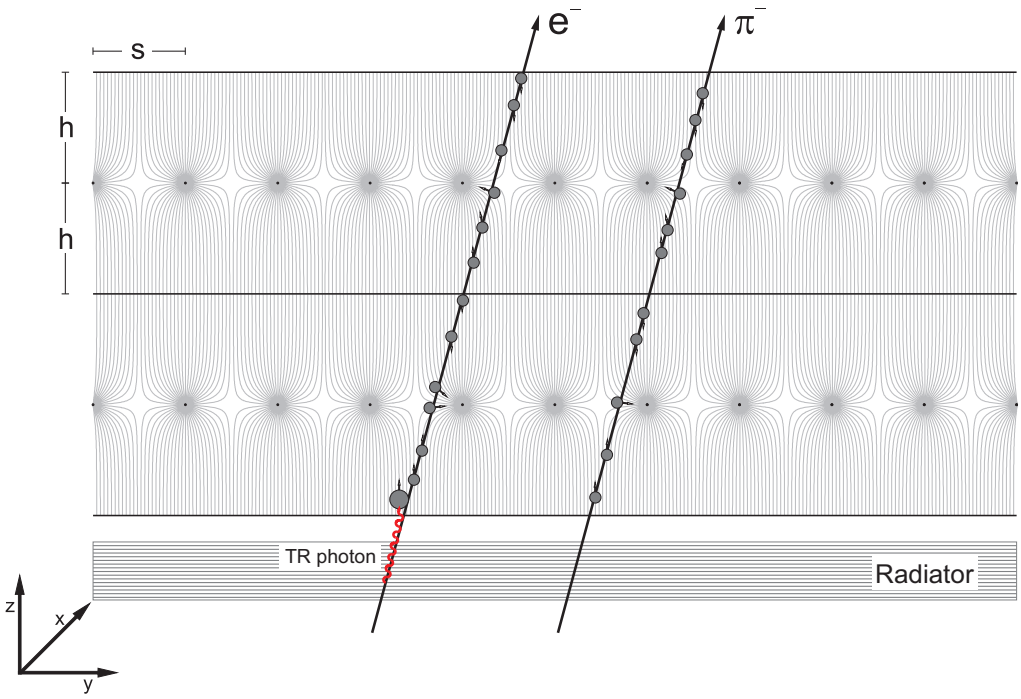

Fig. 2.10: Electric field develops inside the real-size prototype traversed by an electron and a pion. The TR photon created by the electron inside the radiator is absorbed by the detector gas mixture which leads to an increasing signal for electrons.

Granted that charges are liberated in the gas volume by a traversing relativistic particle. The ionization energy loss of the charged particles is typically a few keV per centimeter of gas under normal conditions. The electric potential between cathode and anode is set such that electrons will drift along field lines until they reach the high field region, very close to the anode wires, where avalanche multiplication can occur depending on the applied anode voltage.
The gaseous ionization detectors can be separated into three types working at different voltages: the *ionization chamber*, the *proportional counter*, and the *Geiger-Müller counter* (see Fig. 2.11).
If cathode and anode are both set to ground potential (I), the electron-ion pairs recombine under their own electrical attraction and no charge is collected at the anode or cathode. As the anode voltage is raised, the recombination is reduced and the current begins to increase. In the operating region of the *ionization chamber* (II), all created pairs are separated and collected and a further increase of the voltage has no effect on the output current. When further increasing the voltage above a certain threshold, the current increases again. This is due to the increasing kinetic energy of the electrons which can create now secondary electron-ion pairs by themselves during the avalanche multiplication. The number of electron-ion pairs in the avalanche is proportional to the number of primary electrons in the proportional counter potential region. This gives a proportional amplification of the current. The multiplication factor depends on the working voltage, the gas mixture, and the chamber geometry. This so-called *proportional counter* (III) region is the operating condition for MWPCs. As the anode voltage is raised to a very high voltage beyond the proportional region the energy of the electrons becomes so large that a discharge occurs in the gas. Instead of a single, localized

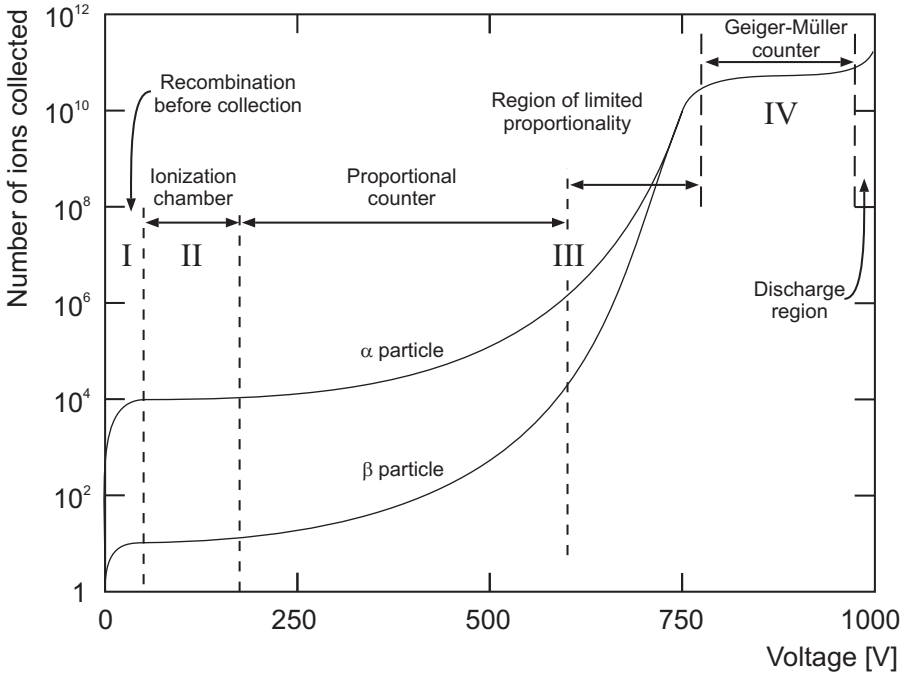

Fig. 2.11: Gain-voltage characteristics for a proportional counter, showing the differnt regions of operation [Sau77].

avalanche, a chain reaction of many avalanches is triggered. The output current becomes completely saturated, always giving the same amplitude which depends no longer on the energy of the initial event. *Geiger-Müller counters* (IV) are working in this voltage region.

2.3.1. Proportional Counter

For a MWPC configuration as shown in Figure 2.14 and an applied voltage in the so-called proportional counter region (see Fig. 2.11), the field lines are essentially parallel and the field density is almost constant in the region far away from the anode wires. The electric field in the chamber reaches its maximum at the surface of the anode wire and rapidly decreases, as r^{-1}, towards the cathode plane until a region of constant field strength is reached (drift region), as shown in Figure 2.10
The operation of the counter will then be as follows. In the constant field region where most of the electron-ion pairs are produced by the primary interaction of the incident particle with the gas volume, electrons and ions are liberated and drift along the field lines towards the nearest anode wire (electrons) or towards the cathode plane (ions). Very close to the anode wire the field increases, the electrons are quickly accelerated, and avalanche multiplication starts. A typical drop-like avalanche develops with all electrons in the front and ions behind (see Fig. 2.12). The avalanche surrounds the wire because of lateral diffusion and the small radius of the anode wire. The negative signal is given by the electron avalanche which is collected by the wires within a few nanoseconds. The positive ions are left over in the trail of the electrons avalanche due to their lower drift speed. They cause the so-called space-charge effects. During their drift towards the cathode plane (see Fig. 2.13) they reduce the electric field and thus

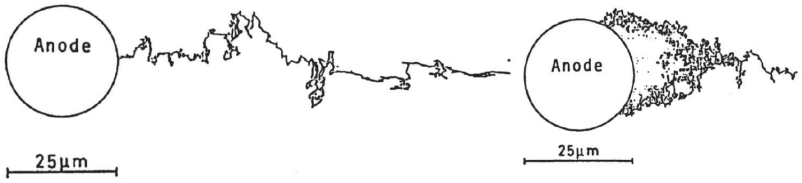

Fig. 2.12: **Left**: For low chamber potential: One electron drifting towards the anode wire
Right: For high chamber potential: A typical drop-like avalanche develops in the multiplication region close to the anode wire [MM85].

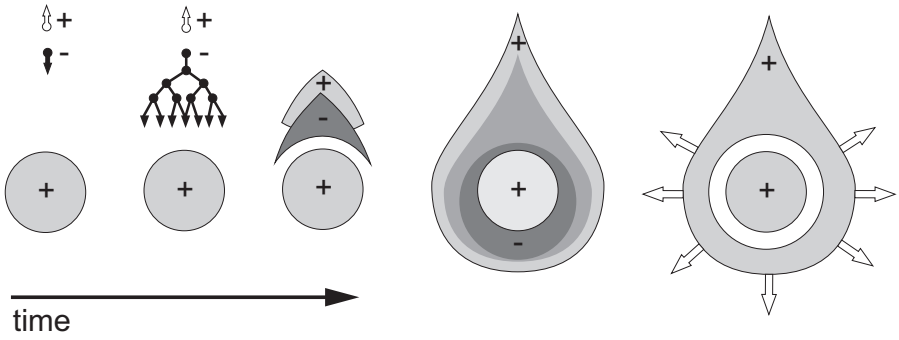

Fig. 2.13: Time development of an avalanche in a proportional counter. A single primary electron proceeds towards the anode wire, in regions of increasingly high fields, experiencing ionizing collisions; due to the lateral diffusion, a drop-like avalanche, surrounding the wire, develops. Electrons are collected in a very short time (about 1 nsec) and a cloud of positive ions is left, slowly migrating towards the cathode [Sau77].

the gas gain, particularly at high counting rates. The ions induce image charges in all surrounding electrodes and these result in a positive signal on the wire depending on the avalanche's position (as shown in Fig. 2.14) behind the electron peak.

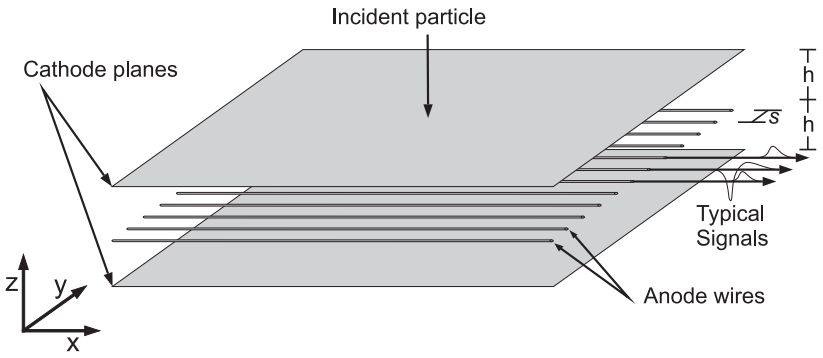

Fig. 2.14: Sketch of a MWPC with anode signal read-out based on [Leo87].

The neighboring wires are also effected, however, the signals induced here are of reverse polarity and have a smaller amplitude. In a similar manner, a positive signal is induced on the cathode plane, if the cathode is grounded and positive voltage is applied to the anode wires. The signal from one cathode plane does not give information on

the position of the avalanche. One can obtain the coordinate of the induced charge by a subdivision of the cathode into readout pads perpendicular to the anode wires as indicated in Figure 2.15. The avalanche can be localized in the direction parallel to the

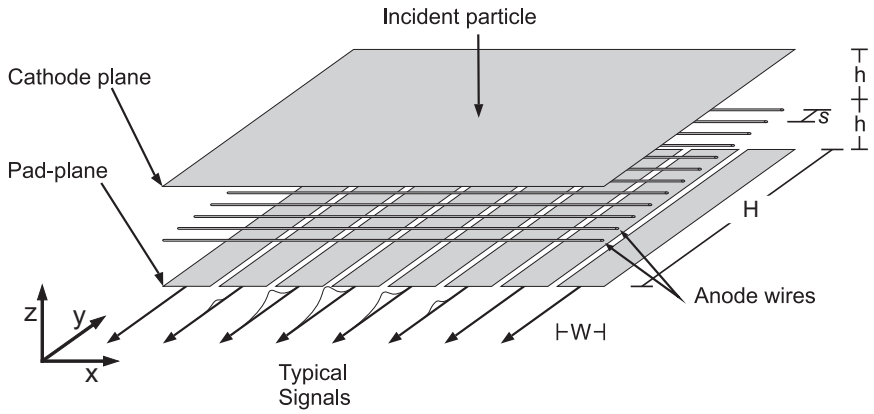

Fig. 2.15: Sketch of a MWPC with cathode signal read-out based on [EG+79].

sense wire as seen in the typical induced signals also drawn in Figure 2.15. The induced charge distribution should be shared between two or three adjacent pads in order to obtain the best possible position resolution in the cartesian coordinate system of the cathode pad plane. The signal to noise ratio decreases if the charge signal is shared by more than three pads. When the induced charge is measured only by one pad (one-pad clusters), the position resolution is given by $1/\sqrt{12}$ times the pad width W. Therefore, a proper matching of the pad width W to the width of the induced charge distribution is required. Additionally to the cluster position reconstruction performance, MWPCs feature electron-pion separation by the additional TR photon signal generated by the electrons with identical momenta due to their lower mass compared to the pion mass (see Chapter 2.1.2).

2.4. Track Position Reconstruction

In applications of multiwire proportional chambers, the knowledge of the distribution of induced charge is necessary to achieve the best position reconstruction performance. To find the best MWPC design one has to know the charge distribution as function of the geometrical chamber parameters.

2.4.1. Mathieson-Formula

The induced charge distribution on the cathode plane can be described by the empirical formula proposed by Mathieson [Mat88] which depends on chamber geometry parameters. To describe this distribution, one needs only one parameter K_3. $\rho(d/h)$ represents the induced charge density distribution on the cathode pad plane in a symmetrical chamber. The x-coordinate can either be parallel or normal to the anode wire direction. The anode-cathode separation is given by h and the net anode charge is q_a. Due to this the formula can be written in the following way [Mat88]:

$$\rho(d/h) = q_a \cdot \frac{\frac{\pi}{2} \cdot \left(1 - \frac{\sqrt{K_3}}{2}\right)\sqrt{K_3}}{4 \arctan\left(\sqrt{K_3}\right)} \cdot \frac{1 - \tanh^2\left(\frac{\pi}{2} \cdot \left(1 - \frac{\sqrt{K_3}}{2}\right)\frac{d}{h}\right)}{1 + K_3 \tanh^2\left(\frac{\pi}{2} \cdot \left(1 - \frac{\sqrt{K_3}}{2}\right)\frac{d}{h}\right)}. \tag{2.26}$$

Values of K_3 have been presented [Mat88] as function of characteristic chamber parameters like the anode wire radius r_a, anode-cathode separation h, and the anode wire pitch s (see Fig. 2.16). From this equation, one can calculate the charge ratio distri-

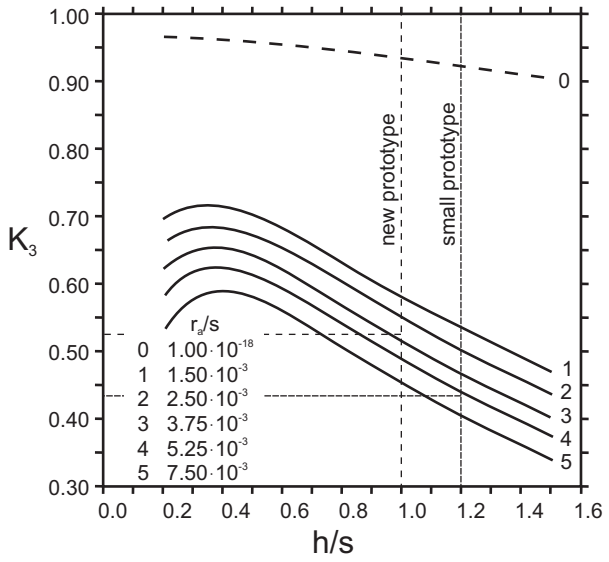

Fig. 2.16: Values of K_3 as function of h/s depending on r_a/s parallel to the anode wire direction [Mat88].

bution or so called **P**ad **R**esponse **F**unction ($PRF(d/h)$) by calculating the integral of $\rho(d/h)$ with $q_a = 1$.

$$\begin{aligned} PRF(d/h) &= \int_{d/h-W/2}^{d/h+W/2} \rho(d'/h)\; d(d'/h) \\ &= -\frac{\arctan\left(\sqrt{K_3}\tanh\left(\pi(\sqrt{K_3}-2)\cdot\frac{W-2\cdot d}{8h}\right)\right)}{2\arctan(\sqrt{K_3})} \\ &\quad -\frac{\arctan\left(\sqrt{K_3}\tanh\left(\pi(\sqrt{K_3}-2)\cdot\frac{W+2\cdot d}{8h}\right)\right)}{2\arctan(\sqrt{K_3})}. \end{aligned} \tag{2.27}$$

For the real-size prototypes an anode-cathode separation and an anode wire pitch of 3 mm therefore $h/s = 1$ was used. The anode wire radius is 12.5 μm and $r_a/s = 4.167 \cdot 10^{-3}$ which leads to $K_3 = 0.525$. For the small prototype $h = 3$ mm, $s = 2.5$ mm, and $r_a = 12.5\,\mu$m, $r_a/s = 5.0 \cdot 10^{-3}$ was used, which leads to $K_3 = 0,434$. The results for this K_3 value are shown in Figure 2.17. The shape of the Mathieson formula is more

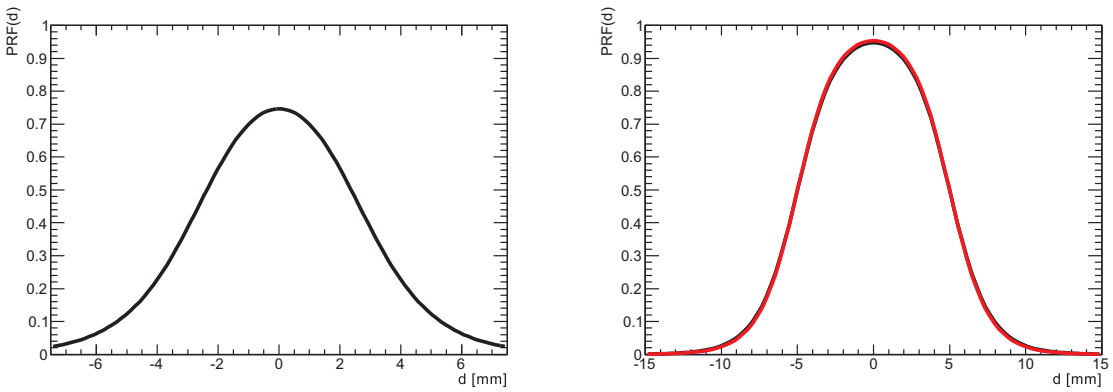

Fig. 2.17: Mathieson formula for: **Left**: Small prototype with $K_3 = 0,434$ for $h = 3\,\text{mm}$, $s = 2.5\,\text{mm}$, $r_a = 12.5\,\mu\text{m}$, and $W = 5\,\text{mm}$; **Right**: Black: real-size prototype with $K_3 = 0.525$ for $h = 3\,\text{mm}$, $s = 3\,\text{mm}$, $r_a = 12.5\,\mu\text{m}$, and $W = 10\,\text{mm}$; Red: $K_3 = 0,434$ for $h/s = 1.2$, $r_a/s = 4.167 \cdot 10^{-3}$, and $W = 10\,\text{mm}$ of the real-size prototype simulation (see Chapter 4.3).

effected by the pad width W than by K_3. This will be important in Chapter 4.3. The Mathieson formula can also be used to determine the cluster position. Therefore, the measured normalized charge ratio of each pad surrounding the pad with maximum charge (Q_{i-1}, Q_i, Q_{i+1}) divided by the total charge on all three adjacent pads ($Q_{i-1}+Q_i+Q_{i+1}$) is fitted to a parameterized Mathieson-fit function. The Mathieson formula given by Equation 2.27 is symmetric with respect to $d = 0$. Therefore, an another parameter x has to be defined to shift the maximum in d-direction. The Mathieson formula is defined as the characteristic average charge sharing signal of a chamber. Therefore, two additional parameters (A and K_3) are optional needed to add two degrees of freedom (width and height) in order to adapt the shape of the fit function to the form of single events as the fit function is to be used for fitting single events.

$$PRF(A, K_3, x) = A \cdot \left[-\frac{\arctan\left(\sqrt{K_3}\tanh\left(\pi(\sqrt{K_3}-2)\cdot\frac{W-2(d-x)}{8h}\right)\right)}{2\arctan(\sqrt{K_3})} - \frac{\arctan\left(\sqrt{K_3}\tanh\left(\pi(\sqrt{K_3}-2)\cdot\frac{W+2(d-x)}{8h}\right)\right)}{2\arctan(\sqrt{K_3})} \right], \tag{2.28}$$

$$PRF(A, x) = A \cdot \left[-\frac{\arctan\left(\sqrt{K_3}\tanh\left(\pi(\sqrt{K_3}-2)\cdot\frac{W-2(d-x)}{8h}\right)\right)}{2\arctan(\sqrt{K_3})} - \frac{\arctan\left(\sqrt{K_3}\tanh\left(\pi(\sqrt{K_3}-2)\cdot\frac{W+2(d-x)}{8h}\right)\right)}{2\arctan(\sqrt{K_3})} \right], \tag{2.29}$$

$$PRF(K_3, x) = -\frac{\arctan\left(\sqrt{K_3}\tanh\left(\pi(\sqrt{K_3}-2)\cdot\frac{W-2(d-x)}{8h}\right)\right)}{2\arctan(\sqrt{K_3})} - \frac{\arctan\left(\sqrt{K_3}\tanh\left(\pi(\sqrt{K_3}-2)\cdot\frac{W+2(d-x)}{8h}\right)\right)}{2\arctan(\sqrt{K_3})}, \tag{2.30}$$

$$PRF(x) = -\frac{\arctan\left(\sqrt{K_3}\tanh\left(\pi(\sqrt{K_3}-2)\cdot\frac{W-2(d-x)}{8h}\right)\right)}{2\arctan(\sqrt{K_3})} - \frac{\arctan\left(\sqrt{K_3}\tanh\left(\pi(\sqrt{K_3}-2)\cdot\frac{W+2(d-x)}{8h}\right)\right)}{2\arctan(\sqrt{K_3})}. \tag{2.31}$$

2.4.2. Pad Response Function

To determine the track position (x, y), Pad Response Function (PRF) measured by the charge sharing between adjacent pads can be used. The PRF is defined as the charge ratio of each pad surrounding the pad with maximum charge (Q_{i-1}, Q_i, Q_{i+1}) divided by the total charge on all three adjacent pads ($Q_{i-1}+Q_i+Q_{i+1}$) as function of the track position d relative to the center of the pad with maximum charge. A Gaussian shape of the PRF is assumed. For a track at a position d, a charge fraction on the pad with maximum charge (i), left pad ($i-1$), and right pad ($i+1$) will be measured. The charge fraction can be expressed in terms of function values of the PRF, where W denotes the pad width:

$$\frac{Q_i}{Q_{i-1}+Q_i+Q_{i+1}} = A\cdot\exp\left(-\frac{d^2}{2\sigma^2}\right), \tag{2.32}$$

$$\frac{Q_{i-1}}{Q_{i-1}+Q_i+Q_{i+1}} = A\cdot\exp\left(-\frac{(d+W)^2}{2\sigma^2}\right), \tag{2.33}$$

$$\frac{Q_{i+1}}{Q_{i-1}+Q_i+Q_{i+1}} = A\cdot\exp\left(-\frac{(d-W)^2}{2\sigma^2}\right). \tag{2.34}$$

To derive an equation to get d, Equation 2.32 is divided by Equation 2.33

$$\frac{Q_i}{Q_{i-1}} = \exp\left(\frac{2dW+W^2}{2\sigma^2}\right) \tag{2.35}$$

Now Equation 2.34 is divided by Equation 2.32

$$\frac{Q_{i+1}}{Q_i} = \exp\left(\frac{2dW-W^2}{2\sigma^2}\right), \tag{2.36}$$

Equation 2.36 by Equation 2.35

$$\frac{Q_{i+1}}{Q_{i-1}} = \exp\left(\frac{2dW^2}{2\sigma^2}\right), \tag{2.37}$$

and Equation 2.35 divided by Equation 2.36

$$\frac{Q_i^2}{Q_{i-1} \cdot Q_{i+1}} = \exp\left(\frac{W^2}{\sigma^2}\right). \tag{2.38}$$

Solved for d, the result is

$$d = \frac{W}{2} \cdot \frac{\ln\left(\frac{Q_{i+1}}{Q_{i-1}}\right)}{\ln\left(\frac{Q_i^2}{Q_{i-1} \cdot Q_{i+1}}\right)}. \tag{2.39}$$

The measured PRFs for the small and the real-size prototype are shown in Figure 2.19 and 2.18 using Equation 2.39.

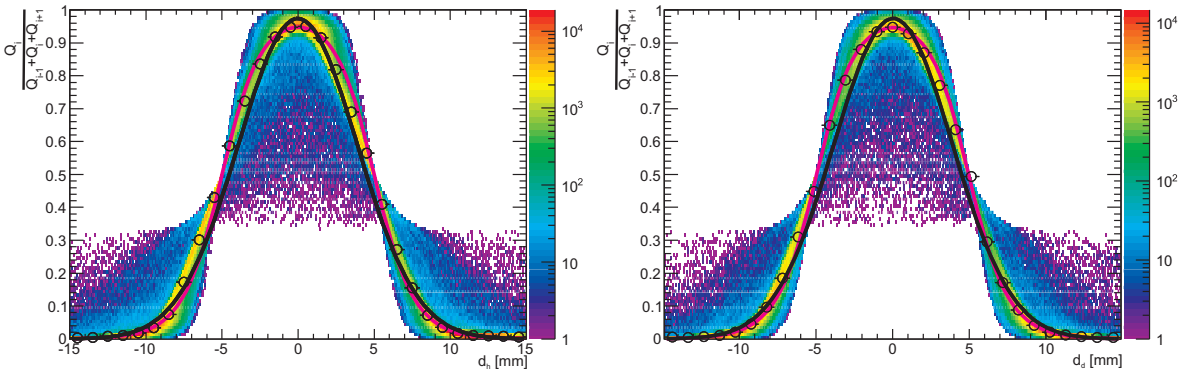

Fig. 2.18: PRF of the new prototype measured with ^{238}Pu: **Left**: Vertical pad group; **Right**: Diagonal pad group; ○: One-dimensional projection of the PRF; Black: Gaussian fit to the one-dimensional projection; Pink: Mathieson formula.

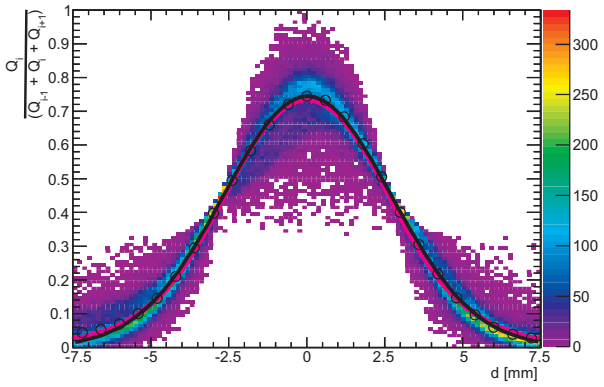

Fig. 2.19: PRF of the small prototype measured with Test beam data; ○: One-dimensional projection of the PRF; Black: Gaussian fit to the one-dimensional projection; Pink: Mathieson formula.

Once the PRF is measured, the track position relative to the center of the pad with maximum charge can be calculated by using Equation 2.35 solved for d. Therefore, the knowledge of the charge on pad i and $i-1$ is needed

$$d = \frac{\sigma^2}{W} \cdot \ln\left(\frac{Q_i}{Q_{i-1}}\right) - \frac{W}{2} \tag{2.40}$$

or the charge on pad i and $i+1$

$$d = \frac{\sigma^2}{W} \cdot \ln\left(\frac{Q_{i+1}}{Q_i}\right) + \frac{W}{2}. \tag{2.41}$$

The best results are obtained by combining these two equations to a weighted average of both displacements d, if the assumption of the Gaussian shape of the PRF is realistic. Since the errors of charge measurement are approximately inverse to the measured charge which is induced on the pad, the error of the calculated displacement can be minimized by choosing the weights as Q_{i-1}^2 and Q_{i+1}^2 [BR94]:

$$d = \frac{1}{Q_{i-1}^2 + Q_{i+1}^2}\left[Q_{i-1}^2\left(\frac{\sigma^2}{W}\ln\left(\frac{Q_i}{Q_{i-1}}\right) - \frac{W}{2}\right) + Q_{i+1}^2\left(\frac{\sigma^2}{W}\ln\left(\frac{Q_{i+1}}{Q_i}\right) + \frac{W}{2}\right)\right] \tag{2.42}$$

3. Small Prototype

As mentioned in Chapter 1.3, **M**ulti**w**ire **P**roportional **C**hamber (MWPC) based **T**ransition **R**adiation **D**etectors (TRDs) meet the experimental demands of the CBM TRD, like high-granularity, if exposed to high counting rates. This can be ensured by reducing the gas thickness in order to reduce space-charge effects in a high counting-rate environment. However, reducing the detector gas thickness leads to a smaller absorption probability for the TR photons and to a decrease of the pion suppression factor. In order to circumvent this aspect, while keeping the number of readout channels and material budget, small TRD prototypes with a double MWPC structure were designed in collaboration with the group of Prof. M. Petrovici in Bucharest, Rumania.

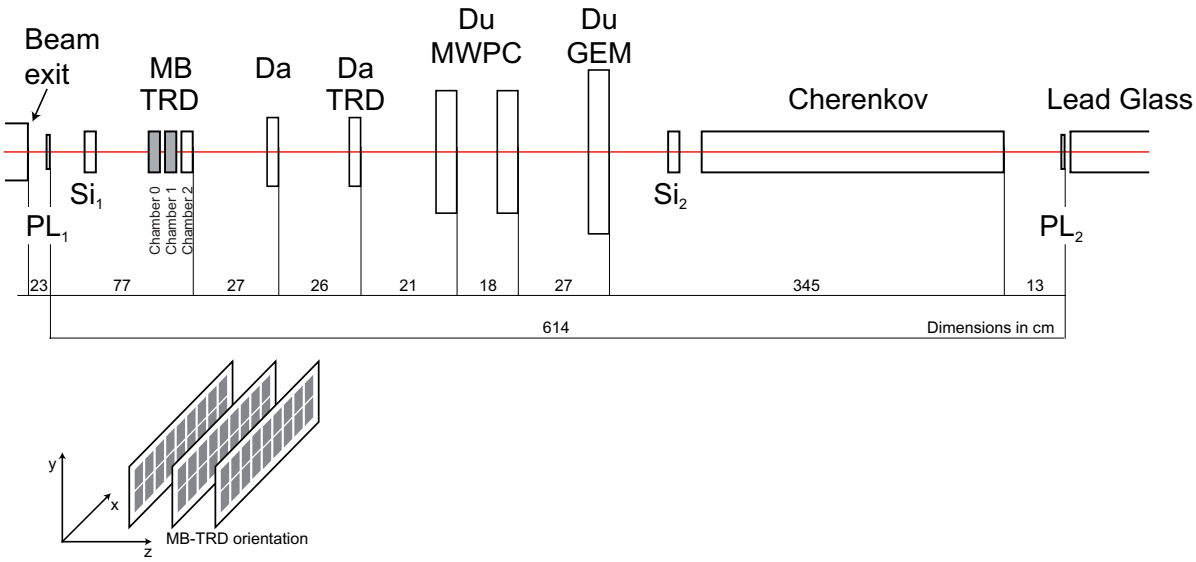

Fig. 3.1: Experimental configuration used for the in-beam tests in 2006 at GSI [KB09].

The small prototypes (MB TRD) were tested in a joint in-beam measurement campaign of the JRA4-I3HP collaboration in February 2006 at GSI Darmstadt. Mixed electron-pion (negative particles) and positron-pion-proton (positive particles) beams were used, which were provided by the SIS 18 accelerator. The experimental setup is shown in Figure 3.1. The tests were performed at different anode voltages and beam intensities, different Xe CO_2 gas mixtures and momenta of up to 2 GeV/c. The online run summary can be found in the appendix (see Table C.1). The beam intensity was varied by changing the extraction time (spill length). The spill length was determined by two arrays, each one consisting of four plastic scintillators (PL_1 and PL_2). The beam profile was monitored by two silicon strip detectors (Si_1 and Si_2). The scintillator counters, to which the Pb-glass detector signal was added was used as electron trigger. Electrons were identified with respect to hadrons using a Pb-glass calorimeter and an air-filled Cherenkov detector [KB09].

3.1. Layout

The design of the first TRD prototypes is based on a symmetric arrangement of two MWPCs with a double-sided central pad readout electrode (see Fig. 3.2).

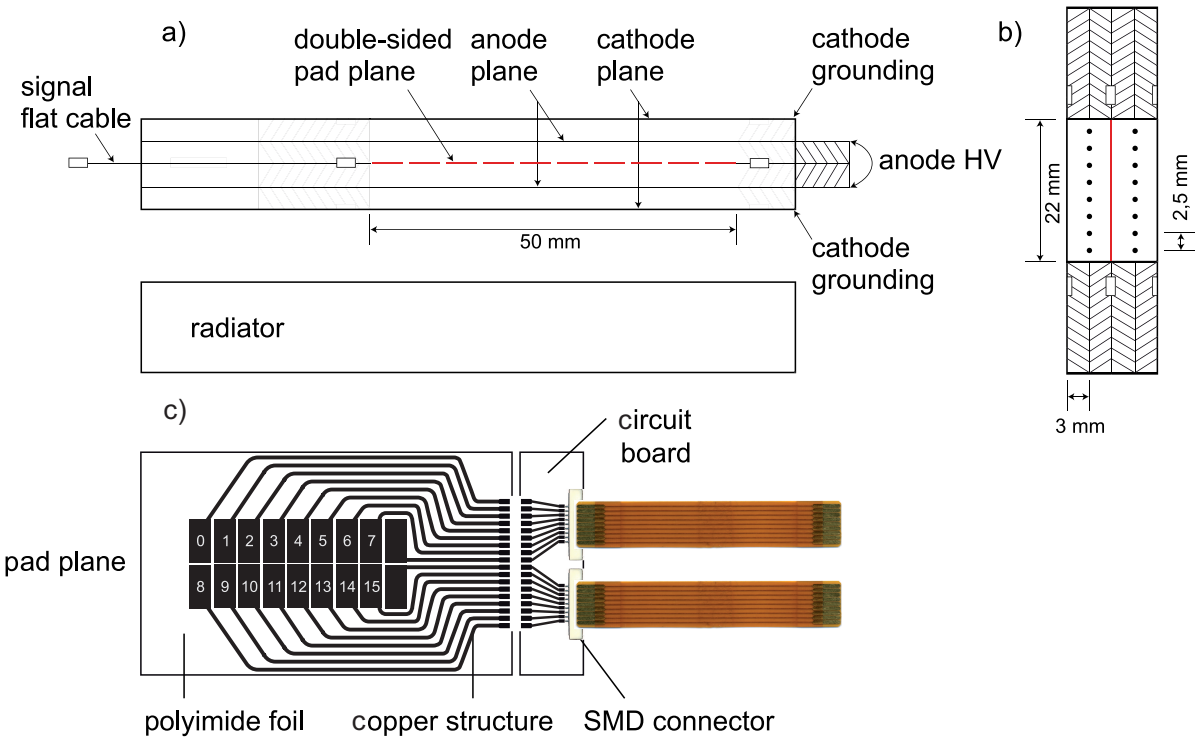

Fig. 3.2: Chamber layout: **a**) horiztontal lateral cut **b**) vertical lateral cut **c**) pad plane layout [KB09].

The detector is composed of two anode and two cathode frames, which are made of two 3 mm **P**oly**C**hlorinated **B**iphenyl (PCB) planes. The two anode wire planes are placed at either side of the central pad readout electrode (pad plane) fixed by two PCB planes. The pad plane is made of a 25 μm polyimide (Kapton) foil, coated with a 0.3 μm copper pad structure on both sides. The active detection area consists of two rows, each with 9 pads ($5 \times 10\,\mathrm{mm}^2$). The corresponding pads on both surfaces are connected on the edge of a circuit board to which also two flat ribbon cables for the signal transfer are connected. The wires are gold plated tungsten wires with a diameter of 25 μm and a wire pitch of $s = 2.5\,\mathrm{mm}$. One anode wire plane is shown in Figure 3.3 and the wires are numbered from 1 to 8. The anode-cathode gap $h = 3\,\mathrm{mm}$ has been optimized to provide appropriate charge sharing between adjacent pads. The entrance windows of 25 μm aluminized polyimide foil serve simultaneously as gas barrier and cathodes. The pads have a dimension of $H = 10\,\mathrm{mm}$ (height) and $W = 5\,\mathrm{mm}$ (width). A detailed description of the inner pad plane, a performance test of the MB-TRD Prototypes, and all engineering detail drawings can be found in the PhD thesis of Melanie Klein-Bösing [KB09].

3.2. Data Acquisition System

The pad signals are amplified with a 16-channel **A**pplication **S**pecific **I**ntegrated **C**ircuit (ASIC) preamplifier/shaper with a peaking time of about 70 ns and with a FWHM of about 70 ns. Further signals were digitized by an 8-bit nonlinear **F**lash **ADC** (FADC) system with 25 MHz sampling frequency (0.6 V swing and an adjustable baseline) in conjunction with an acquisition system which was developed for the in-beam tests of the ALICE TRD [A$^+$01]. The total time of 1.2 μs is sampled in 30 time bins (25 MHz).

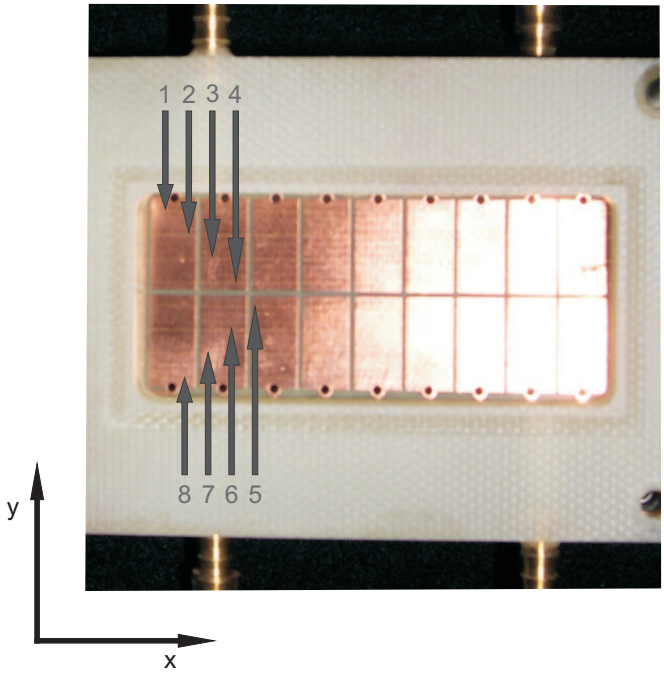

Fig. 3.3: Picture of the built-in pad plane with tensed anode wires (marked with gray arrows) [KB09].

3.3. Position Resolution (x,y)

The PRF is used to reconstruct the position of every cluster as mentioned in Chapter 2.4.2. To determine the y-coordinate the charge ratio CR of the two pad rows (pad number 0 to 7 and 8 to 15) can be used. For the determination of the position resolution the alignment of two identical prototypes can be calculated with the reconstructed cluster positions in both chambers x_{c1}, x_{c2}, y_{c1}, and y_{c2}. Subsequently, the distribution of the reconstructed x-coordinates can be fitted with two linear fits for both pad rows (see left half of Fig. 3.4). For a sample of tracks residuals, as the distribution of the distances between the reconstructed and the fitted values of the displacement between the cluster positions in the two chambers, can be defined. The position resolution of both chambers is given by the standard deviation of the Gaussian fit to this distribution (see right half of Fig. 3.4). Since the two prototypes are identical in construction, the same position resolution for both of them can be assumed. The position resolution of a single prototype is then given by $\sigma/\sqrt{2}$.

3.3.1. X-Coordinate

First, the pad signals are stored to determine the x-coordinate of a track via PRF. This is necessary to get the variance of the distribution as mentioned in Chapter 2.4.2 (see Eq. 2.42). The border pads (0, 7, 8, 15) have to be excluded to be the pad with maximum charge Q_i during the analysis of the data in order to have the signal on three adjacent pads (see Fig. 3.5). This leads to an unavoidable decrease of the active useable detector area corresponding to a decrease of 4% to 8% of used events during the test beam (see

[2] Run 92: Protons and Positrons, Anode Voltage $U = 1700\,\mathrm{V}$, Particle Momentum $p = 2.0\,\mathrm{GeV/c}$, Spill Length $S = 10\,\mathrm{s}$, Gas Mixture 90% Xe and 10% CO_2, Over all Event Rate (see Chapter A.1.1) $R_2 = 7.37 \cdot 10^{+1}\,\mathrm{kHz}$, Event Rate per Area $R_1 = 1.26 \cdot 10^{+1}\,\mathrm{kHz/cm^2}$

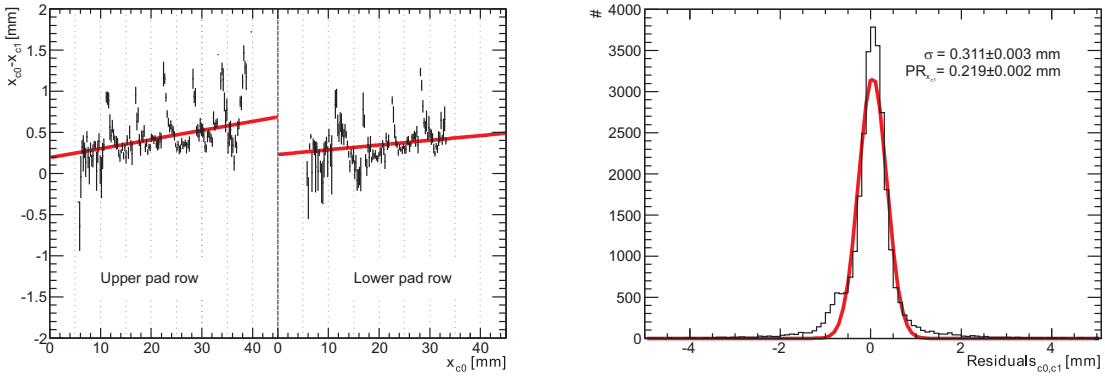

Fig. 3.4: Determination of the position resolution in x-direction
Left: Distribution of reconstructed cluster positions in both chambers (chamber 0 and chamber 1 for run 92[2]) x_{c0} and x_{c1} fitted to two linear fits for both pad rows.
Right: Distribution of the distances between the reconstructed and the fitted values of the displacement between the cluster positions in chamber 0 and chamber 1 for run 92, fitted by a Gaussian distribution.

right side of Fig. 3.17). The decrease of active detector area is true for all pad geometries, if equation 2.42 is used to reconstruct cluster positions. A detailed description can be found in the PhD thesis of Melanie Klein-Bösing [KB09]. The x-coordinate can be

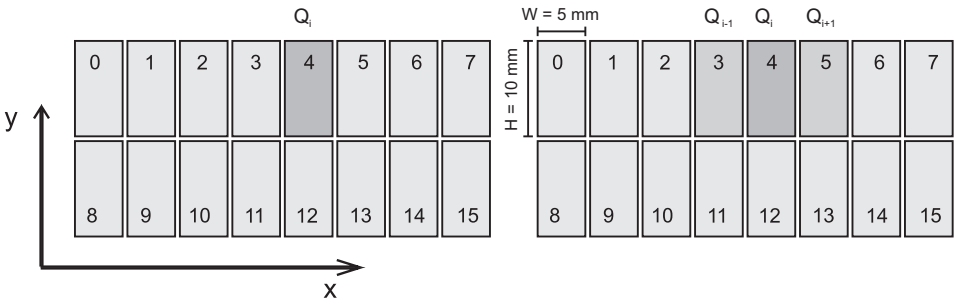

Fig. 3.5: Charge distribution for one event. The pad with maximum charge Q_i and the adjacent pads with charge Q_{i-1} and Q_{i+1} are dark gray-colored.

determined using Eq. 2.42

$$\begin{aligned} x &= \frac{W}{2} + (Wi + d) && i \in [0, 7], \\ x &= \frac{W}{2} + (W(i-8) + d) && i \in [8, 15]. \end{aligned} \tag{3.1}$$

The reconstructed x-position distribution for run 92 for the upper and lower pad row is shown in Figure 3.6. The peaks within the spectra located in the pad center are due to the so-called one-pad-cluster. One-pad-cluster induce charge only on one pad. Therefore, their position is reconstructed with $d \approx 0$.

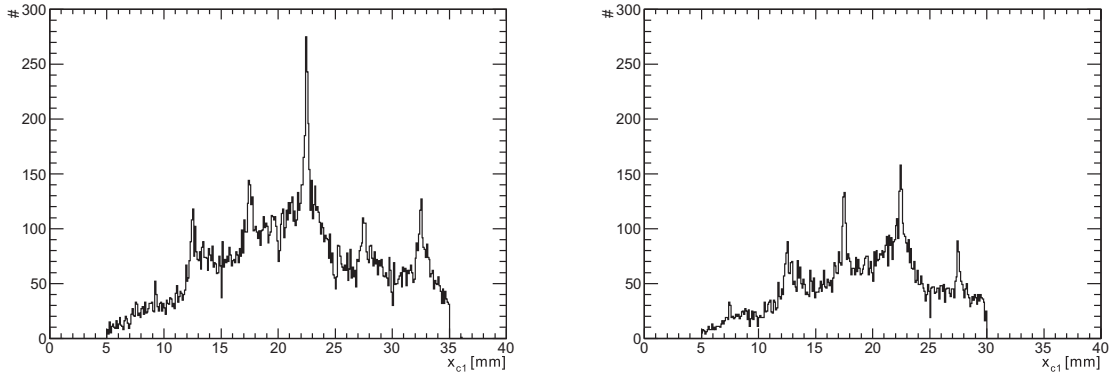

Fig. 3.6: X-position distribution (run 92, chamber 0) **Left**: $Q_i \quad i \in [0,7]$ **Right**: $Q_i \quad i \in [8,15]$

The position resolution of the small prototype depending on gas mixture, anode voltage, counting rate, and cut values (see Chapter 3.4) can be determined in the range of 180 to 500 μm by calculating the residuals of the alignment of two identical prototypes as mentioned in Chapter 3.3.

3.3.2. Y-Coordinate

One obvious option to determine the y-coordinate is to use the PRF (see [Mat88]). But Equation 2.39 cannot be used due to the fact that there are only two adjacent pads $(i, i \pm 8)$ as shown in Figure 3.7. Instead of using Equation 2.39, Equation 2.35 can be solved, if the pad with maximum charge is in the upper row

$$d_1 = \frac{\ln\left(\frac{Q_{i+8}}{Q_i}\right) \cdot 2\sigma^2 + H^2}{2H} \qquad i \in [0,7], \tag{3.2}$$

and else Equation 2.36

$$d_2 = \frac{\ln\left(\frac{Q_i}{Q_{i-8}}\right) \cdot 2\sigma^2 - H^2}{2H} \qquad i \in [8,15], \tag{3.3}$$

for d with H representing the pad height.

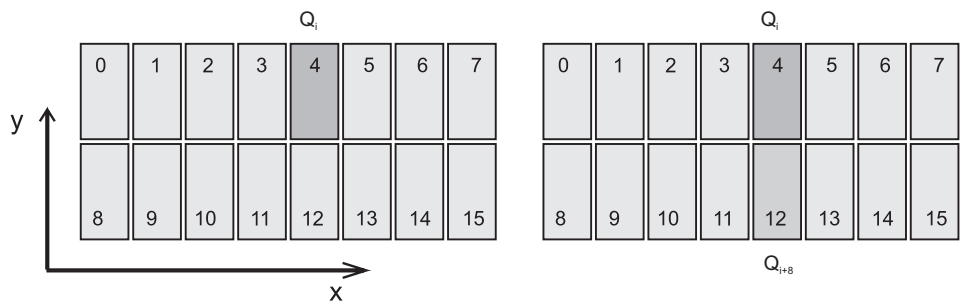

Fig. 3.7: Determination of the y-coordinate of a cluster using the PRF. In this example, the cluster induces maximum charge Q_i on pad 4. Therefore, the charge of pad 12 is choosen to be 'Q_{left}'.

The y-coordinate is given by

$$\begin{aligned} y &= -\frac{H}{2} - d_2 \qquad && i \in [0,7], \\ y &= +\frac{H}{2} - d_1 \qquad && i \in [8,15]. \end{aligned} \tag{3.4}$$

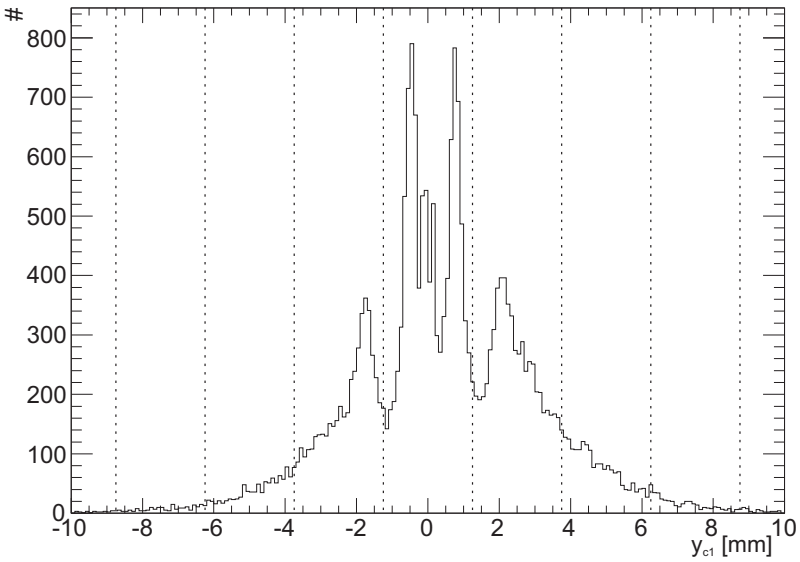

Fig. 3.8: Y-position distribution calculated using PRF: Positions < 0 pad $8-15$; Position > 0 pad $0-7$ (run 92, chamber 0); Dashed lines represent anode wire positions.

The accumulation points within the spectrum and the anode wire positions (see dashed lines in Fig. 3.8) do not overlap. This indicates a bad position reconstruction accuracy when using the PRF for only two adjacent pads. This problem can be avoided by using another method.
An other option to determine the y-coordinate is to make use of the percental charge ratio CR of the two pad rows,assuming that the cluster charge ditribution can be described by an axially symmetric Gaussian distribution. Subsequently, vertical pad groups are built in order to determine the charge distribution in x-direction (shown in Fig. 3.9).

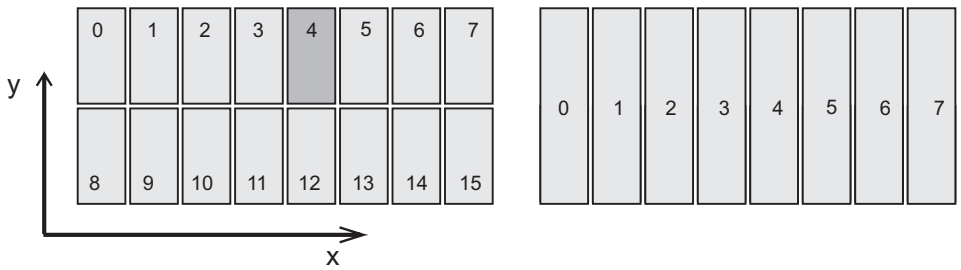

Fig. 3.9: Determination of the charge distribution by building five vertical pad groups surrounding the pad with maximum charge Q_i (dark gray-colored). The charge of the vertical pad groups is fitted to a Gaussian distribution.

The charge of the vertical pad groups is given by

$$Q_i^{Group} = Q_i + Q_{i+8} \qquad i \in [0,7], \tag{3.5}$$

and the charges from $Q_{(i-1)-1}^{Group}$ to $Q_{(i+1)+1}^{Group}$ are fitted to a Gaussian distribution

$$Q^{Fit}(x) = A \cdot \exp\left(-\frac{(x-\mu)^2}{2\sigma^2}\right). \tag{3.6}$$

In addition, it should be mentioned that the fit parameter μ is only used to calculate Q^{Event}, but not to determine $Q^{Fit}(y)$. μ can be taken as a first approximation of the x-coordinate of the cluster. In order to calculate the charge ratio CR the pad row including the pad with maximum charge Q_i (see Fig. 3.10) has to be identified

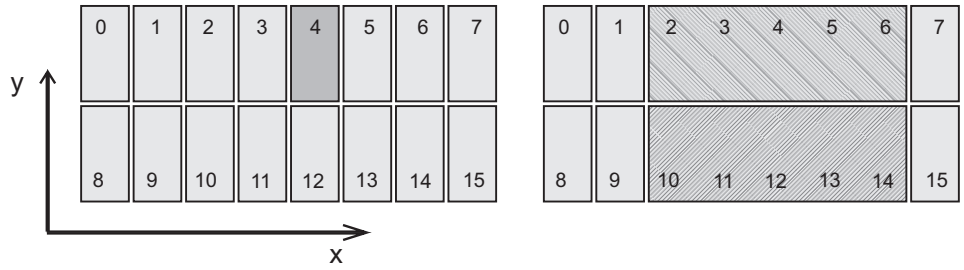

Fig. 3.10: Calculation of the charge ratio. After identifying the pad row including the pad with maximum charge Q_i , the charge of this pad row is calculated as a percentage of the whole cluster charge CR.

and the charge of this pad row is calculated as a percentage of the whole cluster charge CR.

$$CR = \frac{Q_{(i-1)-1} + ... + Q_{(i+1)+1}}{Q_{(i-1)-1} + ... + Q_{(i+1)+1} + Q_{(i-1)-(1\mp 8)} + ... + Q_{(i+1)+(1\pm 8)}} \tag{3.7}$$

One CR distribution is shown in Figure 3.11. CR is the initial point for the determination of the y-coordinate. It is assumed that the sum of five $Q^{Fit}(x)$ function values calculated for five equidistant x values with a distance equivalent to the pad width is equivalent to the whole cluster charge Q^{Event}:

$$\begin{aligned} Q^{Event} &= Q^{Fit}(-2W) + Q^{Fit}(-W) + Q^{Fit}(0) + Q^{Fit}(W) + Q^{Fit}(2W) \\ &\approx Q_{(i-1)-1}^{Group} + Q_{i-1}^{Group} + Q_i^{Group} + Q_{i+1}^{Group} + Q_{(i+1)+1}^{Group} \\ &= Q_{(i-1)-1} + Q_{i-1} + Q_i + Q_{i+1} + Q_{(i+1)+1} \\ &\quad + Q_{(i-1)-(1\mp 8)} + Q_{(i-1)\pm 8} + Q_{i\pm 8} + Q_{(i+1)\pm 8} + Q_{(i+1)+(1\pm 8)}. \end{aligned} \tag{3.8}$$

The ratio of any function value to this total charge $Q^{Fit}(y)/(Q^{Event})$ can be taken as theoretical CR. In this case $Q^{Fit}(y)$ can be characterized by the same fit parameters A and σ as $Q^{Fit}(x)$ (see Eq. 3.9):

$$Q^{Fit}(y) = A \cdot \exp\left(-\frac{y^2}{2\sigma^2}\right). \tag{3.9}$$

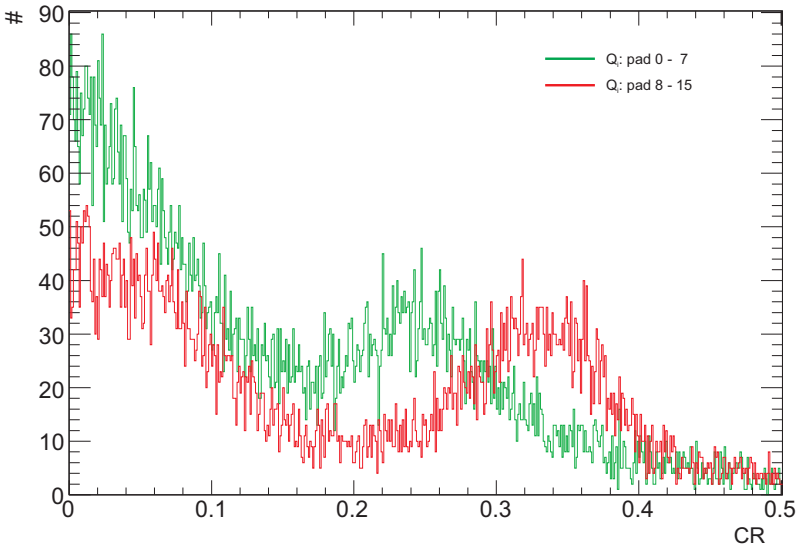

Fig. 3.11: Charge ratio (CR) spectrum (run 92, chamber 0) for the Q_i within the upper pad row green line and Q_i within the lower pad row red line.

This Gaussian curve $Q^{Fit}(y)$ is shifted along the y-direction until the measured charge ratio CR is reproduced. This is justified by the rather quadratic shape of the area covered by the pads, on which the charge is integrated. In addition, the integrated charge is equal along x- and y-direction when using the same pads for the charge integration. A histogram of y-coordinates determined by this method is shown in Figure 3.12.

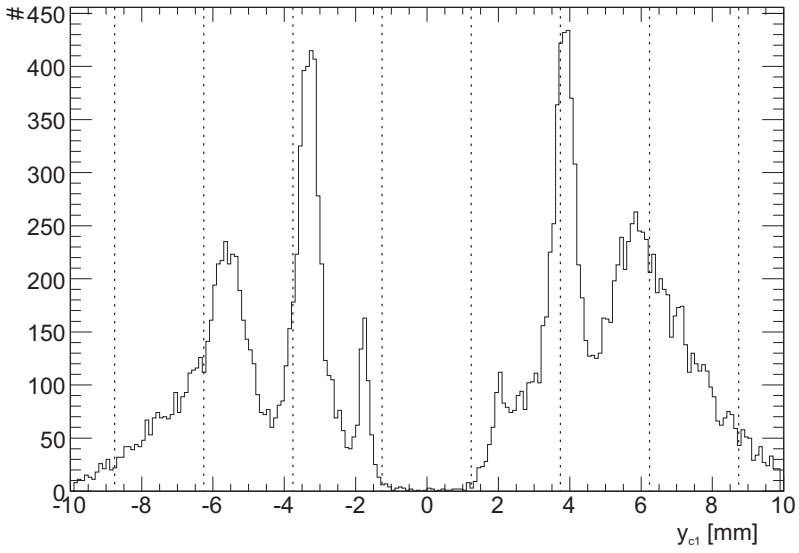

Fig. 3.12: Y-position distribution reconstructed using the CR method: Positions < 0 pad $8 - 15$; Position> 0 pad $0 - 7$ (run 92, chamber 0); Dashed lines represent anode wire positions.

The accumulation points within the spectrum are due to the wire positions. The primary electrons drift along the electric field lines. Near to the anode wires a drop like avalanche surrounds the wire. The electrons are collected by the wire and the positive

ions are left around the wire which leads to an induced signal on the pads. Therefore, it is only possible to determine the cluster position normal to the wire direction with a higher accuracy than the wire spacing. The cluster position parallel to the wire direction is shifted in direction of the next anode wire (see Chapter 2.3.1), which leads to the characteristic accumulation points of the spectrum. The resolution of the wire image gets worse at larger distances to the center of the chamber due to the decreasing charge sharing between the pad rows for non central cluster positions ($y < -6\,\text{mm}$ or $y > 6\,\text{mm}$). The peak width of the accumulation points is mainly correlated to the field strength and homogenity. The center of the accumulation points related to the wire positions can be used for a first estimation on the position resolution. By using this method, the position of the particle track can be related to the position of the closest wire. Therefore, it is not reasonable to determine the position resolution by calculating the residuals of the alignment of two identical prototypes as mentioned in Chapter 3.3. Thus, the position can be determined with a resolution of the order of the wire distance 2.5 mm divided by $\sqrt{12} \Rightarrow PR_y = 1.768\,\text{mm}$. Two reconstructed beam profiles are shown in Figure 3.13 and 3.14. The accumulation points around the anode wire

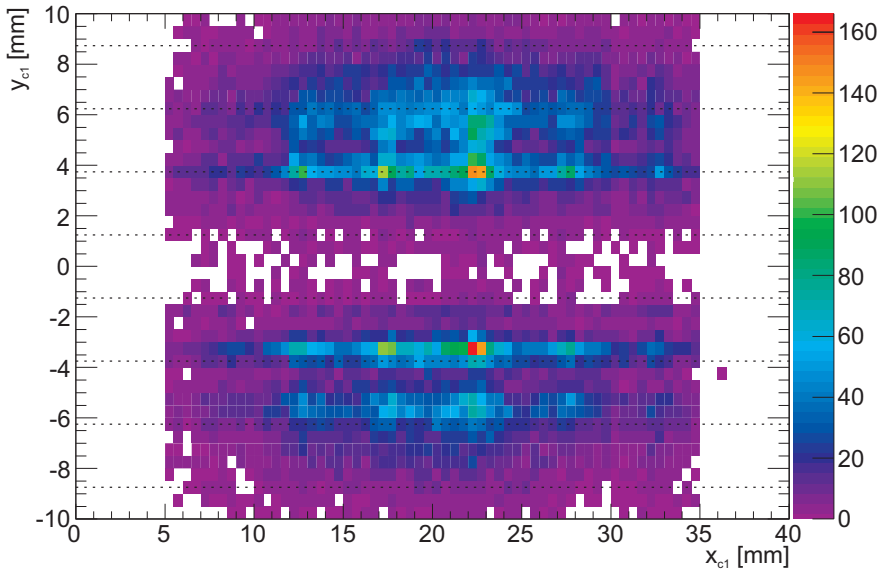

Fig. 3.13: The beam profile was reconstructed using the CR method (run 92, chamber 0). Dashed lines represent anode wire positions of the TRD.

positions (dashed lines) are clearly visible within the whole spectrum, as expected. The thinning of reconstructed positions around y_{c1} (see Fig. 3.13 or 3.14) is due to the charge sharing of the pad rows given by the anode wire positions. A mandatory requirement for a reconstructed cluster y-coordinate of approximately zero is a charge ratio CR of 0.5, which can only be realized by very broad charge distributions or an anode wire above the pad row separation line.

[3] Run 41: Pions and Electrons, Anode Voltage $U = 1700\,\text{V}$, Particle Momentum $p = 1.5\,\text{GeV/c}$, Spill Length $S = 10\,\text{s}$, Gas Mixture 85% Xe and 15% CO_2, Over all Event Rate (see Chapter A.1.1) $R_2 = 1.08 \cdot 10^{-2}\,\text{kHz}$, Event Rate per Area $R_1 = 1.90 \cdot 10^{-3}\,\text{kHz/cm}^2$

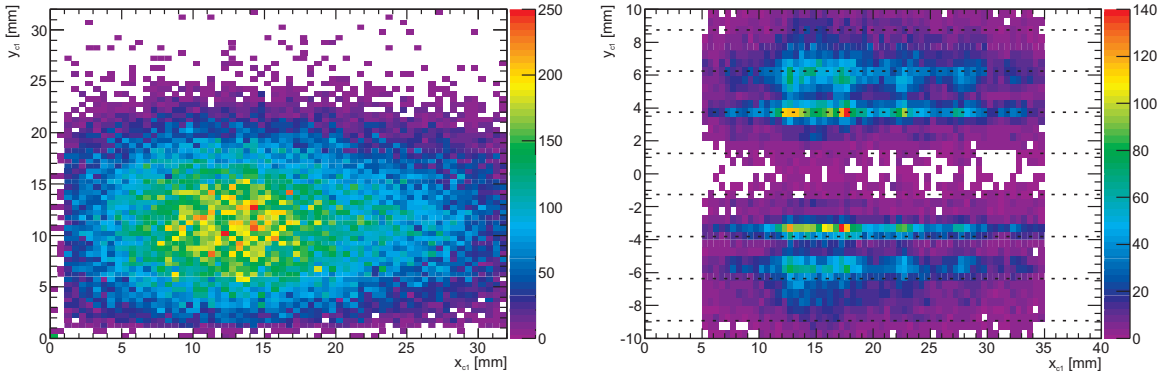

Fig. 3.14: Dashed lines represent anode wire positions; **Left**: Beam profile by the silicon tracking; **Right**: Reconstructed beam profile using *CR* method, measured by the TRD (run 41, chamber 0^3).

3.4. Cut Values

Noise is a random signal characteristic of all electronic circuits. In science, and especially in physics and telecommunication, noise means fluctuations in and the addition of external factors to the stream of target information (signal) being received at a detector. This electronic noise produced during the transmission and digitalization of the signal can be reduced to a minimum by optimization of the **D**ata **Acq**uisition (DAQ). In contrast to this kind of noise, the noise caused by unavoidable physical background, like radiation caused by radioactive isotope within the detector components, cosmic radiation, or multiple hits, remains. Before performing the analysis this noise has to be removed preliminarily from the data by threshold cuts. A certain amount of signal loss due to this cuts is unavoidable. Thus, an optimum of an acceptable noise level and minimum signal loss, which depends on the experimental requirements, has to be found. The following chapters will deal with so-called 'offline' data filters (cut values) and their effect on the position resolution, data efficiency, and pion efficiency of the small prototypes.

3.4.1. Time Bin Window

First of all, the **T**ime **B**in (TB) window range is chosen to reduce the noise within the first five time bins and the probability of multiple hits in a high counting rate environment, which increases with rising time bin number. Therefore, rejection of the last 15 time bins is reasonable. For the pad-charge integration in the following analysis, the signals in the time bin range [6, 15] is choosen, since the avalanche signal is located in this time region. The signal-to-noise ratio is calculated by dividing the integral of time bins [6, 11] by the integral of time bins [0, 5]

$$S/N = \sum_{j=6}^{10} TB_j / \sum_{k=0}^{5} TB_k \tag{3.10}$$

The average signal of pions, electrons, and the average signal of both are shown in Figure 3.15. In contrast to the electron TR signal spectrum of the ALICE TRD (see [Wil04]) with a long drift region, the increase of the electron signal by TR photons is located

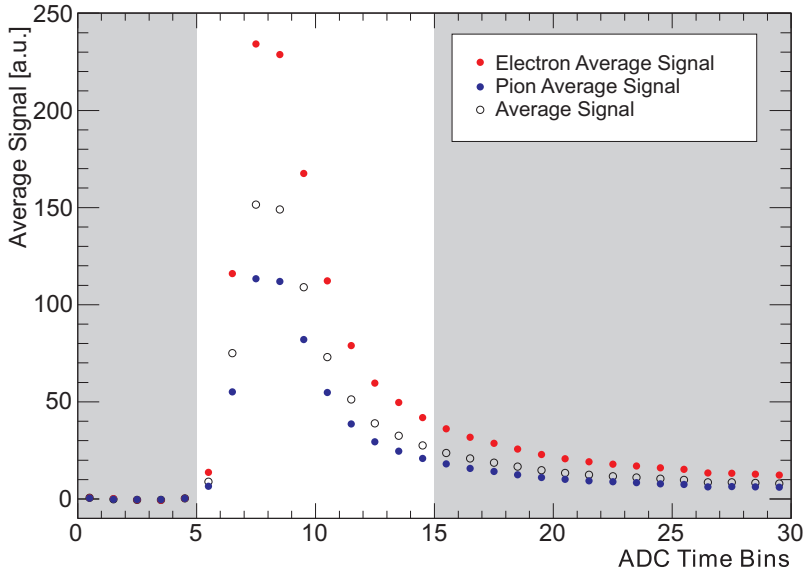

Fig. 3.15: Average Signal of electrons, pions, and the over all average signal determined in chamber 0, run 41.

within the same time bins of the CBM TRD signal spectrum as the ionization peak. Thus, the short time bin range is sufficient to separate electrons from pions.

3.4.2. Minimum Charge on Pad with Maximum Charge Cut (ec) and Minimum Charge on Cluster (tec)

For decreasing charge on the pad with maximum charge or charge of the cluster the charge sharing between adjacent pads decreases and the probability of being a non physical event increases. This can be seen by comparing the noise spectra of the pad with maximum charge and of the cluster (see Fig. 3.16).

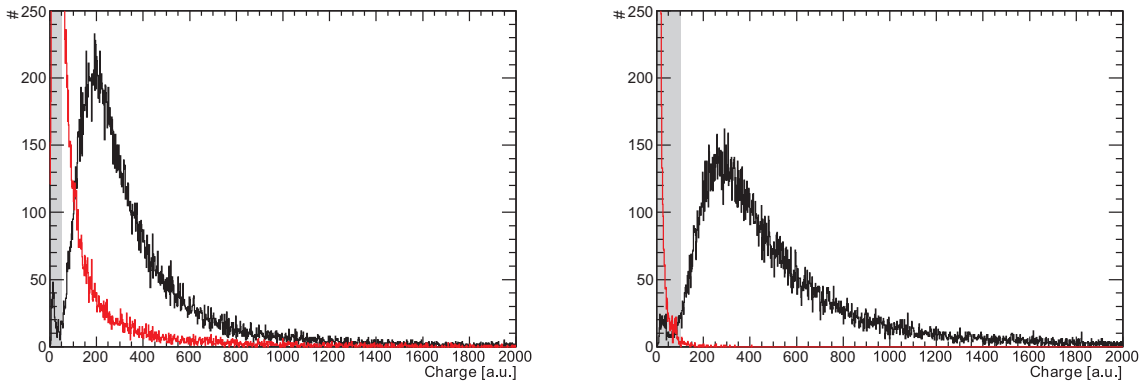

Fig. 3.16: Charge distribution chamber 0, run 92. **Left**: Charge on pad with maximum charge; Red line: Noise **Right**: Charge per Cluster; Red line: Noise.

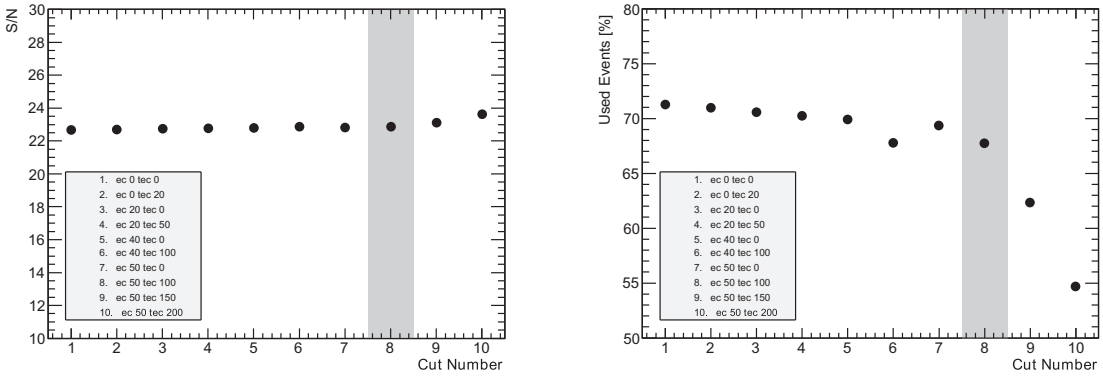

Fig. 3.17: Left: Signal to noise ratio; **Right**: Data efficiency quantified for several cuts (run 92, chamber 0).

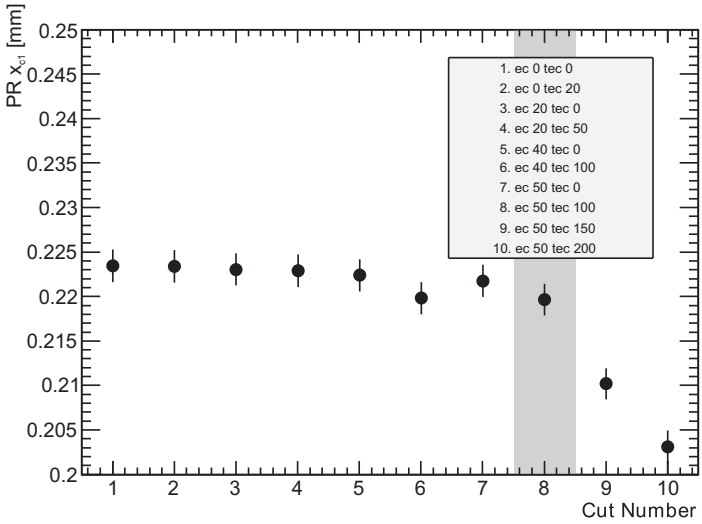

Fig. 3.18: Position resolution for several cuts for chamber 0, run 92.

The noise spectra are determined by integration of the time bin values in the range of [0, 4] on pad i,

$$\text{Noise}_i = \sum_{j=0}^{4} TB_j \tag{3.11}$$

or in case of cluster noise, on three adjacent pads $i-1, i, i+1$.

$$\text{Noise}^{\text{Cluster}} = \text{Noise}_{i-1} + \text{Noise}_i + \text{Noise}_{i+1} \tag{3.12}$$

This non-physical events are removed from the data sample by a minimum charge threshold applied to the maximum charge data per event and the cluster charge data per event. The cut value is chosen by comparing S/N ratio, data efficiency (see Fig. 3.17), and the achieved position resolution (see Fig. 3.18). For the following position resolution data analysis $ec = 50$ and $tec = 100$ is used. For this cut values an increase of S/N (< 1), a small decrease of data efficiency to 67%, and an improvement in PR of the x-coordinate by 0.003 mm is achieved. Higher cut values are not recommended due to the decrease of data efficiency.

3.4.3. Cluster Quality Cut (CQC)

Multiple hits, which can occur at very high particle rates, lead to a decrease of the measured position resolution. Th multiple hits can be reduced by a cut on the charge ratio of the adjacent pads $(Q_{i-1} \cdot Q_{i+1})/Q_i^2$. Due to the additional deposited charge, the probability of multiple hits increases with increasing deviation from the mean charge ratio (see Fig. 3.19). It is important to find reasonable cuts in order not to prefer

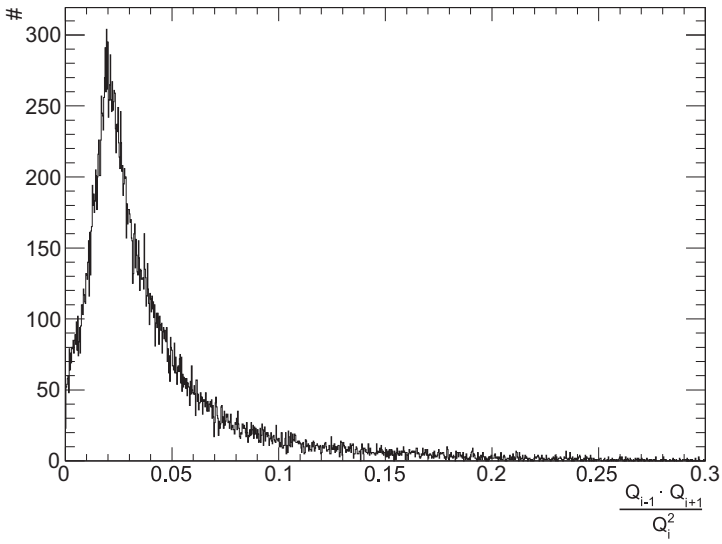

Fig. 3.19: Charge ratio $(Q_{i-1} \cdot Q_{i+1})/Q_i^2$ spectrum (run 92, chamber 0).

certain cluster positions for the determination of the position resolution. First of all the influence of the point of appliance of this filter has to be analyzed. It can be seen that the accumulation point of the distribution is sharply peaked at small values range of $(Q_{i-1} \cdot Q_{i+1})/Q_i^2$ values ($[0.01, 0.05]$) and $Q_i/(Q_{i-1} + Q_i + Q_{i+1})$ values ($[0.01, 0.05]$). By applying the **C**luster **Q**uality **C**ut (CQC) to the PRF histogram, a sharp localized area of the histogram is cut-off. This leads leads to a deformation of the one-dimensional average histogram and the increase of the non-Gaussian character of the distribution (see Fig. 3.20).

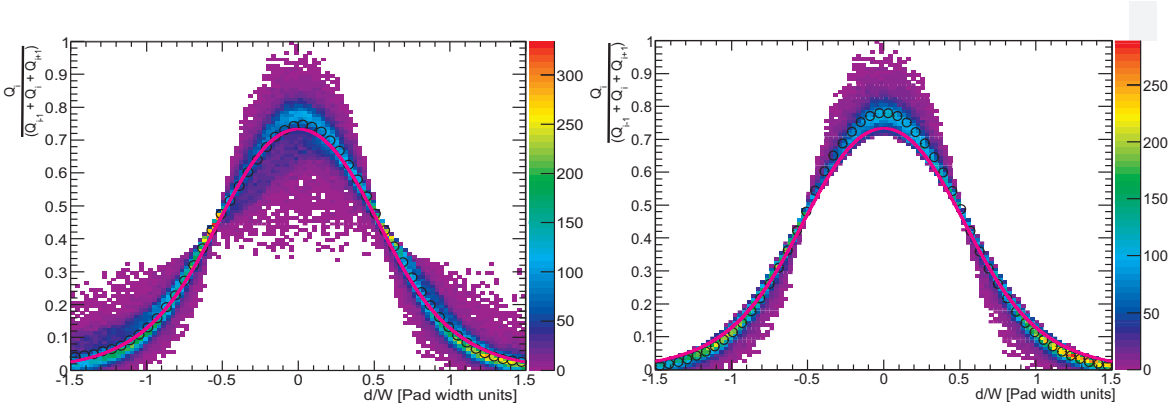

Fig. 3.20: PRF spectrum: **Left**: $CQC = 1.00$ PRF and (run 92, chamber 0); Purple: Mathieson formula; Black: 1dim PRF; **Right**: $CQC = 0.04$ PRF and (run 92, chamber 0); Purple: Mathieson formula; Black: 1dim PRF.

This has an effect on the PR (see Eq. 2.42) due to the deformation of the PRF distribution, the modification of the Gaussian fit parameter σ (see Fig. 3.20), and the increasing deviation of the PRF from the theoretical Mathieson formula.

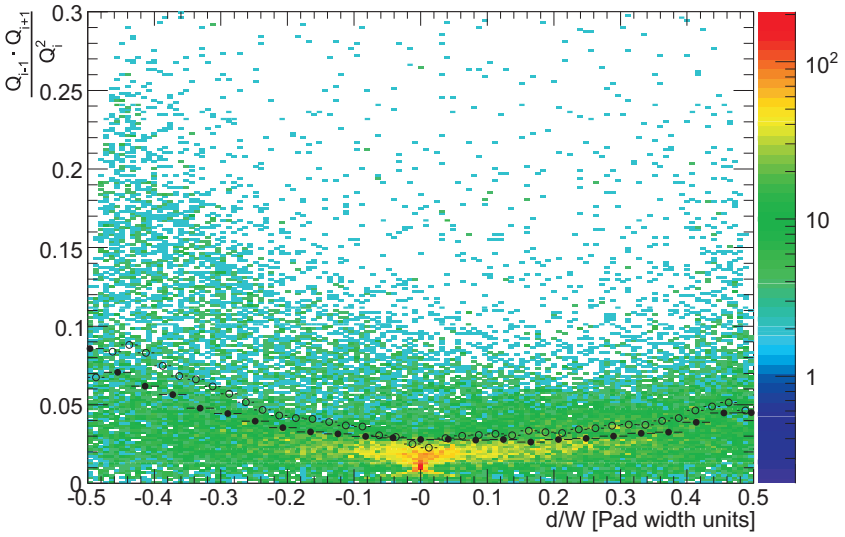

Fig. 3.21: Correlation of charge ratio/position. All dots above the black markers have a higher probability to be a multiple hit (run 92, chamber 0).

• : Average charge ratio calculated from the PRF $CQM = \dfrac{\langle PRF(x-1)\rangle \cdot \langle PRF(x+1)\rangle}{\langle PRF(x)\rangle^2}$;

◦ : Average charge ratio $CQM = \dfrac{\langle Q_{i-1}(x-1)\rangle \cdot \langle Q_{i+1}(x+1)\rangle}{\langle Q_i(x)\rangle^2}$.

Thus, it is reasonable to apply this filter after calculating and fitting the PRF. The PRF can be used to get a dynamic CQC as function of the cluster position. With the measured PRF, a cluster-quality measure (CQM) can be calculated to separate isolated clusters from shared clusters (see Fig. 3.21):

$$CQM = \left\langle \frac{PRF(x-1) \cdot PRF(x+1)}{PRF(x)^2} \right\rangle \tag{3.13}$$

with $Q_{Sum}(x) = Q_{i-1}(x-1) + Q_i(x) + Q_{i+1}(x+1)$,

$$= \left\langle \frac{\dfrac{Q_{i-1}(x-1)}{Q_{Sum}(x)} \cdot \dfrac{Q_{i+1}(x+1)}{Q_{Sum}(x)}}{\left(\dfrac{Q_i(x)}{Q_{Sum}(x)}\right)^2} \right\rangle \tag{3.14}$$

$$= \left\langle \frac{Q_{i-1}(x-1) \cdot Q_{i+1}(x+1)}{Q_i(x)^2} \right\rangle$$

$$\leq \frac{\langle Q_{i-1}(x-1)\rangle \cdot \langle Q_{i+1}(x+1)\rangle}{\langle Q_i(x)\rangle^2}. \tag{3.15}$$

This shared clusters are supposed to have a charge ratio above average, but there is no theoretical model to predict the relationship between the probability to be a shared cluster and the charge ratio. To give a first estimation on the usefulness of the dynamic

CQC, the average charge ratio of all runs was fitted to a polynomial $CQC(x) = p[0] \cdot (x + p[1])^2 + p[2]$, which was then chosen as cut value (see Fig. 3.22). The effect on the position resolution, S/N event efficiency, and average cluster width of the used events, is shown in Figure 3.23. The dynamic CQC provides an increase in PR comparable to the best achievable PR using a static $CQC = 0.05$ with a better event efficiency and equal S/N and average cluster width.

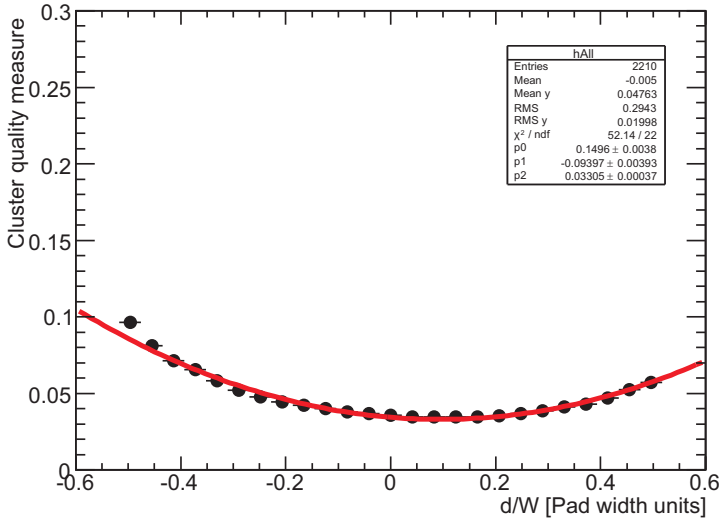

Fig. 3.22: Avarage charge ratio for all runs correlated to the reconstructed track position on PadMax, fit: $CQC(x) = 0.1496 \cdot (x - 0.09397)^2 + 0.03305$.

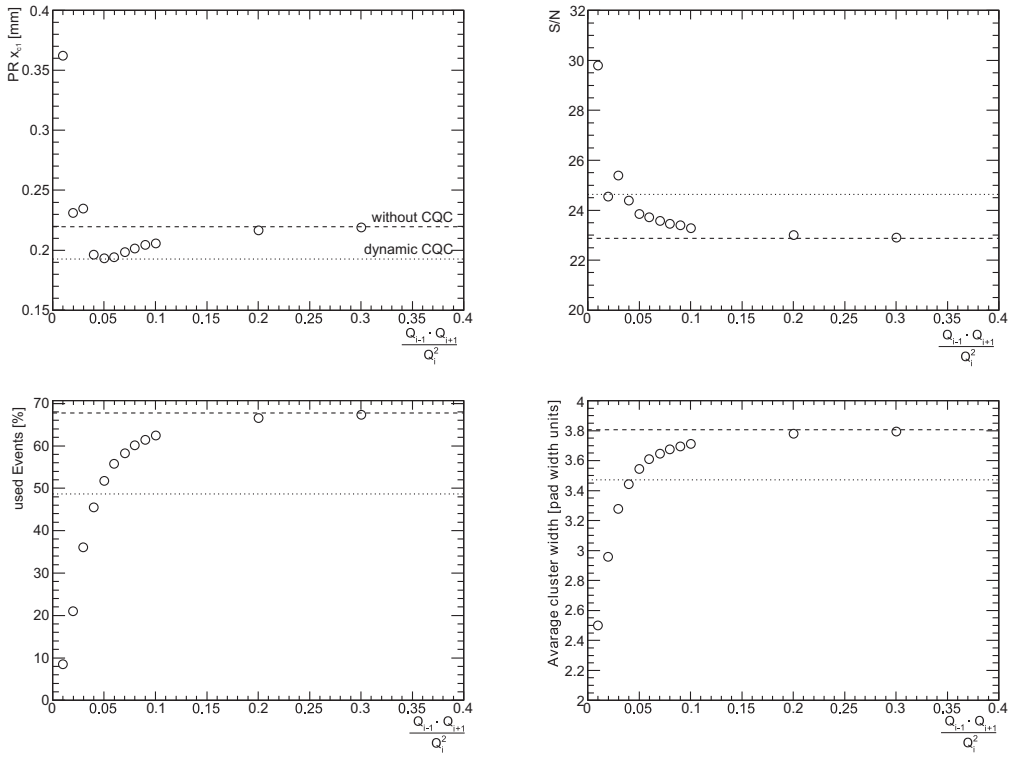

Fig. 3.23: Effects of the dynamic CQC applied after calculating the PRF. Dashed lines: Value for run 92 without CQC; Pointed lines: Values with dynamic CQC; **Upper left**: Position resolution; **Upper right**: S/N; **Lower left**: Event efficiency; **Lower right**: Average cluster width.

3.5. Particle Rate

One big technical challenge for the CBM TRD is to cope with very high counting rates up to 100 kHz/cm^2 in the central part of the detector. Therefore, for measuring the rate dependence of the **P**osition **R**esolution (PR) of small prototypes, different anode voltages and gas mixtures were chosen to find an optimum configuration. To determine the event rate, the beam area has to be calculated. The beam profile can be assumed to be elliptical as shown in Figure 3.14. To evaluate the average event rate per area in the central beam area, the beam profile is fitted to a Gaussian distribution to determine the width σ in x- and y-direction. This width in one direction is $\sqrt{2\ln(2)}$ times the FWHM/2 value which is assumed to be one semiaxis of the ellipse of the central beam profile area. The area of an ellipse is given by

$$A = \pi a b, \tag{3.16}$$

a representing the semimajor axis,

$$a = \sqrt{2\ln(2)}\sigma_x \tag{3.17}$$

and b representing the semiminor axis of the ellipse,

$$b = \sqrt{2\ln(2)}\sigma_y. \tag{3.18}$$

Only events within this ellipse given by

$$\frac{(x-\mu_x)^2}{a^2} + \frac{(y-\mu_y)^2}{b^2} = 1, \tag{3.19}$$

are used to determine the counting rate. Since there are no data taken with the Si_1-Si_1-counter and Pb-glass detector for every test beam run, the beam area is determined for a small sample of runs and the average area

$$\langle A \rangle = (291.72 \pm 25.29)\,\mathrm{mm}^2 \tag{3.20}$$

is used for the rest (see Tab. A.1). A Monte Carlo integration was used to determine the fraction of events within the used area of the ellipse.

$$\int_{x_1}^{x_2}\int_{y_1}^{y_2} \frac{1}{\sqrt{2\pi}} \exp\left(-\frac{1}{2}\left(\left(\frac{x-\mu_x}{\sigma_x}\right)^2 + \left(\frac{y-\mu_y}{\sigma_y}\right)^2\right)\right) dx\, dy \approx 0.500042 \tag{3.21}$$

$$\text{with } x_1 = -\sqrt{\left(1 - \frac{(y-\mu_y)^2}{b^2}\right)a^2} + \mu_x, \qquad x_2 = +\sqrt{\left(1 - \frac{(y-\mu_y)^2}{b^2}\right)a^2} + \mu_x,$$

$$y_1 = -\sqrt{\left(1 - \frac{(x-\mu_x)^2}{a^2}\right)b^2} + \mu_y \text{ and } y_2 = +\sqrt{\left(1 - \frac{(x-\mu_x)^2}{a^2}\right)b^2} + \mu_y.$$

The total rate per area (R_1) is given by

$$R_1 = \frac{0.500042 \cdot E}{A \cdot S}, \tag{3.22}$$

and the over all rate (R_2) by

$$R_2 = \frac{E}{S}. \tag{3.23}$$

E represents the particles measured by the first (Si_1) and second Silicium counter (Si_2) and the Pb-glass detector (Pb), A represents the beam area within the ellipse given in mm^2 and S represents the spill length given in seconds. The results and some useful properties are demonstrated in Figure 3.24. The best PR of 0.179 ± 0.002 mm could

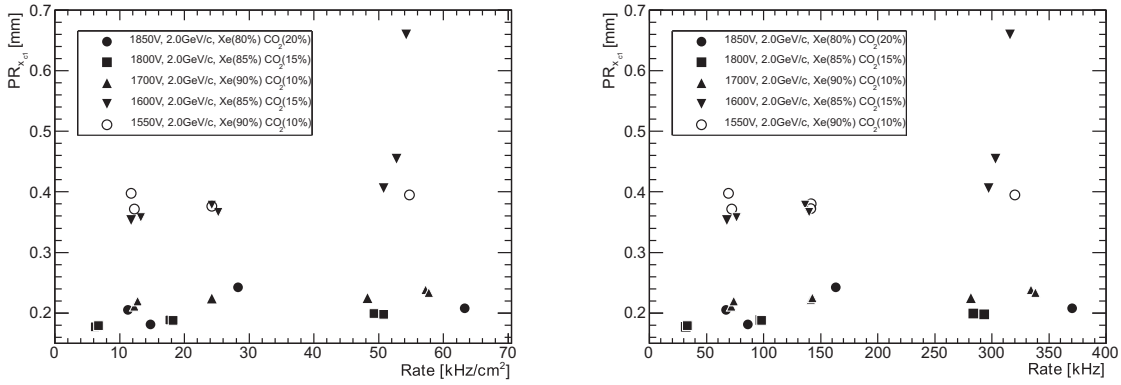

Fig. 3.24: Rate dependence of the position resolution for different anode voltages and gas mixtures: **Left**: Total rate per area R_1; **Right**: Over all rate R_2, used runs are gray-colored in Tab. A.1. Data points are drawn without x- and y-error bars for improved clarity. Errors of position resolution are of the order of 1 - 3% and errors of rate R_1 are of the order of 1-5%.
● : 1850 V, 2 GeV/c, Xe(80%) CO_2(20%) ■ : 1800 V, 2 GeV/c, Xe(85%) CO_2(15%)
▲ : 1700 V, 2 GeV/c, Xe(90%) CO_2(10%) ▼ : 1600 V, 2 GeV/c, Xe(85%) CO_2(15%)
○ : 1550 V, 2 GeV/c, Xe(90%) CO_2(10%)

be obtained by using a gas mixture of Xe(85%) CO_2(20%), an anode voltage of 1800 V, and $p = 2$ GeV/c particles. For this conditions, the PR was almost steady for different particle rates between 1 and 70 kHz/cm^2. The remainder of the data samples, using other conditions like an anode voltage smaller than 1800 V and gas mixtures between Xe(90%) CO_2(10%) and Xe(80%) CO_2(20%), show a moderate decreasing of PR for increasing particle rates. A strong dependence of PR on the anode voltage and gas mixture is pointed out by this data sample, whereas there are not enough samples to determine the effect of different gas mixtures and anode voltages independently.

3.6. Electron-Pion-Separation using LQ-Method

One of the major tasks of the CBM TRD is to distinguish between electrons (and positrons) and pions. This separation in the TRD is based on the differential energy deposition inside of the TRD. Electrons loose energy by ionization plus TR whereas other particles like pions loose energy only by ionization. The electron and pion events are identified and selected off-line by using the correlation between the signals measured by

the Cherenkov and the lead-glass detectors in the test-beam data as shown in Figure 3.25. Electrons can be separated from pions by their larger energy loss in both detectors (see Chapter 2.1) by threshold cuts represented by the lines in Figure 3.25. For decreasing

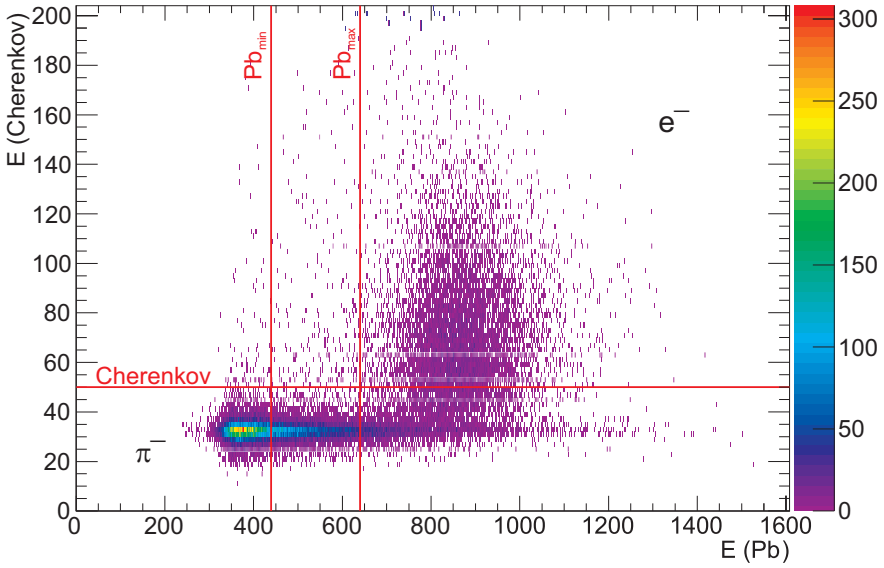

Fig. 3.25: Energy loss in the Pb-glass detector plotted versus energy loss in the Cherenkov detector in order to find the most efficient threshold values for the e^- and π^- separation. Cut and separation thresholds: $(Pb_{min} = 440, Pb_{max} = 640; Cherenkov = 50)$ run 41, chamber 0, particle momentum $p = 1.5\,\mathrm{GeV/c}$.

particle beam momentum (electrons and pions have the same momentum in the test beam) the energy loss of electrons and pions converge which makes it difficult to separate them. It is advantageous to use two thresholds in the Pb-glass calorimeter (Pb_{min}, Pb_{max}) to obtain cleaner samples of both particle species, since the electron and pion signal regions in this detector overlap. The Cherenkov detector readout is triggered by the scintillator counters and the Pb-glass detector.

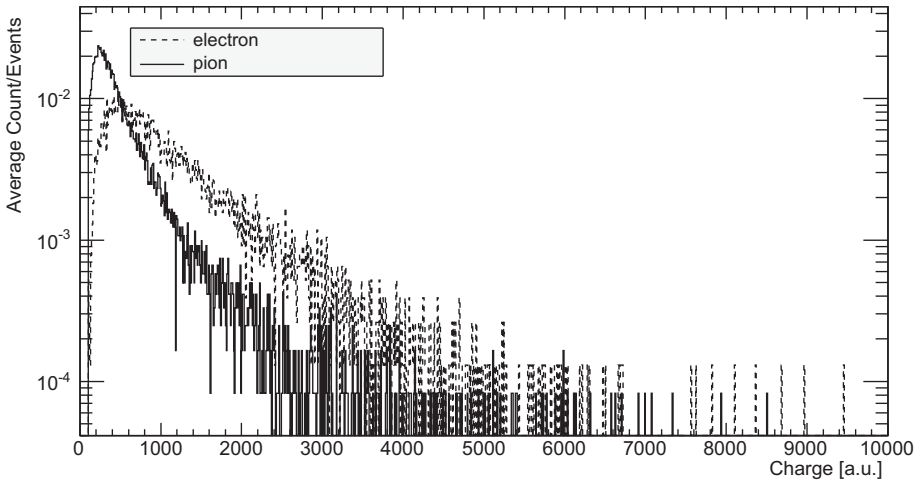

Fig. 3.26: Integrated normalized charge distributions of electrons (dashed line) and pions (solid line). Integrated signal on three adjacent pads.

In Figure 3.26, the normalized distributions of the integrated charge (the sum on three adjacent readout pads $i-1, i, i+1$) measured by the TRD prototype are shown for electrons and pions identified by the Cherenkov and the Pb-glass detectors. Pions of some GeV are minimum ionizing particles in contrast to electrons, which are already in the Fermi plateau. Therefore, the average electron signal in this momentum region is larger than the pion signal, irrespective of the detector. In addition, it has to be mentioned that the electron signal measured by the TRD prototype is shifted towards higher values due to the extra TR signal produced in the radiators in front of the TRD chamber.

3.6.1. Pion Efficiency

The normalized charge distributions of electrons and pions (see Fig. 3.26) can also be interpreted as probability distributions in order to determine the pion-rejection factor of the TRD prototypes. Electrons and pions have a probability $P(E)$ equivalent to the normalized count $C(E)$ to deposit the energy E in the detector. Assuming that the measurements are independent, the pion-rejection factor can be extrapolated to n detector layers by the measured normalized charge distributions of one chamber. E_n^e and E_n^p are sampled for electrons and pions random energy losses according to the measured charge-loss spectra in order to determine the probability that this energy E_n is deposited in detector layer n by an electron ($P^n(E_n \mid e)$) or a pion ($P^n(E_n \mid \pi)$). The total probability for an electron to produce a tuple of energy losses $E = \{E_1, ..., E_n\}$ within n detector layers is [Wil04]:

$$P_e(E) = \prod_{n=1}^{10} P^n(E_n \mid e) = \prod_{n=1}^{10} P(E_n \mid e). \tag{3.24}$$

$P = P^n$ is justified for n identical and independent layers. The total probability for pions can be calculated correspondingly [Wil04]:

$$P_\pi(E) = \prod_{n=1}^{10} P^n(E_n \mid \pi) = \prod_{n=1}^{10} P(E_n \mid \pi). \tag{3.25}$$

The relative probability L_e (likelihood) to be an electron corresponding to the random numbers E_n^e can be calculated using the values for the total probabilities for electrons [Wil04]:

$$L_e = \frac{P_e(E^e)}{P_e(E^e) + P_\pi(E^e)}, \qquad \text{with } \; 0 \leq L_e \leq 1. \tag{3.26}$$

The relative probability for a pion to be identified as an electron is [Wil04]:

$$L_e = 1 - L_\pi = \frac{P_e(E^\pi)}{P_e(E^\pi) + P_\pi(E^\pi)}, \qquad \text{with } \; 0 \leq L_e \leq 1. \tag{3.27}$$

A large number of electron and pion events are required for the determination of the pion suppression factor. The electron efficiency ϵ_e gives the fraction of accepted electrons. The number of misidentified pions at a given ϵ_e is defined to be the pion

efficiency. The pion suppression is given by $1/\epsilon_\pi$. Typically, an ϵ_e of 90% is used. This process is illustrated in Figure 3.27.

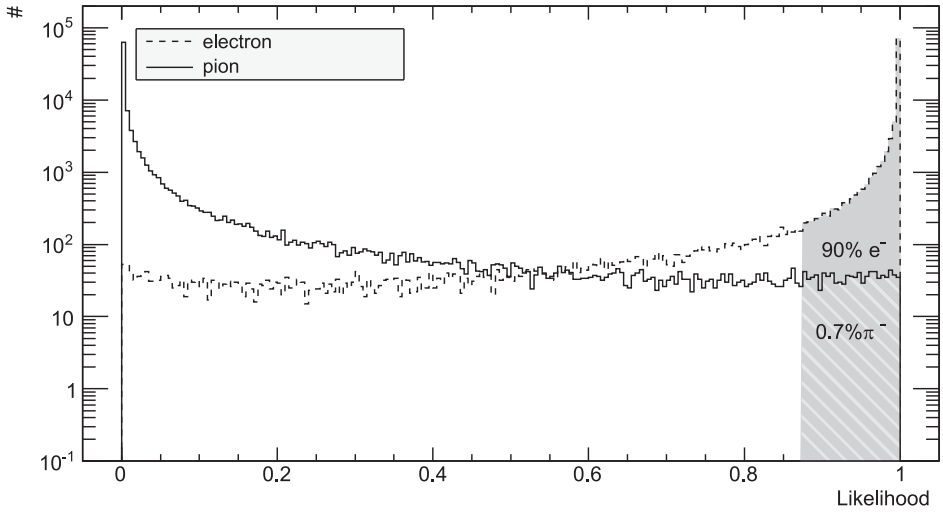

Fig. 3.27: Likelihood distribution of electrons (dashed line) and pions (solid line). The electron entries are integrated from the right until 90% of all electrons are included (gray region), (6.84% pions included). Approximation for 10 detector layers.

The likelihood distribution of electrons f^e is integrated until the integral includes 90% of the electrons with the highest likelihood values [Wil04]:

$$0.9 = \frac{\int_{L_{\epsilon_e=90\%}}^{1} f^e(L_e)}{\int_0^1 f^e(L_e)}, \tag{3.28}$$

The pion efficiency is the fraction of pions included by the integration limits for 90% of the electrons [Wil04]:

$$\epsilon_\pi = \frac{\int_{L_{\epsilon_e=90\%}}^{1} f^\pi(L_e)}{\int_0^1 f^\pi(L_e)}. \tag{3.29}$$

A compromise between between an acceptable signal loss and a sufficient pion efficiency, which depends on the experimental requirements, has to be found. The pion efficiency of 1% at an electron efficiency of 90% has to be achieved for the CBM-TRD. The pion efficiency can be increased by choosing Pb_{min} and Pb_{max} with a sufficient gap. This leads to a decrease of the data efficiency in the range of 7%. An additional enhancement of the Cherenkov threshold value reduces the data efficiency by 4%. The best compromise between data efficiency and pion efficiency is reached for $Pb_{min} = 440$, $Pb_{max} = 640$, and $Cherenkov = 50$ (see Fig. 3.28). A pion efficiency of 1% can be reached by using ten detector layers.

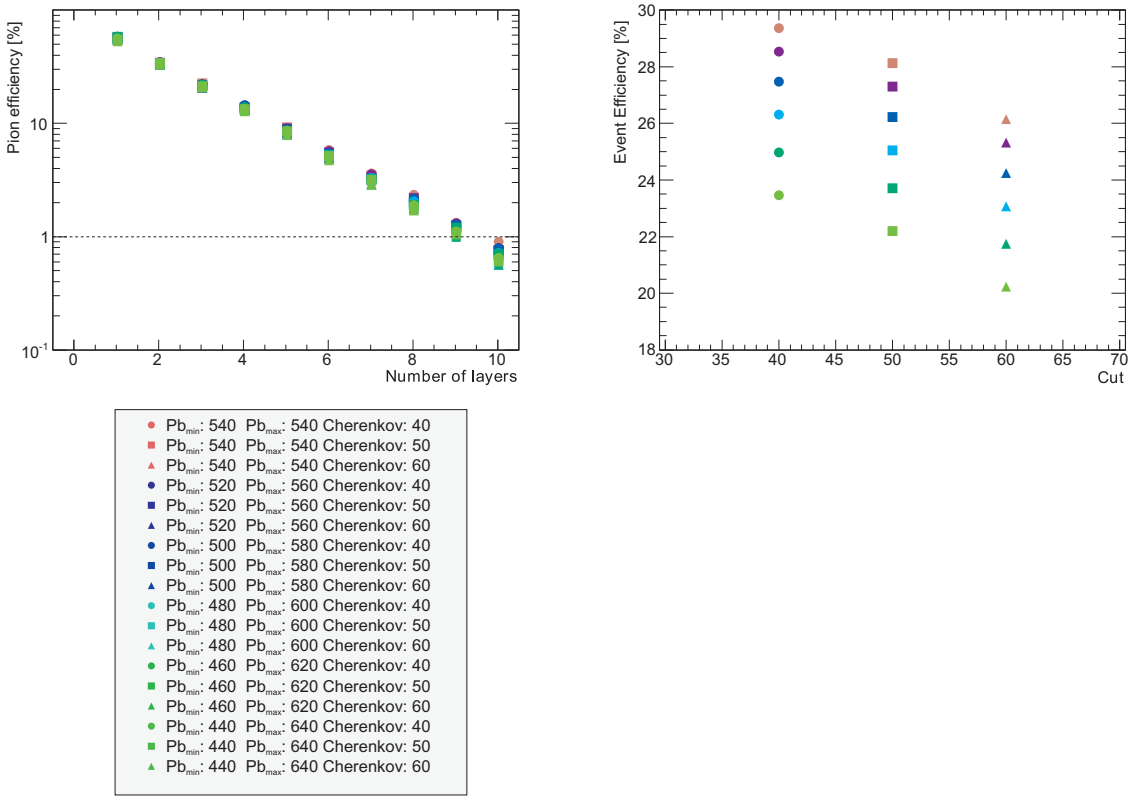

Fig. 3.28: Left: Pion efficiency, **Right**: Data efficiency: Pions and electrons within the thresholds Pb_{min}, Pb_{max}, and $Cherenkov$ divided by all pions and electrons approximation for different numbers of detector layers and different Pb_{min}, Pb_{max}, and $Cherenkov$ threshold values.

The pion efficiency, depending on different minimum charge on pad with maximum charge cut (ec) and minimum charge on cluster (tec) values, is shown in Figure 3.29.

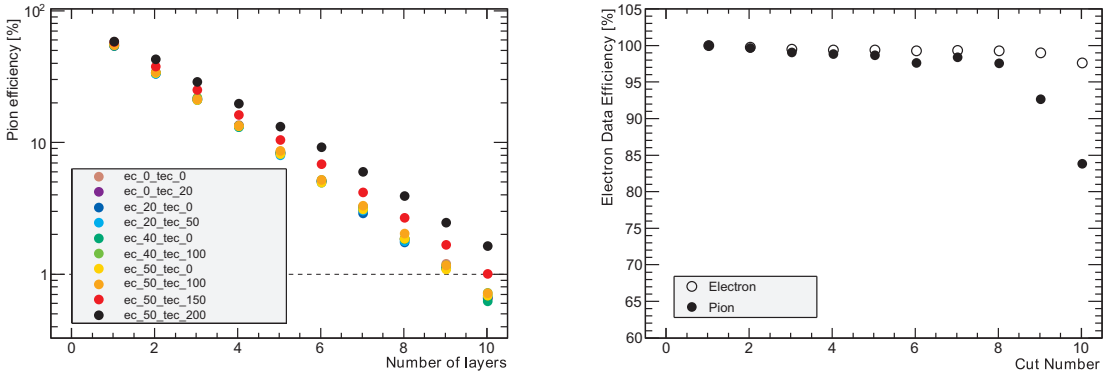

Fig. 3.29: Left: Pion efficiency approximation for different numbers of detector layers and different ec and tec threshold values ($Pb_{min} = 440$, $Pb_{max} = 640$; $Cherenkov = 50$).
Right: Data efficiency: Pions and electrons within the ec and tec threshold values divided by all pions and electrons within the thresholds Pb_{min}, Pb_{max}, and $Cherenkov$.

It can be seen, that a strong correlation between increasing values of both thresholds and the pion efficiency exists. This correlation has an opposing trend in comparison to

the increasing PR of rising threshold values (see Fig. 3.18). This can be interpreted as an effect of diverging data samples for pions and electrons as shown in the right histogram of Figure 3.18. More pions are rejected by this cut thresholds due to their smaller average energy loss within the detector volume. Finally, the pion efficiency can be optimized by using the CQC. A pion efficiency of 1% can be reached by using eight detector layers, if the *dynamic* CQC is applied to the data. Similar to the effect of the *dynamic* CQC on the PR it effects the pion efficiency (see Fig. 3.30). Due to the worse over all data efficiency of the static CQC (see Fig. 3.23) at a charge ratio of 0.05 ($\geq$ 50%), the dynamic CQC ($\approx$50%), and the reduced data sample by previous thresholds like Pb_{min}, Pb_{max} and $Cherenkov$, it does not seem to be sensible to use the static CQC to determine the pion efficiency or to identify $\geq$ 45% of the electrons.

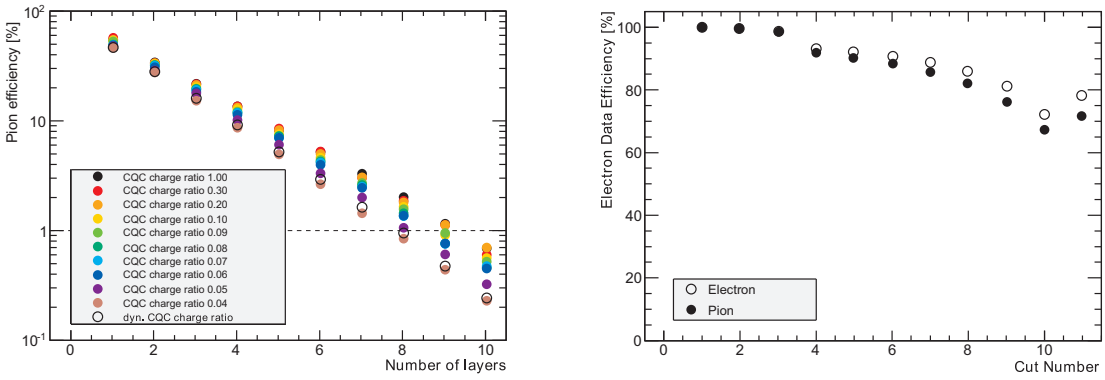

Fig. 3.30: Left: Pion efficiency approximation for different numbers of detector layers and different CQC threshold values. Event efficiency can be found in Fig. 3.23. Cut and separation threshold values: ($ec = 50$, $tec = 100$), ($Pb_{min} = 440$, $Pb_{max} = 640$; $Cherenkov = 50$) **Right**: Data efficiency: Pions and electrons within the CQC threshold values divided by all pions and electrons within the thresholds Pb_{min}, Pb_{max}, and $Cherenkov$.

4. Real-Size Prototype

In contrast to the small prototypes the new real-size prototypes are technically equivalent to the present design concept of a TRD in the CBM experiment. They are designed to feature a two-dimensional position reconstruction in one detector layer and a pion suppression factor of the order of 100 at 90% electron efficiency. The double-sided read-out pad plane concept with a gas volume of 12 mm thickness, an anode wire separation (3 mm), and an anode cathode gap (3 mm) are retained (see Chapter 3.1) due to a good performance of electron/pion separation and position resolution of the small prototypes. As shown in Chapter 3.4, the design goal of x-coordinate position resolution (300-500 μm) is obtainable with minimum losses by applying sufficient threshold cuts to the data. This has to be demonstrated for the new pad plane design in the following chapters.

4.1. Layout

The dimension of the pad plane is 80 mm $\times$ 377.5 mm with a modified pad geometry due to the increased pad plane height of 20 mm to 80 mm in order to provide a position reconstruction in y-direction. The technical design aim is a pad structure, which provides a two-dimensional position reconstruction within a single detector layer. This is reachable by subdividing the 36 rectangular pads into 2 $\times$ 36 triangular pads with independent read-out channels for two pads back-to-back on opposite sides of the pad plane (see Fig. 4.1).

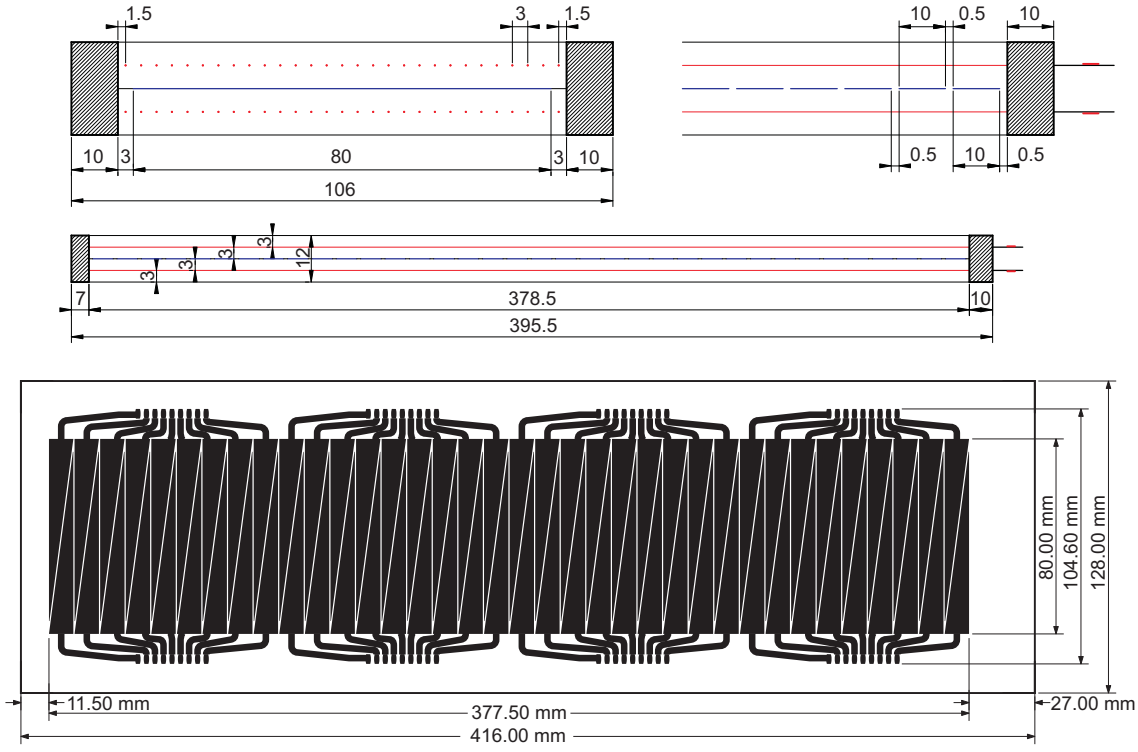

Fig. 4.1: Technical drawing of the real-size prototype [Sim09] and of the pad plane layout [Hei09].

Every triangle pad has a width of $W = 10$ mm in x-direction (twice the width of the pads in the small prototypes) and a height of $H = 80$ mm in y-direction. The doubled

pad width, the retained wire separation, and anode cathode gap lead to worsening in the charge sharing of adjacent pads. For this new pad size a larger anode-cathode gap is conceivable. The final pad size and geometry has to be chosen also in dependence of the possible number of readout channels. The detector is composed of two anode and two cathode frames, which consist of two 3 mm **P**oly**C**hlorinated **B**iphenyl (PCB) planes each. The two anode wire planes are placed at either side of the central pad plane (25 μm kapton) between two PCB planes. The contacts are realized by gluing the pad plane with silver epoxy through a small hole on the chamber frame. Different production states can by found in the appendix B.1.1.

4.2. Production

Two different pad plane coatings (Al and Cu) are compared to each other. Eight pad planes consist of 25 μm kapton foil, on both sides coated by vacuum evaporation with 1-3 μm copper like the small prototype pad plane. The vaporation of the kapton foils was performed using a Veeco VE-770-M[4] . In order to minimize the thermal exposure of the foils a rotatable castor was constructed (Blueprint can by found in Figure B.1). This castor shown in Figure 4.2 was also used as drying frame after cleaning the foils with non-methylated spirit and distilled water. An absolutely clean kapton surface is fundamental to avoid oxidation and to maximize the adhesion of the copper coating. The copper coating thickness and evaporation rate was monitored using an oscillating crystal and a referee foil installed next to the rotating castor above the melting crucible. To achieve a homogeneous non-oxidized copper coating, a constant evaporation rate of about 8.3 - 9.2 $\cdot 10^{-7}$ kg/(s m^2), a temperature of $\leq 2567\,^{\circ}$C within the melting crucible, and a pressure of $\leq 2 \cdot 10^{-4}$ Pa inside of the vacuum bell jar is required. After vaporating the first side of the kapton foil the bell jar is vented and the foil is flipped over.

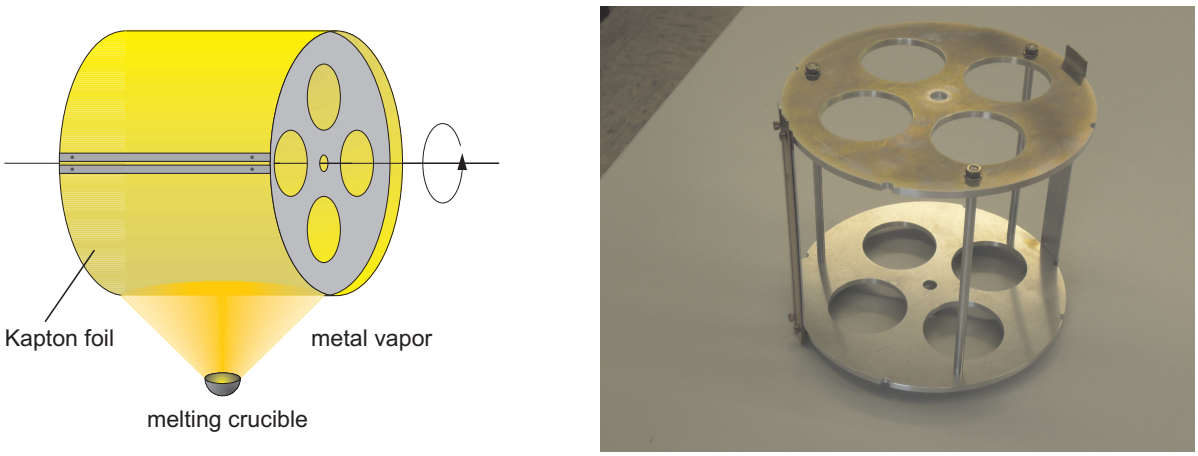

Fig. 4.2: Left: Functional principle sketch of evaporating a kapton foil using a castor frame.
Right: Photograph of a castor frame.

The efficiency of the copper coated pad plane prototype might be improved by a pad plane providing less absorption of TR between the two detector halves. The γ-transmission spectrum for Cu coated pad planes is dominated by the absorption in the

[4]High vacuum thin film evaporator model VE-770-M, Vecco Instruments Inc. Plainview, USA.

copper coating. In contrast to these pad planes, the Al pad plane transmission spectrum is defined by the absorption of kapton foil (see Fig. 4.3).

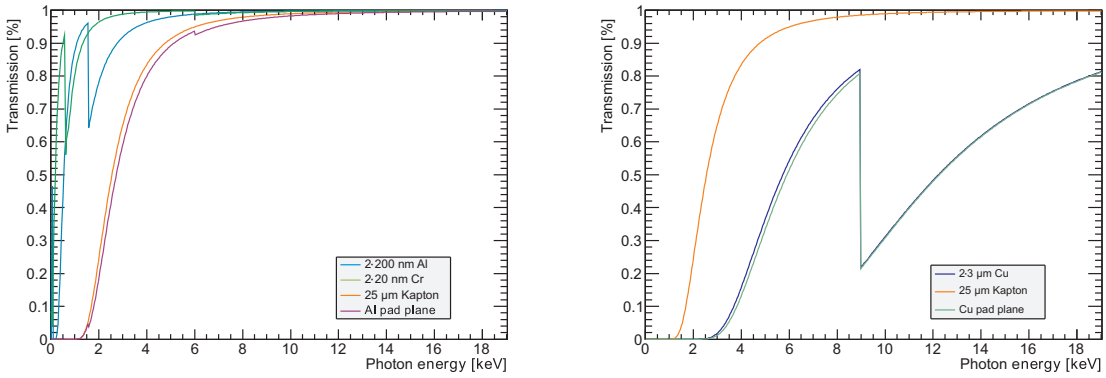

Fig. 4.3: Photon transmission calculated for Al coated pad plane (**left**) and Cu coated pad plane (**right**) [H+09].

Thus, a second batch of ten foils is coated initially with 20 nm chromium in order to obtain a strong adherence and afterwards with 200 nm aluminum on both sides. A disadvantage of the Al pad plane is its worse soldering property. Therefore, contacts to the read-out circuit are advantageous conveniently obtainable by gluing the pad plane with silver epoxy through a small hole on the electric contacts.

4.2.1. Metal Coating Thickness Measurement Using SEM

After vacuum copper evaporation the homogeneity of the coating surface and thickness needs to be controled. This was performed using a **S**canning **E**lectron **M**icrograph (SEM). In Figure 4.4 a picture taken with 2 kV and 20 kV electrons are shown.

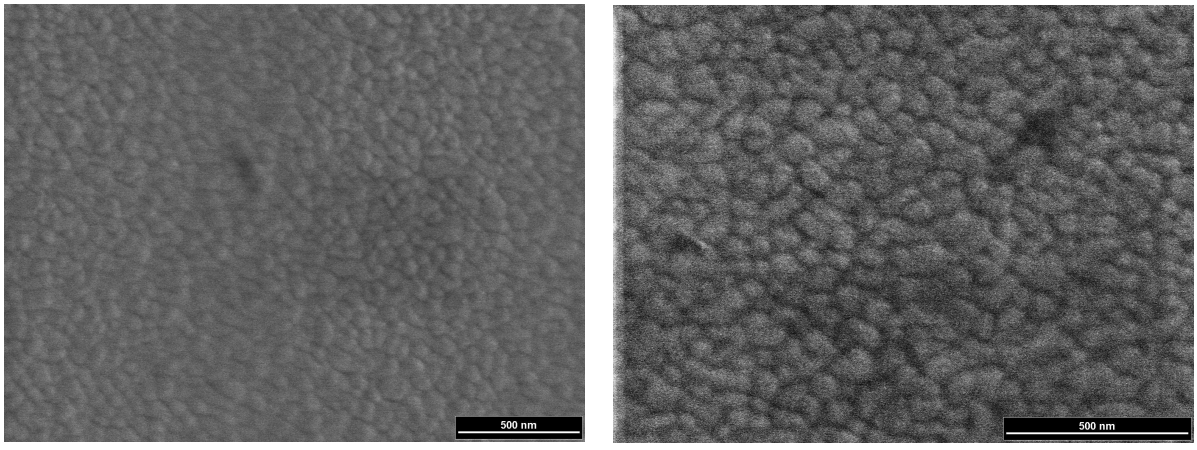

Fig. 4.4: Surface of a copper coated kapton foil measured by a SEM; **Left**: 2 kV; **Right**: 20 kV [Gru09].

The periodical structure is typical for copper evaporated surfaces. The amplitude of this structure cannot be determined due to the non-calibrated gray scale values. Thus, the homogeneity of the coating thickness is visualized in Figure 4.5, showing two cross sections measured with 20 kV electrons. This is only a small sample of the whole cross

section of the pad plane. Thus, a sufficient sample of cross section probes is required to evaluate the average thickness of the pad plane (see Fig. 4.6).

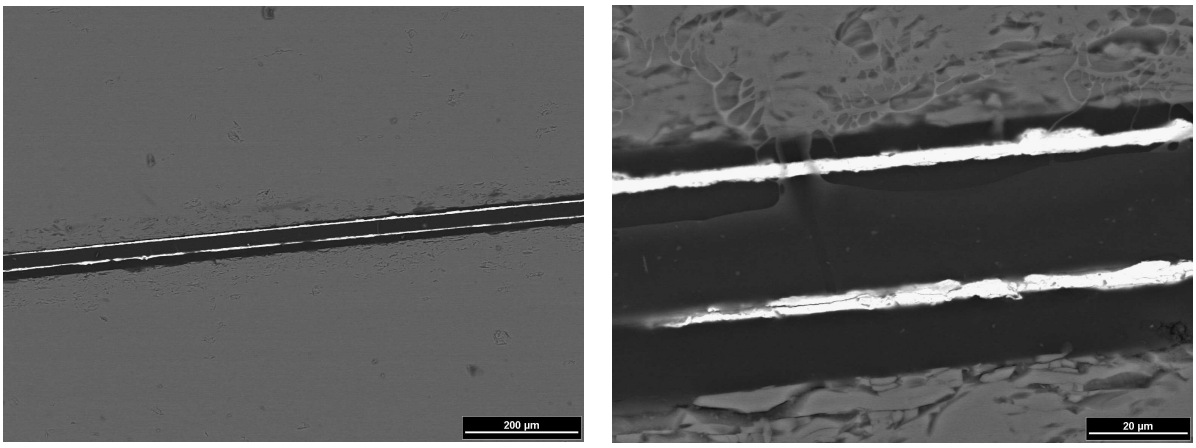

Fig. 4.5: Cross sections of one copper coated kapton foil measured by a SEM (20 kV) [Gru09].

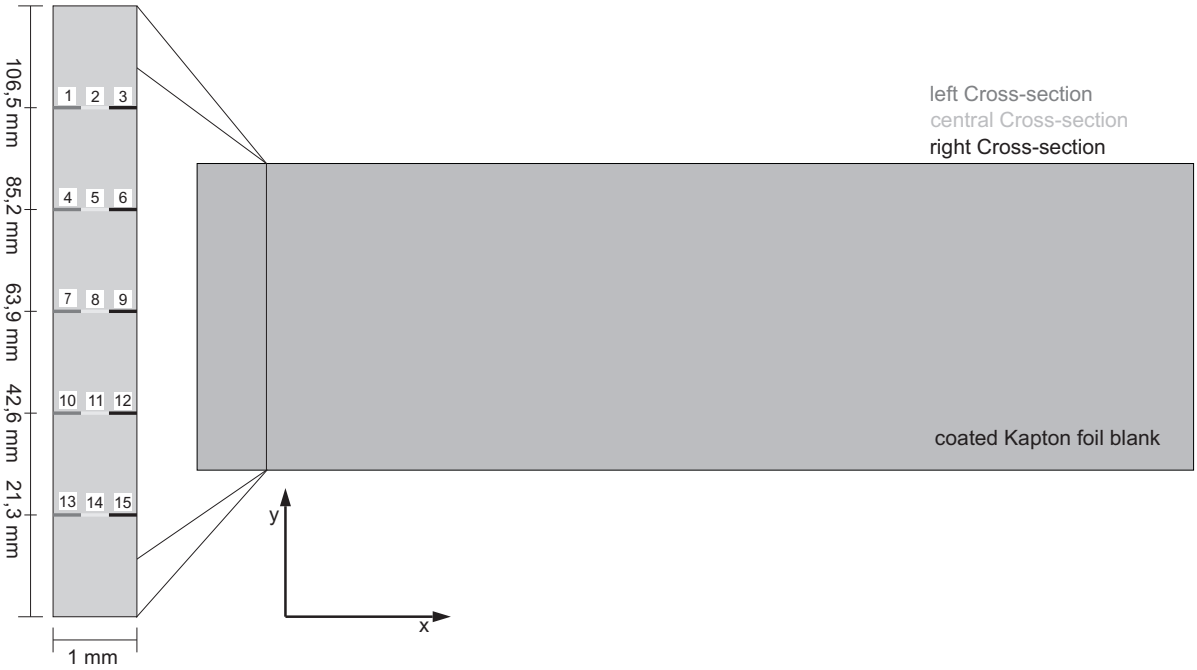

Fig. 4.6: Positions sketch of the SEM analyzed cross section samples. Five equally spaced cross section probes (vertical), taken from the complete height (128 mm) of one evaporated kapton foil, are trebly divided (horizontal).

Five equally spaced cross section probes of 1 mm width are taken from the vertical positions 21.3, 42.66, 63.9, 85.2, and 106.5 mm of one evaporated kapton foil. These probes are subdivided into three sections and scanned using a SEM. The pictures taken by the SEM (see Fig. 4.7) are scanned line by line to determine the coating thickness which is given by the number of pixels above a certain gray scale value. The line by line thickness measurements are supposed to be Gaussian distributed within one sample. The superposition of three adjacent SEM samples is shown in the right histogram in Figure 4.8. The accumulation points of this distribution are fitted to a Gaussian distribution

to evaluate the average and error of each point. The distribution of average coating thicknesses and errors was used to calculate the overall average coating thickness by error propagation. The results are shown in the left histogram of Figure 4.8.

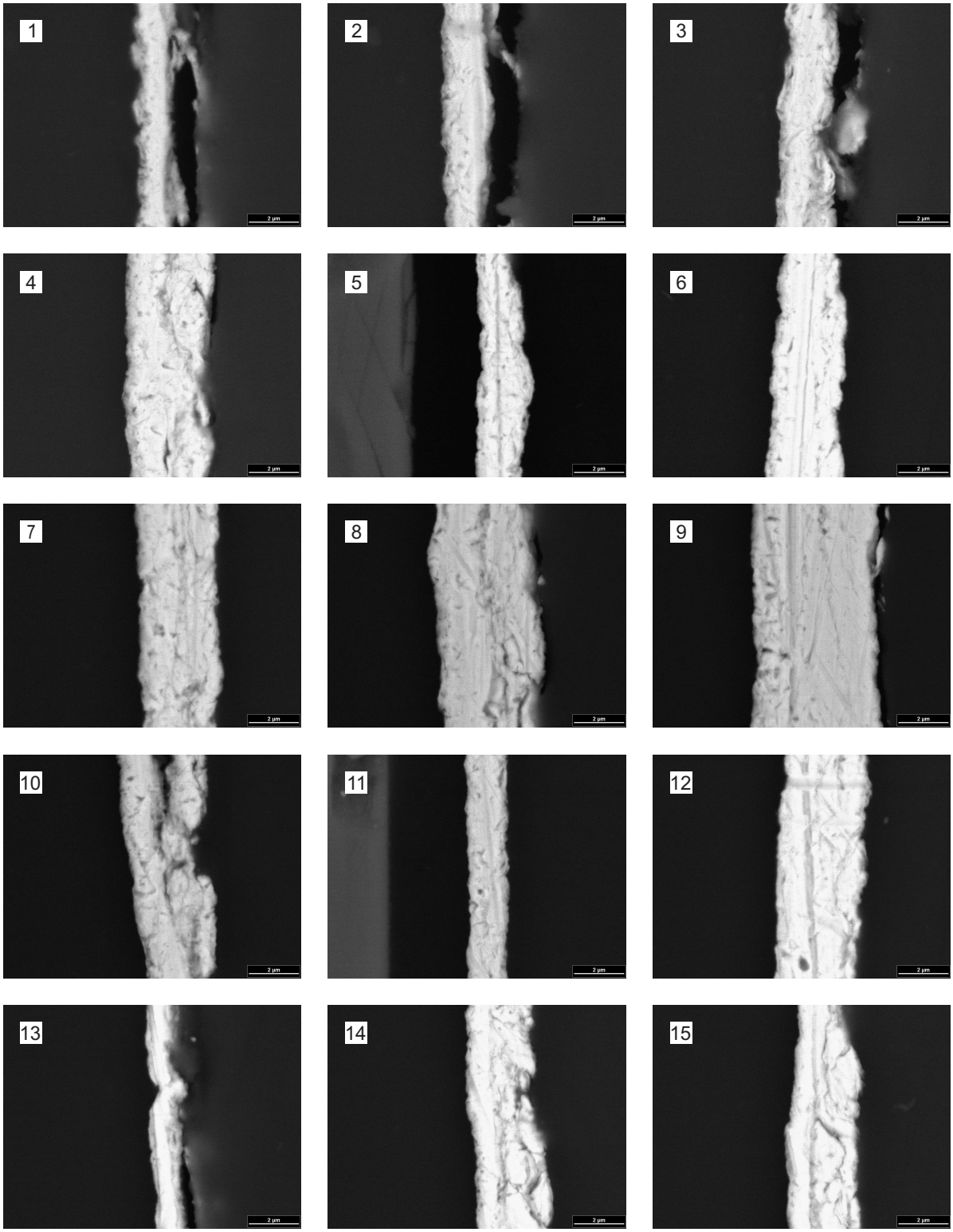

Fig. 4.7: 15 samples taken from five equally spaced cross section probes (vertical) trebly divided (horizontal) of one coated foil and analyzed by a SEM. Positions are shown in Figure 4.6 [Gru09].

The average coating thickness depending on the foil height is Gaussian distributed along the pad plane height due to the small dimensions of the melting crucible. The amplitude varies from 1.3 μm to 3.6 μm.

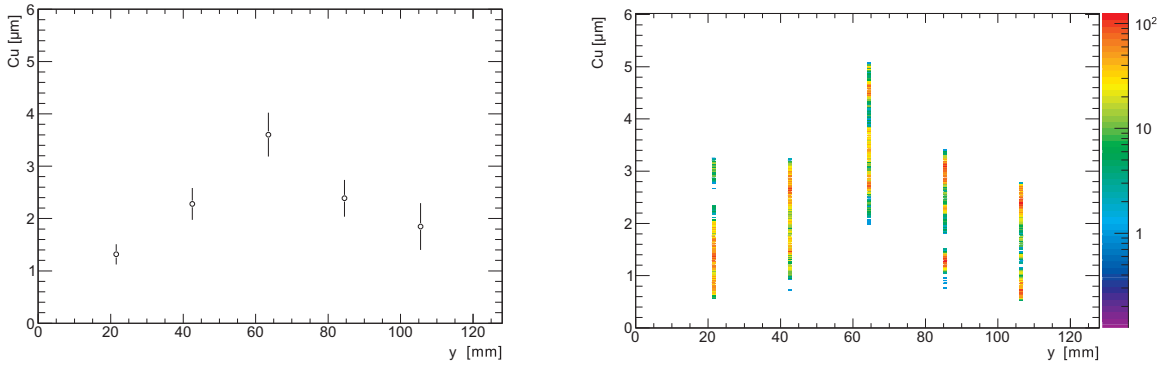

Fig. 4.8: Average coating thickness determined for three adjacent SEM samples (14.08.2008) (see Fig. 4.6 and 4.7). The thickness measurements are supossed to be Gaussian distributed within one sample. The superposition of three adjacent SEM samples are shown in the **right** histogram. The accumulation points of this distribution are fitted to a Gaussian distribution in order to evaluate the average and error of each point. The distribution of average coating thicknesses and errors can be used to calculate the overall average coating thickness for three adjacent SEM samples shown in the **left** histogram.

4.2.2. Pad Plane Structuring

The pad planes are structured by photolithography. The coated foil is initially heated to a temperature sufficient to remove any moisture that may be present on the surface. A viscous, liquid solution of photoresist is printed on both sides of the dried foil (see Fig. 4.9). The photoresist coated foil is then prebaked at 90 to 100 °C for 30 to 60 seconds in

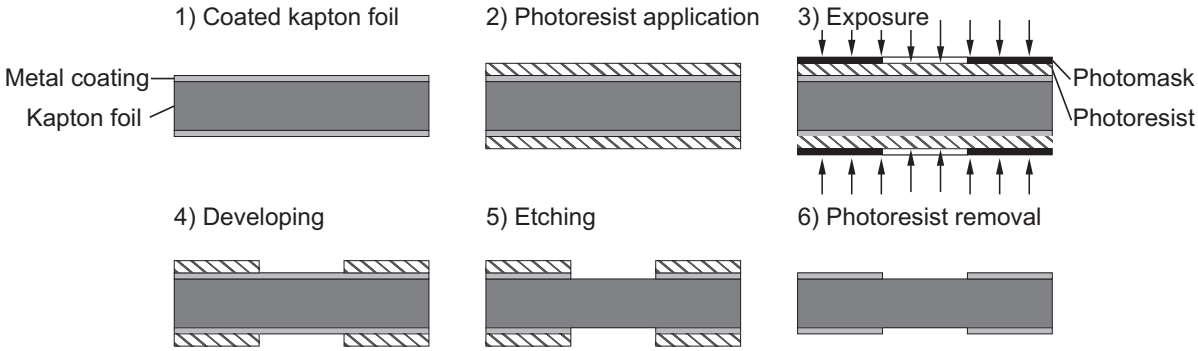

Fig. 4.9: Photolithography:
1) Cleaning and drying of the metal coated kapton foil
2) The photoresist printed on top of the metal coated kapton foil
3) The photoresist is exposed to a pattern of intense ultraviolet light through the photomask
4) Developing and removing of the exposed photoresist
5) Etching of the metal coating in the areas that are not protected by photoresist
6) Removing of the photoresist by a resist stripper.

order to dry the photoresist. After prebaking, the photoresist is exposed to a pattern of intense ultraviolet light through two photomasks (see Fig. 4.1). The position matching

of both masks is checked using crop marks on both masks (see. Fig. 4.10). The positive photoresist becomes soluble in the basic developer when exposed. This chemical change allows to remove non-exposed parts of the photoresist by a developer. In etching, a liquid chemical agent removes the metal in the areas that are not protected by photoresist. Copper is typically etched by ammonium chloride containing a copper chloride solution. The solving of copper increases the copper concentration and therefore the solution's density. In order to keep the copper ions in solution at pH-values of around 8.5, they are linked with ammonia in the copper tetramin complex. Aluminium is etched by a mixture of 1-5% HNO_3 to oxygenize aluminium, 65-75% H_3PO_4 to dissolve the Al_2O_3, 5-10% acetic acid to bedabble and buffer the nitric acid, and H_2O to adjust the etching rate at a given temperature. After the photoresist is no longer needed, it is removed from the foil by a liquid resist stripper.

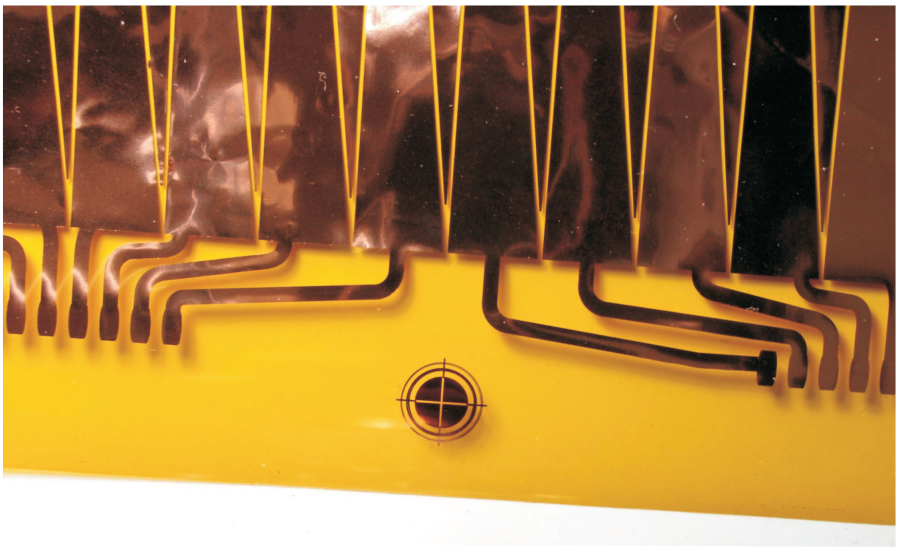

Fig. 4.10: Photographed crop mark of the copper coated pad plane.

Etching of small structures like peaked tops of triangulare pads is unconvertible. Therefore, the peaked tops are rounded on the photomask. The electric field is simulated by using Comsol 3.5[5] to determine the effect on the field homogeneity (see Fig. 4.11 and 4.12). The field intensity increases for rounded tops due to the increased metal cavity. This increase of field intensity is maintainable due to its localized character and it does not influence the overall field homogeneity.

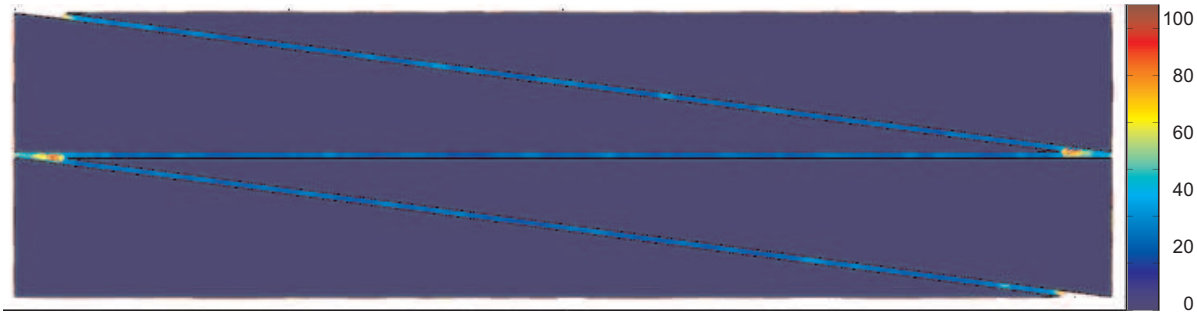

Fig. 4.11: Two-dimensional electric field simulation for peaked tops: Skala $[0 - 130\,\mathrm{V}]$.

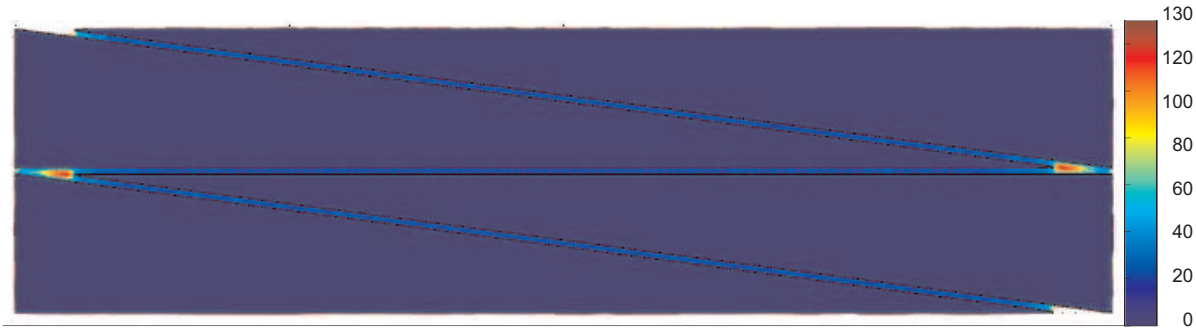

Fig. 4.12: Two-dimensional electric field simulation edgeless tops: Skala [0 – 130 V].

The produced pad plane foils made of copper (see Fig. 4.13) and aluminum (see Fig. 4.14) are shown in Figure 4.13 and 4.14. The homogeneity of the coating thickness and accuracy of the structure lay within the allowed tolerance.

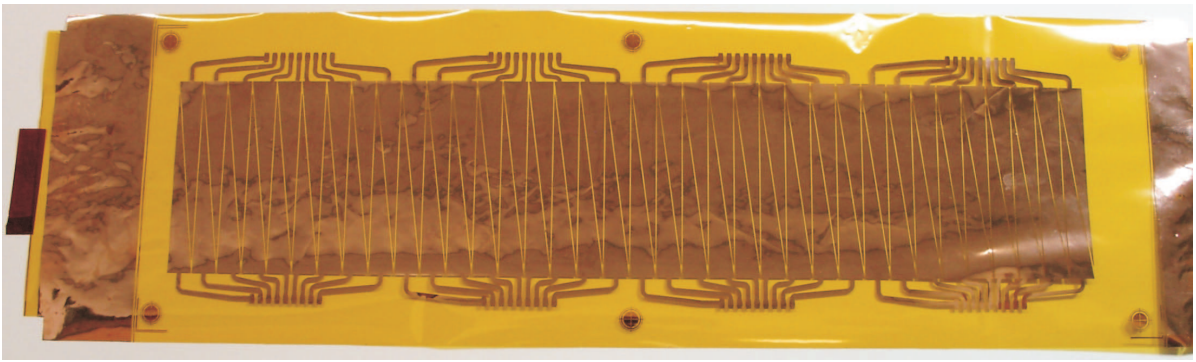

Fig. 4.13: Photographed copper coated pad plane after etching.

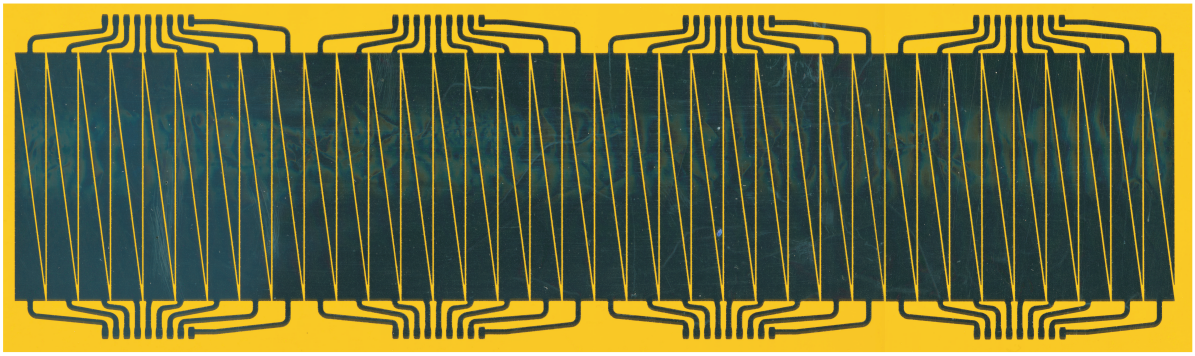

Fig. 4.14: Scaned aluminized pad plane after etching.

Another option to structure the coated pad plane is to use a laser **C**omputerized **N**umerical **C**ontrol (CNC) machine. In contrast to industrial applications of laser CNC machines, which are used to cut workpieces, they can be used to evaporate a defined layer of a sandwich structure. The accuracy of a structure produced by a laser CNC machine is given by the accuracy of the system itself and the focus diameter of the laser beam. The matching of the structures on both sides of the pad plane is optimal since

[5] COMSOL Multiphysics 3.5, COMSOL Multiphysics GmbH

the foil does not need to be turned during the structuring. The thermal stress of the kapton foil can be minimized by choosing a wavelength which is not absorbed by the foil. After structuring the coating on the first side, the laser beam is focused through the foil on the coating of the other side through the foil (see Fig. 4.15).

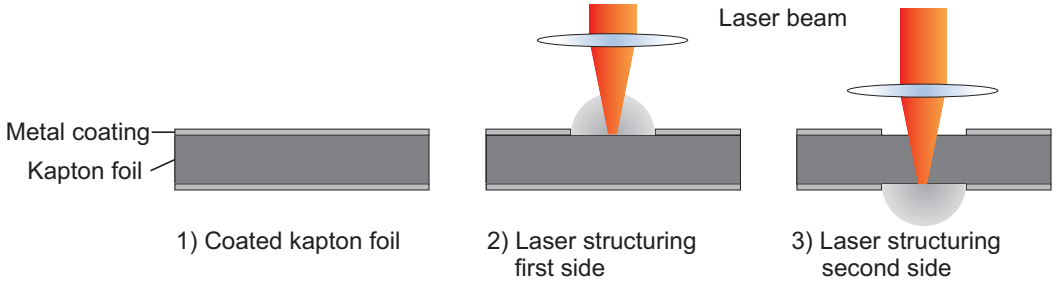

Fig. 4.15: Laser structuring:
1) Cleaning and drying of the metal coated kapton foil
2) Laser structuring of the first side of the metal coated kapton foil
3) Laser structuring of the second side of the metal coated kapton foil.

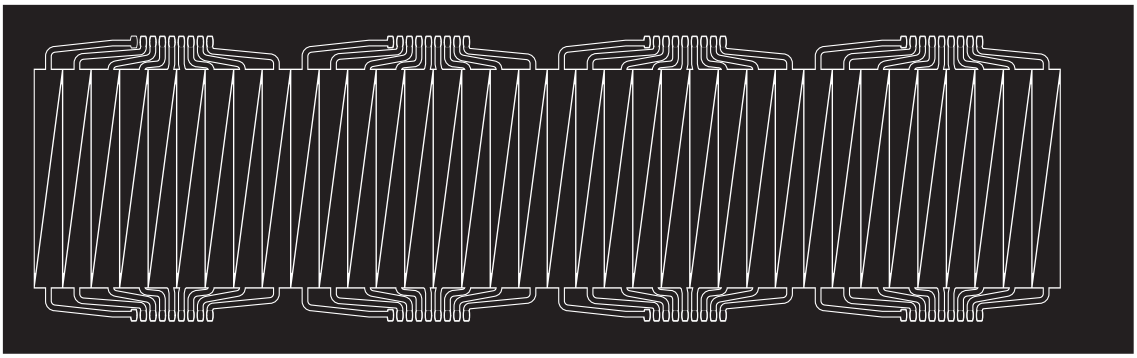

Fig. 4.16: Scetch of a pad plane after laser structuring.

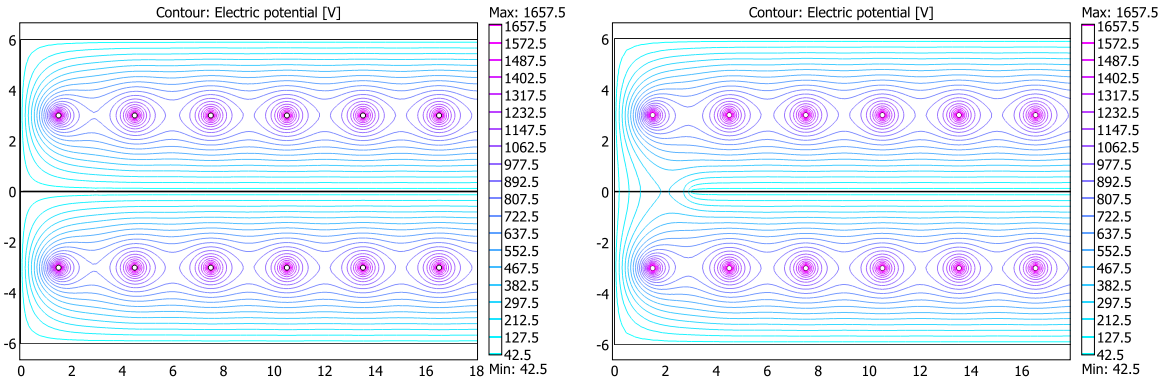

Fig. 4.17: Two-dimensional electric field simulation lateral cut: **Left**: Laser structured with metal border; **Right**: Structured by etching without metal border.

4.3. Position Resolution (x,y) Simulation

This simulation was programed in order to obtain a certain methode of position reconstruction. The design goal of the algorithm was a non-complex (reduced) simulation without autonomous event simulation procedure. Thus, an approach using the small prototype test beam data was choosen. This is warrantable as the chamber parameters, which characterize the average, signal are identical or akin for both prototypes since the average signal shape, given by the Mathieson formula, is more effected by the pad width W than by the Mathieson chamber parameter K_3 (see Chapter 2.4.1). Since the signal shape $Q(x)$ can be assumed to be Gaussian, it is specified by two parameters:

$$Q(x) = p'[0] \cdot \exp\left[-\frac{1}{2}\left(\frac{\mu_x - x}{p'[1]}\right)^2\right]. \tag{4.1}$$

These two parameters $p'[0]$ and $p'[1]$ are obtained event by event as described in Chapter 3.3.2. A spectrum of both fitted parameters of run 092 is shown in Figure 4.18. A strong correlation of both parameters can be identified with the cluster point of $p'[0] = 250$ and $p'[1] = 2.4$. The accumulation of fit values at $p'[1] = 1$ is due to a so-called one-pad cluster. Since a one-pad cluster induces charge only on one pad, fitting the cluster width is not possible due to the lacking charge sharing.

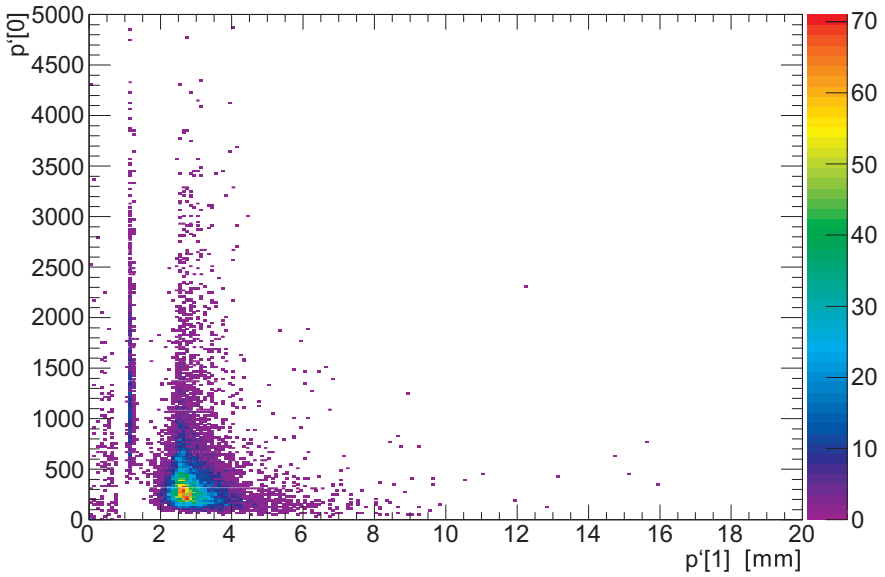

Fig. 4.18: Parameter correlation of $p'[0]$ and $p'[1]$.

The fitted parameters cannot be used as input data for event simulation. They have to be converted into two-dimensional Gaussian parameters which characterize charge density distribution $\rho(x, y)$. To simplify matters, the charge density distribution is assumed to be an axially symmetric Gaussian distribution.

$$\rho(x, y) = p[0] \cdot \exp\left[-\frac{1}{2}\left(\left(\frac{\mu_x - x}{p[1]}\right)^2 + \left(\frac{\mu_y - y}{p[1]}\right)^2\right)\right]. \tag{4.2}$$

Since this charge density distribution induces the charge distribution $Q(x)$, both parameter sets can be assumed to be correlated. For a choosen interval $p[0]$ from 0 to 4 and $p[1]$ from 0 to 10 the charge distribution is calculated (see Eq. 4.3). The pad plane is discretized in 2 points per millimeter and the lattice points are assigned to different pads. The charge induced on each pad is determined by summation of the charge density distribution on the corresponding pad.

$$\begin{aligned} Q_k &= \int_{x_{min}}^{x_{max}} \int_{y_{min}}^{y_{max}} \rho(x,y)\, dx\, dy && x_{min}, x_{max} \in Pad \;\; k \\ &\approx \sum_{x_{min}}^{x_{max}} \sum_{y_{min}}^{y_{max}} \rho(x,y) && y_{min}, y_{max} \in Pad \;\; k. \end{aligned} \tag{4.3}$$

The correlated parameter values of $p'[0]$ and $p'[1]$ are determined by fitting this charge distribution to a Gaussian distribution as described in Chapter 3.3.2. The relationship between the one-dimensional and two-dimensional parameters is given by a linear fit (see Fig. 4.19).

$$p'[0] = -10.83 \cdot p[0] + 393.1, \tag{4.4}$$

$$p'[1] = 0.9915 \cdot p[1] + 0.218, \tag{4.5}$$

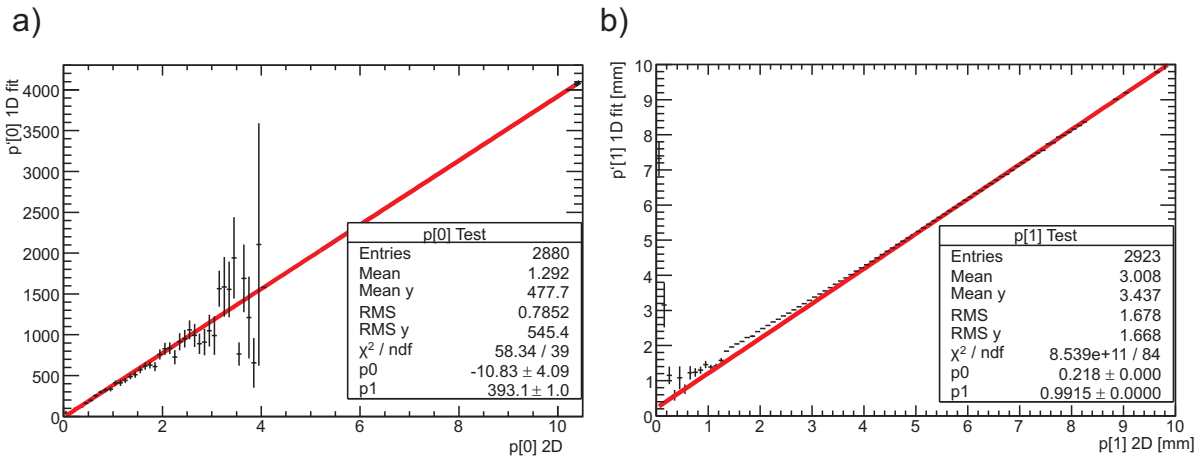

Fig. 4.19: Parameter correlation: both parameter spectra are linear fitted to obtain the relationship of the 2dim and 1dim parameter values
a) $p[0]$ plotted against $p'[0]$ and linear fitted $p'[0] = -10.83 \cdot p[0] + 393.1$
b) $p[1]$ plotted against $p'[1]$ and linear fitted $p'[1] = 0.9915 \cdot p[1] + 0.218$.

The input data generated by fitting the small prototype test beam data can be tested by calculating the PRF. The PRF determined for this data has to match the Mathieson-formula, if a realistic pad charge sharing and cluster width is used.

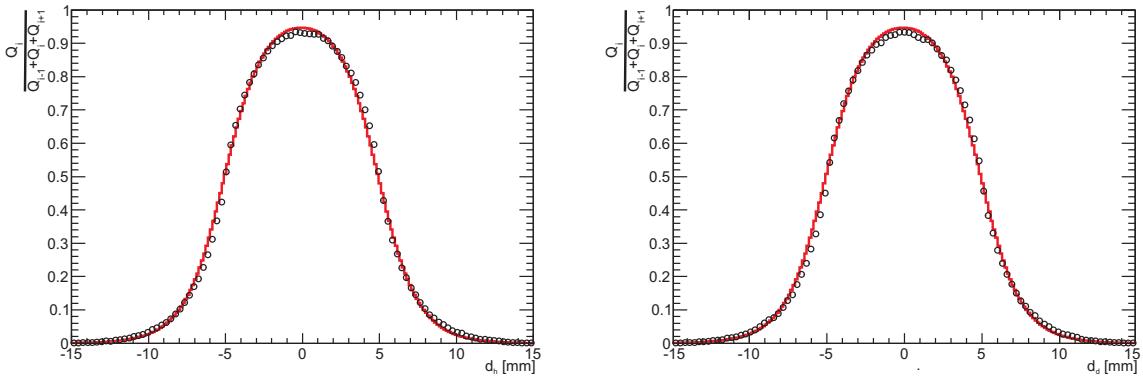

Fig. 4.20: Left: PRF calculated for vertical pad group; **Right**: PRF calculated for diagonal pad groups; **Red**: Mathieson-formula.

4.3.1. Track Position Reconstruction Using Charge Ratio of Adjacent Pads

A first approach to determine the cluster position in y-direction is using the charge sharing of adjacent triangular pads, whereas one pad has to be pad i with maximum charge Q_i. The correlation of the y-coordinate of the cluster position and charge ratio Q_i/Q_j is calculated for two adjacent triangular pads. Both pads are discretized into 20 lattice points in x-direction and 160 points in y-direction. The calculated correlation is very sensitive to the cluster width given by the parameter $p'[1]$ and is highly non-linear (see Fig. 4.21). Therefore, the correlation of cluster position and charge ratio has to be precalculated for every cluster width and position or has to be calculated for every event online. Furthermore, the y-coordinate reconstruction is impaired by the noise on the adjacent pad j due to decreasing charge sharing for cluster positions far from the separating line of both pads. Therefore, a different method to determine cluster positions is tested in order to avoid this calculation expenditure and sensitively to noise.

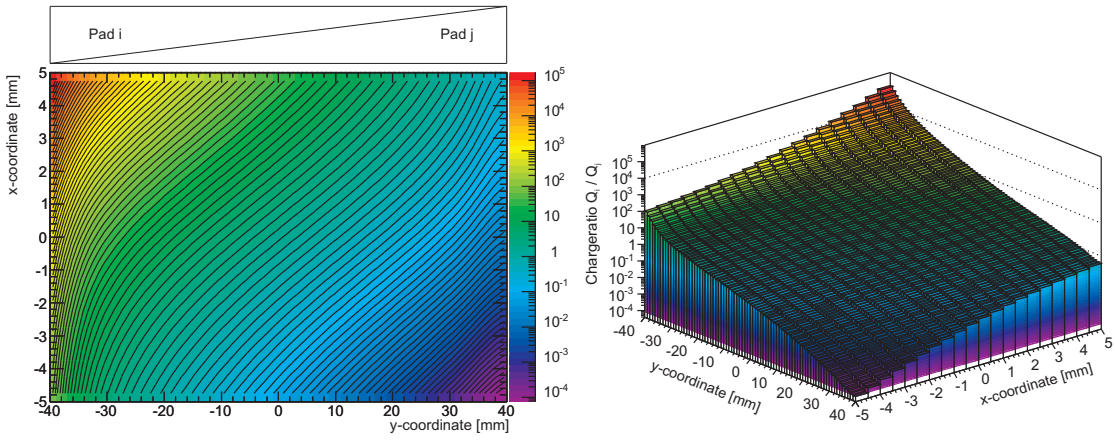

Fig. 4.21: Correlation of the cluster position and charge ratio Q_i/Q_j calculated for two adjacent triangulare pads, which are discretized into 2 lattice points per millimeter.

4.3.2. Track Position Reconstruction Using PRF

For the determination of the track position (x, y) the **P**ad **R**esponse **F**unction (PRF) measured by the charge sharing between adjacent pad groups might be used. The PRF is defined as the charge ratio of the pad group including the pad with maximum charge (Q_i) divided by the total charge on all three adjacent pad groups as function of the track position relative to the center of the pad group with maximum charge d_h and d_d. There are two different kinds of pad groups, vertical $(Q_j + Q_{j\pm9})$ and diagonal $(Q_j + Q_{j\pm8})$ pad groups (see Fig. 4.22).

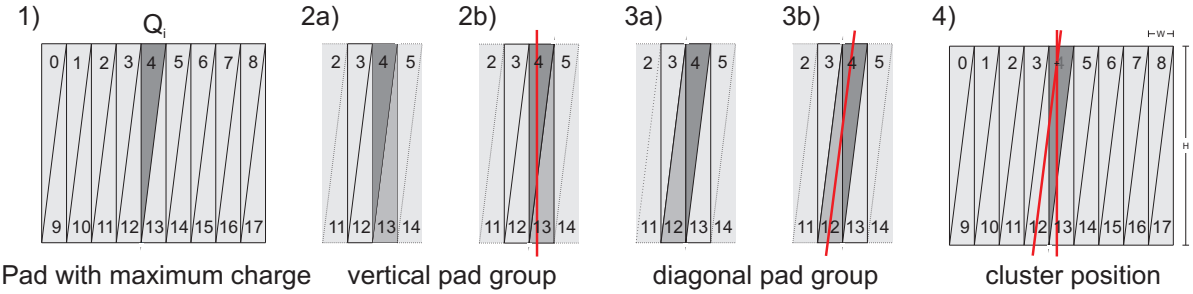

Fig. 4.22: Functional principle of the cluster position reconstruction:
1) Searching pad with maximum induced charge Q_i.
2a) Creating vertical pad groups.
2b) Calculate horizontal displacement d_h between cluster position and center of vertical pad group to get x-coordinate.
3a) Creating diagonal pad groups.
3b) Calculate diagonal displacement d_d between cluster position and center of diagonal pad group.
4) Intersection of both displacements is the reconstructed cluster position (x,y).

The horizontal displacement d_h between cluster position and center of vertical pad group with maximum charge is calculated to get the x-coordinate of the cluster position.

$$\begin{aligned} x &= \frac{W}{2} + (Wi + d_h) && i \in [0, 8], \\ x &= \frac{W}{2} + (W(i-9) + d_h) && i \in [9, 17]. \end{aligned} \tag{4.6}$$

Afterwards, the diagonal displacement d_d between cluster position and center of diagonal pad group with maximum charge is calculated. The intersection of both displacements is the reconstructed cluster position (x, y). The intersection can be interpreted as the same point in two Cartesian coordinate systems a and b. In this case, a is shifted by $\pm W/2$ and rotated $(\alpha = \arctan(W/H) \approx 7.13°)$ relative to b (see Fig. 4.23). The y-coordinate of b can be determined by solving the linear equations defined by the following matrix equation.

$$\begin{pmatrix} a_1 \\ a_2 \end{pmatrix} = \begin{pmatrix} \cos(\alpha) & -\sin(\alpha) \\ \sin(\alpha) & \cos(\alpha) \end{pmatrix} \cdot \left(\begin{pmatrix} b_1 \\ b_2 \end{pmatrix} + \begin{pmatrix} \pm W/2 \\ 0 \end{pmatrix} \right) \tag{4.7}$$

with

$$\begin{aligned} a_1 &= d_d & b_1 &= d_h \\ & & b_2 &= y \end{aligned} \tag{4.8}$$

$$y = \frac{(d_d - (d_h + W/2) \cdot \cos(\alpha))}{-\sin(\alpha)} \qquad i \in [0, 8],$$
$$y = \frac{(d_d - (d_h - W/2) \cdot \cos(\alpha))}{-\sin(\alpha)} \qquad i \in [9, 17]. \tag{4.9}$$

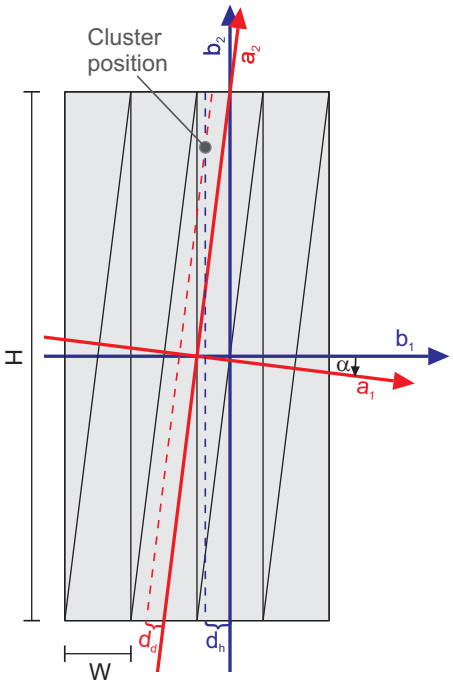

Fig. 4.23: Sketch of the coordinate systems a and b. The cluster position can be interpreted as the same point in both Cartesian coordinate systems. a is shifted by $\pm W/2$ and rotated relative to b.

18 triangular pads are simulated to determine the position resolution. The simulated events generated by fitting the small prototype test beam data are distributed within a Gaussian beam profile on top of the pad plane. The simulation algorithm does not include effects like charge accumulation around the anode wires (see Chapter 2.3.1 and 3.3.2). The position is obtained as described in Chapter 4.3.2. The relative error of the reconstructed position depending on the x- and y-coordinate can be determined by the deviation of the simulated track position (μ_x, μ_y) from the reconstructed track position (x, y) (see Eq. 4.2). The average relative errors depending on one coordinate show a strong correlation to the position (see Fig. 4.24). This can be interpreted as an effect of insufficient charge sharing of the pads. The correlation of the relative error disappears for halved pad width, which supports this interpretation. To obtain a realistic result for the position resolution the charge signal of every pad is 1024 Bit digitized and a two Bit Gaussian distributed noise of the last 10 Bits is added. The position resolution for each coordinate is given by the full width at half maximum of the distribution of the position deviation fitted to a Gaussian distribution (see Tab. 4.1).

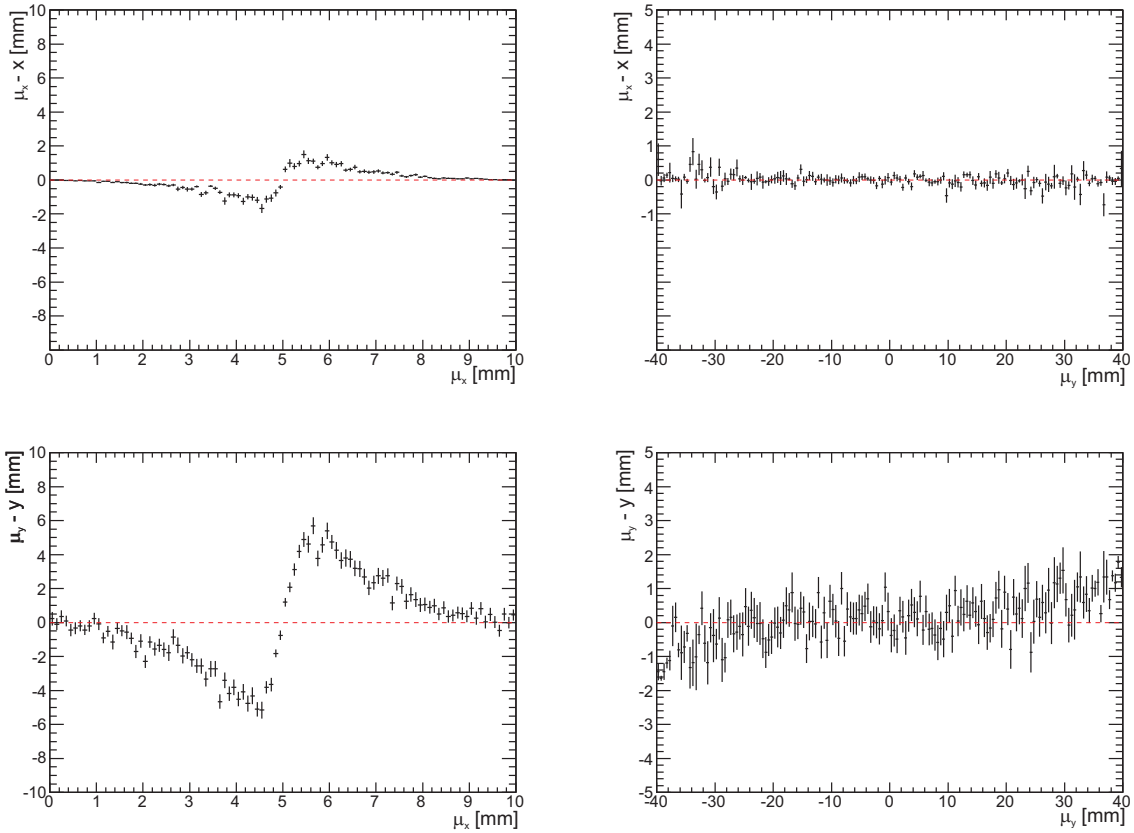

Fig. 4.24: Relative position errors for floating point accuracy and pad width $W = 10$ mm:
Left up: $(\mu_x - x)$ plotted versus μ_x; **Right up**: $(\mu_x - x)$ plotted versus μ_y;
Left down: $(\mu_y - y)$ plotted versus μ_x; **Right down**: $(\mu_y - y)$ plotted versus μ_y.

The position resolution for halved pad width is of the order of the position resolution for the small prototypes (see Fig. 3.24), which supports the simulation methode.

Tab. 4.1: Summary of position resolution simulations (see Chapter A.2).

	Pad width [mm]	PR x [mm]	PR y [mm]
Floating point accuracy	$W = 10$	0.4771	5.893
	$W = 5$	0.1180	3.087
Realistic noise level and 1024 Bit ADC digitalization	$W = 10$	1.0350	8.075
	$W = 5$	0.1223	3.085

4.4. Position Resolution (x,y) Measurement

The chamber was illuminated with a source of ^{55}Fe and one of ^{238}Pu. The ^{55}Fe source emits X-ray of 5.9 keV and the ^{238}Pu source emits X-ray of 13.6, 17.2, and 20.2 keV. The photons are absorbed by the detection gas mixture of 376.986 ml Ar(70%) CO_2(30%) (gas flow of 33.6 ml/min) with a contamination of 30 ppm O_2.

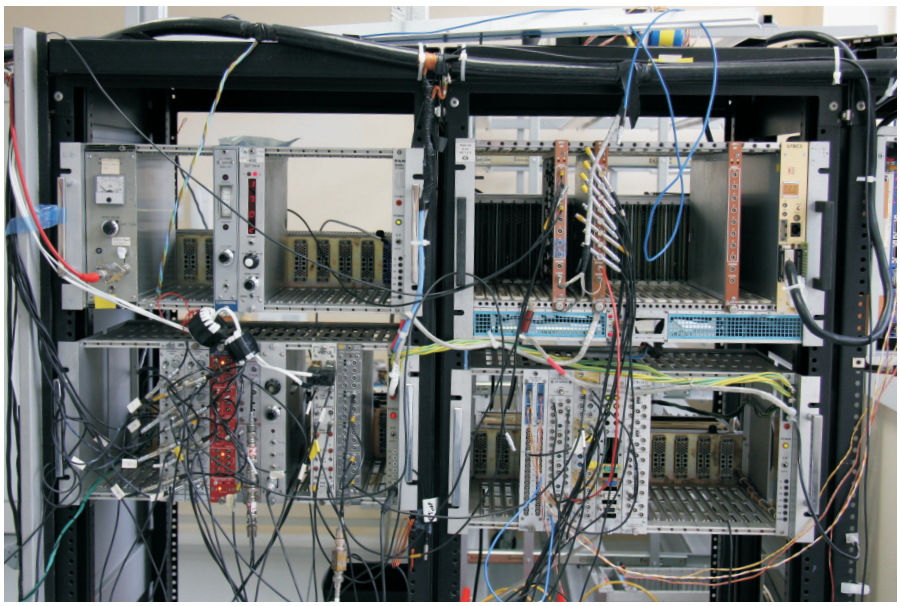

Fig. 4.25: Data Acquisition System used during the source measurements at the Hadron Physics Department National Institute for Physics and Nuclear Engineering Bucharest, Rumania, 2009.

The pad signals of eight pads, shown in Figure 4.31, are amplified with a charge-sensitive PASA, the same used for ALICE TRD prototype testing [A+01]. It has a gain of 2 mV/fC and a noise of about 1800 electrons r.m.s.. The **A**nalog-to-**D**igital **C**onverter (ADC) was a peak sensing, commercial: ORTEC AD811. The anode wire signal is amplified with a **C**harge **S**ensitive pre**a**mplifier (CSA) and a spectroscopy amplifier made by Andrei Caragheorgheopol. Both, CSA and main amplifier, were designed for high performance X- and γ-ray spectroscopy. The CSA has a gain of 2 mV/fC and a feedback capacitance of $C_f = 0.5\,\text{pF}$. The main amplifier provides a Gaussian pulse shape with a shaping time of $2\,\mu\text{s}$ and a maximum gain of 640. The used data aquisition system is shown in Figure 4.25.

4.4.1. Energy Spectra of the Used Sources

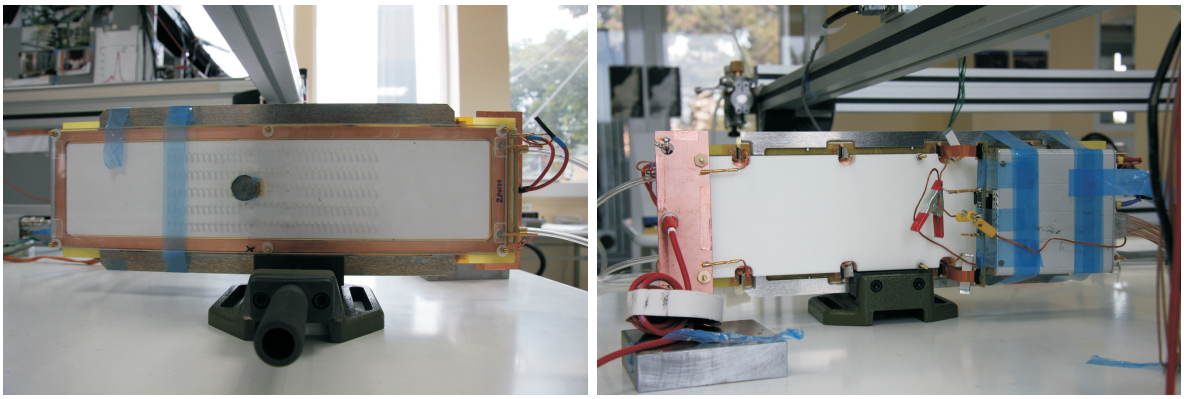

Fig. 4.26: Real-size prototype **Left**: Plexiglas collimator with applied ^{238}Pu source; **Right**: Rohacell layer.

The energy resolution for anode and cathode signal of the real-size prototype was measured using a ^{55}Fe and a collimated ^{238}Pu source (2 mm diameter). The signal was analyzed for the whole detector and also separately for both chamber halves due to the different gain and instability of the plexiglas collimator (left) chamber half (see Fig. 4.26). The measurements were performed at different anode voltage using an Ar(70%) CO_2(30%) gas mixture (Chapter 4.4).
The calibrated amplitude spectra for the prototype are presented in Figure 4.27 for signals taken by the cathode pad plane and in Figure 4.28 for signals taken by the anode wires. To obtain the total deposited charge, the charge sum over all eight pads and all wires was performed. The energy resolution of a detector is given by:

$$\text{Energy res.} = \frac{\text{FWHM}}{E} = \frac{2\sqrt{2\ln(2)}\cdot\sigma}{\mu} \approx 2.35\cdot\frac{\sigma}{\mu}. \tag{4.10}$$

where σ and μ are the parameters of a Gaussian fit to the 5.9 keV peak of the ^{55}Fe spectra and 20.2 keV peak of the ^{238}Pu spectra. The observed energy resolution of 28.83% corresponds to the anode signal, 26.3% to the pad signal for the ^{55}Fe source shown in Figure 4.27, respectively. For the ^{238}Pu source shown in Figure 4.28, an energy resolution of 12.43% was obtained by using the anode, 14.78% by using the pad signal, respectively.

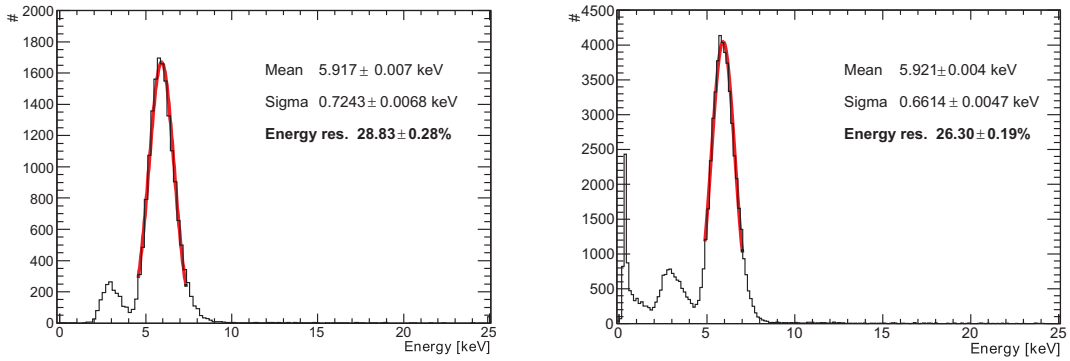

Fig. 4.27: ^{55}Fe source signal spectra, 1700 V anode voltage, right detector half.
Left: Anode wire signal; **Right**: Cathode pad signal.

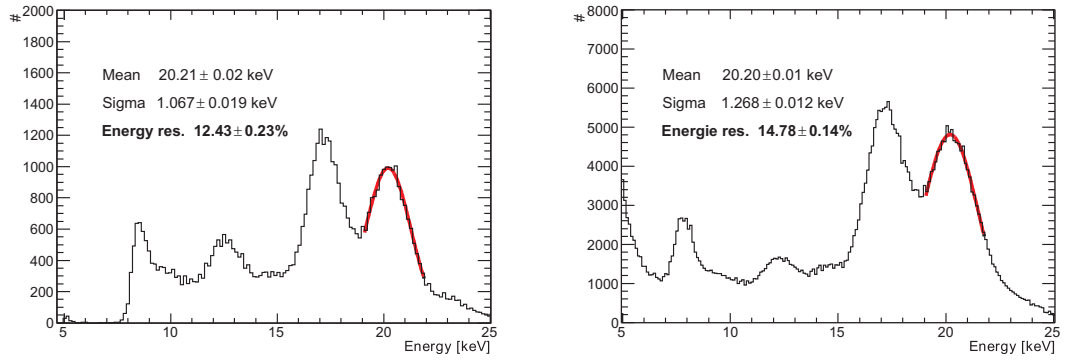

Fig. 4.28: ^{238}Pu source signal spectra, 1700 V anode Voltage, right detector half.
Left: Anode wire signal; **Right**: Cathode pad signal.

Beside the main peak corresponding to the full energy deposit, one or two escape peaks (EP_α, EP_β) corresponding to the partial energy deposit are visible in the spectra. The escape peak is due to the following process: A primary X-ray photon ionizes an electron from the K-shell of an argon atom and the hole is filled by electrons from higher shells. The energy difference ΔE is released either by a radiation-less transition (Auger effect), or in form of another X-ray photon. If this photon is not absorbed within the detector volume, the energy of this photon is lost. Instead, the energy difference $E_\gamma - \Delta E$ is deposited. The K_α line of argon has an energy of 2.96 keV and K_β of 3.19 keV. Thus, the expected escape peak positions are summarized in Tables 4.2 and 4.3.

Tab. 4.2: ^{55}Fe γ-spectra including first and second escape peak (EP_α and EP_β)

E_γ [keV]	Escape peak	Energy [keV]
5.9	EP_α	2.94
	EP_β	2.71

Tab. 4.3: ^{238}Pu γ-spectra including first and second escape peak (EP_α and EP_β)

E_γ [keV]	Escape peak	Energy [keV]
13.6	EP_α	10.64
	EP_β	10.41
17.2	EP_α	14.24
	EP_β	14.01
20.2	EP_α	17.24
	EP_β	17.01

The energy resolution of the real-size prototype depending on the anode voltage for 5.9 keV (left) and 20.2 keV (right) photon energy is shown in Figure 4.29. The average energy resolution is $26.5 \pm 4.9\%$ for the ^{55}Fe source and $21.7 \pm 5.5\%$ for the ^{238}Pu source.

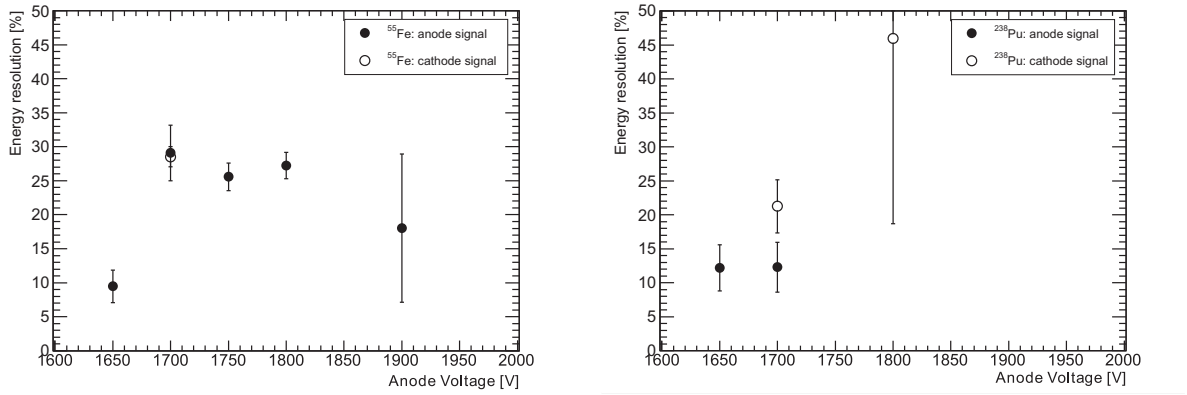

Fig. 4.29: Energy resolution for different anode voltages; **Left**: ^{55}Fe **Right**: ^{238}Pu.

4.4.2. Track Position Reconstruction

Eight pads are read out for this measurement. The signal is amplified with a charge sensitive PASA and digitized with a peak sensing ADC, as described in Chapter 4.3.2. To determine the track position the **P**ad **R**esponse **F**unction (PRF) measured by the charge sharing between adjacent pad groups is used. As shown in Figure 4.30, the calculated PRF for the measurement using the ^{238}Pu source meets the theoretical prediction by the Mathieson formula. In contrast to the PRF of the small prototype, the one-dimensional

projection of the real-size prototype PRF has an nonGaussian shape. This causes a smearing of the reconstructed collimator positions.

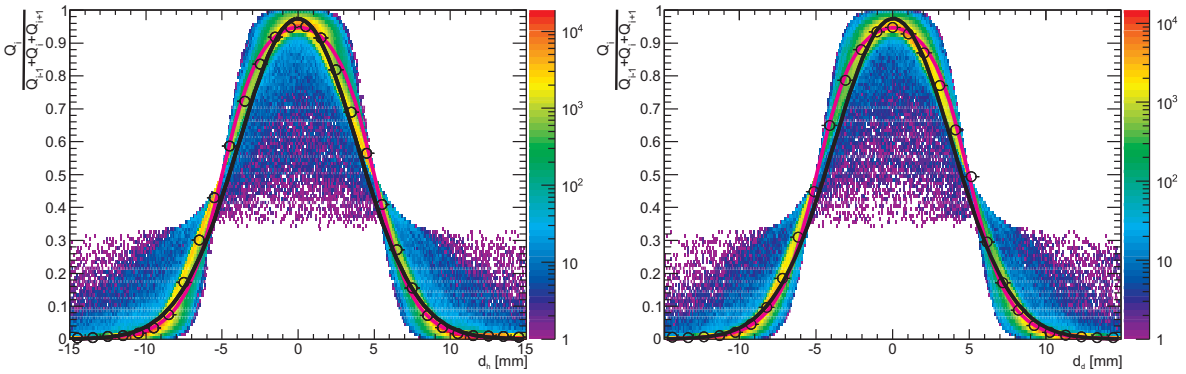

Fig. 4.30: ^{238}Pu new prototype: **Left**: Vertical pad group; **Right**: Diagonal pad group; ○: One-dimensional projection of the PRF; Black: Gaussian fit to the one-dimensional projection; Pink: Mathieson formula.

The PRF is defined as the charge ratio of the pad group including the pad with maximum charge (Q_i) divided by the total charge on all three adjacent pad groups as function of the track position relative to the center of the pad group with maximum charge d_h and d_d. Thus, six adjacent triangular pads are needed to determine a track position. Therefore, only events inducing maximum charge on pad two or five can be reconstructed (see Fig. 4.31).

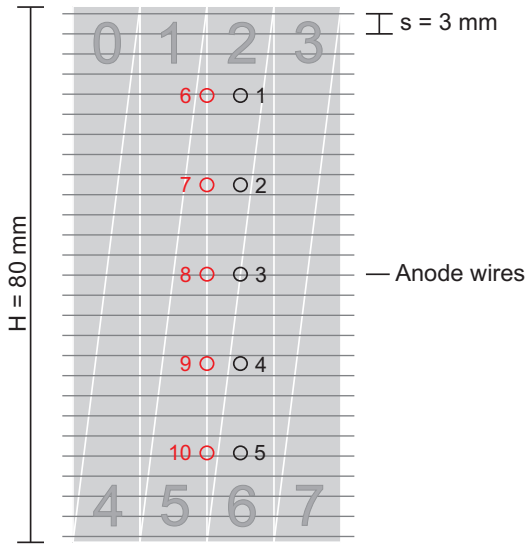

Fig. 4.31: Sketch of the eight used pads, collimator positions 1 - 10 and wire positions.

The collimator positions are equally arranged with a distance of 13.33 mm in y-direction and 5.0 mm in x-direction. Ten collimator positions were used for the following measurement (see Fig. 4.31). The anode wire positions vary relatively to the collimator positions. Thus, one does not expect all ten collimator positions to be exactly reconstructable since the reconstructed track position is equivalent to the anode wire position

within the shortest distance to the track of the incident photon. Due to the nonGaussian shape of the one-dimensional projection of the PRF seven different position reconstruction methods were tested and compared. The unweighted displacement (Eq. 2.39), the weighted displacement (Eq. 2.42), and four parameterized Mathieson-fit functions (Eq. 2.28, 2.29, 2.30 and 2.31), where x represents the reconstructed cluster position, A represents the modified amplitude coefficient, and K_3 represents the Mathieson chamber parameter. The diagonal shift within the spectrum of cluster positions reconstructed by using unweighted displacement is maybe due to the nonGaussian shape of the PRF (see Fig. A.9). This effect can be minimized by using the unweighted displacement shown in Figure A.10 or the parameterized Mathieson-fit functions shown in Figure A.11, A.12, A.13, and A.14. The use of Equation 2.28 and 2.30 gives the best results in inhibition of the diagonal shift of the reconstructed collimator positions. The remaining diagonal shape might be due to the position of the next anode wire which corresponds to an accumulation point of reconstructed cluster positions. There is no straight method of determining the position resolution of one single real-size prototype due to the indeterminableness of the absolute position of the initial photon. The position resolution is

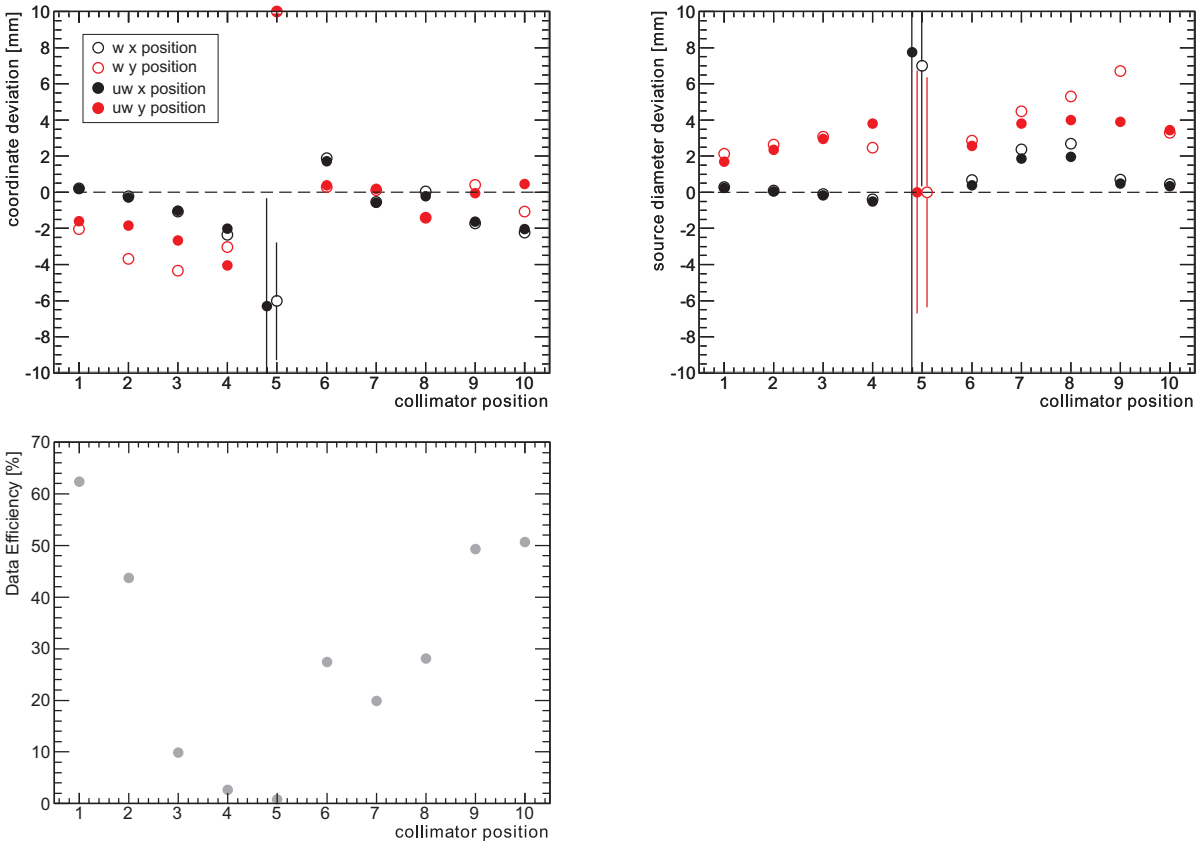

Fig. 4.32: Summary of Fig. A.9 and A.10. Spectra fitted to a Gaussian distribution to determine collimator position (**left**) and diameter (**right**). Data points beyond of y-axis' range are shifted to $y = 10$ and drawn without error bar and data points with an visible error bar are slightly shifted in x-direction for improved clarity.
●: unweighted x position ●: unweighted y position
○: weighted x position ○: weighted y position ●: data efficiency.

correlated with the deviation of the reconstructed coordinate from the collimator coordinate and the deviation of the measured collimator diameter from the reconstructed

diameter. There is no easy way to deconvolve this dependency. The collimator position and diameter values are obtained by fitting the cluster position distributions for each collimator position and coordinate to a Gaussian distribution. The diameter is given by the Gaussian fit parameter σ and the position is given by the Gaussian fit parameter μ. The results for cluster position reconstruction by using the weighted and unweighted displacement are shown in Figure 4.32. The increasing deviation for collimator position 3, 4, and 5 is due to the small number of pads used for this measurement. Therefore, data efficiency (ratio of reconstructed events to all measured events) decreases and only events inducing maximum charge on pad two or five can be reconstructed. The reconstructed x-coordinates and collimator diameter show a good agreement with the theoretical values for all reconstruction methods (see Fig. 4.32 and 4.33). The reconstructed y-coordinates and collimator diameter deviate from the theoretical values because of the diagonal shift generated by the nonGaussian shape of the PRF and the accumulation of reconstructed clusters next to the wire positions due to the electric field characteristic perpendicular to the wire direction.

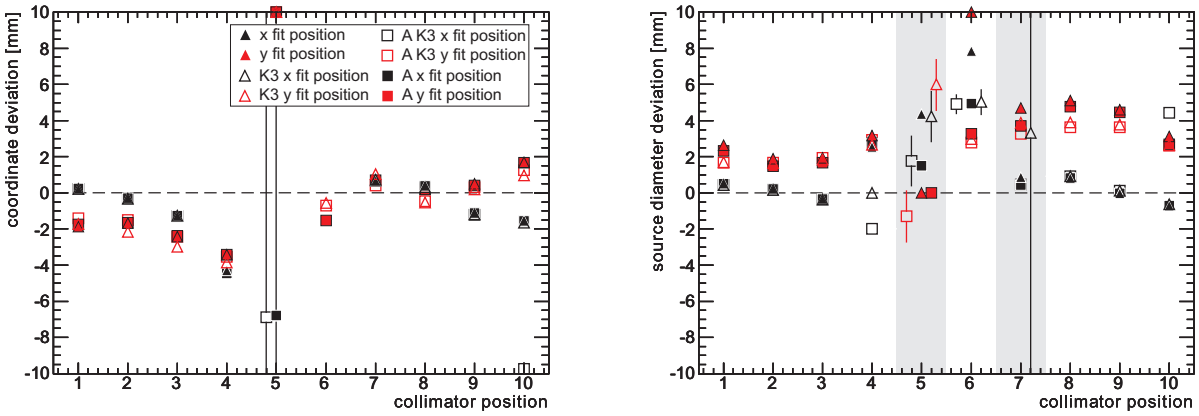

Fig. 4.33: Summary of Fig. A.11 to A.14. Spectra fitted to a Gaussian distribution to determine collimator position (**left**) and diameter (**right**). Data points outside of y-axis' range are shifted to $y = 10$ and drawn without error bar and data points with an visible error bar are slightly shifted in x-direction for improved clarity.

▲: x-coordinate by fitting to Eq. 2.31 ▲: y-coordinate by fitting to Eq. 2.31
△: x-coordinate by fitting to Eq. 2.30 △: y-coordinate by fitting to Eq. 2.30
□: x-coordinate by fitting to Eq. 2.28 □: y-coordinate by fitting to Eq. 2.28
■: x-coordinate by fitting to Eq. 2.29 ■: y-coordinate by fitting to Eq. 2.29.

5. Conclusion/Summary

The CBM experiment at FAIR at the GSI is a dedicated heavy-ion experiment. It is designed to perform research of strongly interacting matter in ultrarelativistic heavy ion-collisions and to explore the QCD phase diagram of nuclear matter. CBM consists of several detectors, one of them being the **T**ransition **R**adiation **D**etector (TRD) providing particle tracking and electron identification. In this diploma thesis, the position resolution and electron-pion-separation performance of two TRD prototypes has been examined using a test beam at GSI (small prototype) and ^{238}Pu and ^{55}Fe source measurements at the Hadron Physics Department National Institute for Physics and Nuclear Engineering Bucharest, Rumania, (real-size prototype).

The small prototype provided also the basis of the PHD thesis of Melanie Klein-Bösing [KB09] where detailed performance studies and simulations can be found. It was shown that the the x-coordinate position resolution of the small prototype meets the experimental requirements for CBM. The y-coordinate of the cluster can be determined by one detector within certain limits. The y-coordinate cannot be determined more precisely than the wire coordinate, due to the physical process of the signal generation of ('within') a multiwire proportional counter. Furthermore, the y-coordinate can only be determined within the central area of the detector. Clusters located between -5 and 5 mm from the pad row separation can be reconstructed. The position resolution and electron-pion-separation performance can be optimized by applying threshold cuts to the data. The threshold values have to be considered since their influence on the position resolution and on the electron-pion-separation is correlated. By using reasonable cut values a particle rate depending position resolution of 0.179 ± 0.002 mm could be obtained by using a gas mixture of Xe(85%) CO_2(20%), an anode voltage of 1800 V, and $p = 2$ GeV/c particles. For this conditions, the PR was almost steady for different particle rates up to rates of 51.0 kHz/cm^2 without applying static or dynamic cluster quality cut. A pion efficiency of approximated 0.7%, which is equivalent to a pion suppression factor of approximated 140, can be reached by using this cut values for 10 detector layers in a row. The pion efficiency of 1%, at an electron efficiency of 90%, like it is envisaged for the CBM-TRD, was achieved for eight layers of the prototypes by using the *dynamic CQC* cut.

The energy resolution of the real-size prototype is 26.5 ± 4.9% for the ^{55}Fe source and 21.7 ± 5.5% for the ^{238}Pu source. The position resolution simulation suggests a position depending error. The average relative errors depending on one coordinate show a strong correlation to the position. This can be interpreted as an effect of insufficient charge sharing of the pads. The correlation of the relative error disappears for halved pad width, which supports this interpretation. The position resolution of the real-size prototype cannot be determined by a source measurement of one single real-size prototype due to the indeterminableness of the absolute position of the initial photon. The position resolution is correlated with the deviation of the reconstructed coordinate from the collimator coordinate and the deviation of the measured collimator diameter from the reconstructed diameter. There is no easy way to deconvolve this dependency. The position resolution will be measured at a cosmics or test beam run using a silicon tracking detector, scheduled for 2009 - 2010. The results of the simulation of the real-size prototype has to be compared with this test beam measurement results.

The position resolution in y-direction of the real-size prototype has to be determined,

whereas the result of the small prototype meets the design goal of the CBM TRD, but is given by the wire distance divided by $\sqrt{12}$. The position resolution in y-direction of the real-size prototype will as well be defined by the anode wire distance. Thus, other pad and chamber geometry options have to be checked. For example, a pair of quadratic chambers, one rotated by 90°, lined up alternatingly, provides the same position resolution for both directions with minimum losses of active detector area and performance due to particle energy loss within detector frame components. A next generation prototype has to track all charged particles with a position resolution of 300-500 μm in x- and y-direction within one or two detector layers. This limits the pad width and anode-cathode gap. The exposition of the TRD to counting rates up to 100 kHz/cm^2 delimitates the pad height and also the anode- cathode gap. Due to the good position resolution performance of the small prototype for counting rates up to 63.5 kHz/cm^2 suggests retain basic chamber parameters like pad width and anode-cathode gap. The smaller absorption of TR between the two detector halves by the Al coated pad plane of the real-size prototype would also be a good feature for a new prototype.

The results confirm the further development of a next generation prototype for a TRD for the CBM experiment based on the conclusions of the measurements performed with the small and real-size prototypes.

A. Measurments and Histograms

A.1. Small Prototype

A.1.1. Determination of Particle Rate

Gray-colored runs are used for histograms shown within this thesis.

Tab. A.1: Run summary of the small prototype test beam 2006 @ GSI including particle rate

run	U[V]	p [GeV/c]		Spill [s]	$\langle Si_{1,2} \rangle$ Beam Area [cm^2]	Events Si_1, Si_2, Pb	Rate R_2 [kHz]	Rate R_1 [kHz/cm^2]
40	1700	1.5	-	10	2.86	105	$1.05{\cdot}10^{-2}$	$1.83{\cdot}10^{-3}$
41	1700	1.5	-	10	2.84	108	$1.08{\cdot}10^{-2}$	$1.90{\cdot}10^{-3}$
42	1700	1.5	-	4(?)	2.86	98	$2.45{\cdot}10^{-2}$	$4.28{\cdot}10^{-3}$
43	1700	1.5	-	4	2.87	101	$2.53{\cdot}10^{-2}$	$4.40{\cdot}10^{-3}$
48	1800	1.5	-	4	2.93	209	$5.23{\cdot}10^{-2}$	$8.90{\cdot}10^{-3}$
50	1800	1.0	-	4	3.57	460	$1.15{\cdot}10^{-2}$	$1.61{\cdot}10^{-2}$
51	1800	1.0	-	4	3.37	160	$4.00{\cdot}10^{-2}$	$5.94{\cdot}10^{-3}$
52	1800	1.0	+	2	2.73	200	$1.00{\cdot}10^{-1}$	$1.83{\cdot}10^{-2}$
53	1800	1.0	+	2	2.61	170	$8.50{\cdot}10^{-2}$	$1.63{\cdot}10^{-2}$
58	1800	1.5	+	10	2.79	100	$1.00{\cdot}10^{-2}$	$1.79{\cdot}10^{-3}$
60	1800	1.5	+	10	2.77	100	$1.00{\cdot}10^{-2}$	$1.80{\cdot}10^{-3}$
61	1800	1.5	+	1	3.19	1200	$1.20{\cdot}10^{+0}$	$1.88{\cdot}10^{-1}$
62	1800	1.5	+	1	3.17	2700	$2.70{\cdot}10^{+0}$	$4.25{\cdot}10^{-1}$
63	1800	1.5	+	1	3.08	1160	$1.16{\cdot}10^{+0}$	$1.88{\cdot}10^{-1}$

continued on next page

continued from previous page							
run	U[V]	p [GeV/c]	Spill [s]	$\langle Si_{1,2} \rangle$ Beam Area [cm^2]	Events Si_1, Si_2, Pb	Rate R_2 [kHz]	Rate R_1 [kHz/cm^2]
64	1800	1.5 +	1		7600	$7.60 \cdot 10^{+0}$	$1.30 \cdot 10^{+0}$
65	1800	1.5 +	2		2150	$1.08 \cdot 10^{+0}$	$1.84 \cdot 10^{-1}$
66	1800	1.5 +	5	3.07	953	$1.91 \cdot 10^{-1}$	$3.11 \cdot 10^{-2}$
67	1800	1.5 +	0.7		5300	$7.57 \cdot 10^{+0}$	$1.30 \cdot 10^{+0}$
68	1800	1.5 +	0.5		7138	$1.43 \cdot 10^{+1}$	$2.45 \cdot 10^{+0}$
70	1800	1.5 +	0.5		7000	$1.40 \cdot 10^{+1}$	$2.40 \cdot 10^{+0}$
71	1800	1.5 +	4		55	$1.38 \cdot 10^{-2}$	$2.36 \cdot 10^{-3}$
74	1800	2.0 +	10	2.33	319000	$3.19 \cdot 10^{+1}$	$6.23 \cdot 10^{+0}$
75	1800	2.0 +	5	2.50	491000	$9.82 \cdot 10^{+1}$	$1.83 \cdot 10^{+1}$
76	1800	2.0 +	5	2.54	166000	$3.32 \cdot 10^{+1}$	$6.53 \cdot 10^{+0}$
77	1800	2.0 +	5	2.76	485000	$9.70 \cdot 10^{+1}$	$1.76 \cdot 10^{+1}$
78	1800	2.0 +	2	2.87	586000	$2.93 \cdot 10^{+2}$	$5.10 \cdot 10^{+1}$
79	1800	2.0 +	2	2.89	567000	$2.84 \cdot 10^{+2}$	$4.90 \cdot 10^{+1}$
80	1600	2.0 +	2	2.92	594000	$2.97 \cdot 10^{+2}$	$5.09 \cdot 10^{+1}$
81	1600	2.0 +	2	2.89	606000	$3.03 \cdot 10^{+2}$	$5.25 \cdot 10^{+1}$
82	1600	2.0 +	5	2.75	698000	$1.40 \cdot 10^{+2}$	$2.54 \cdot 10^{+1}$
83	1600	2.0 +	5	2.81	682000	$1.36 \cdot 10^{+2}$	$2.42 \cdot 10^{+1}$
84	1600	2.0 +	10		764000	$7.64 \cdot 10^{+1}$	$1.31 \cdot 10^{+1}$
85	1600	2.0 +	10		677000	$6.77 \cdot 10^{+1}$	$1.16 \cdot 10^{+1}$
86	1600	2.0 +	2		631000	$3.16 \cdot 10^{+2}$	$5.41 \cdot 10^{+1}$
87	1700	2.0 +	2		563000	$2.82 \cdot 10^{+2}$	$4.83 \cdot 10^{+1}$
88	1700	2.0 +	2		668000	$3.34 \cdot 10^{+2}$	$5.72 \cdot 10^{+1}$
89	1700	2.0 +	2		676000	$3.38 \cdot 10^{+2}$	$5.79 \cdot 10^{+1}$
90	1700	2.0 +	5		705000	$1.41 \cdot 10^{+2}$	$2.42 \cdot 10^{+1}$
91	1700	2.0 +	5		714000	$1.43 \cdot 10^{+2}$	$2.45 \cdot 10^{+1}$
92	1700	2.0 +	10		737000	$7.37 \cdot 10^{+1}$	$1.26 \cdot 10^{+1}$
93	1700	2.0 +	10		717000	$7.17 \cdot 10^{+1}$	$1.23 \cdot 10^{+1}$
95	1550	2.0 +	10		720000	$7.20 \cdot 10^{+1}$	$1.23 \cdot 10^{+1}$
96	1550	2.0 +	10		694000	$6.94 \cdot 10^{+1}$	$1.19 \cdot 10^{+1}$
97	1550	2.0 +	5		709000	$1.42 \cdot 10^{+2}$	$2.43 \cdot 10^{+1}$
98	1550	2.0 +	5		707000	$1.41 \cdot 10^{+2}$	$2.42 \cdot 10^{+1}$
99	1550	2.0 +	2		640000	$3.20 \cdot 10^{+2}$	$5.49 \cdot 10^{+1}$
110	1650	2.0 +	5		330000	$6.60 \cdot 10^{+1}$	$1.13 \cdot 10^{+1}$
111	1650	2.0 +	2		530000	$2.65 \cdot 10^{+2}$	$4.54 \cdot 10^{+1}$
113	1850	2.0 +	2		740000	$3.70 \cdot 10^{+2}$	$6.34 \cdot 10^{+1}$
114	1850	2.0 +	2		134000	$6.70 \cdot 10^{+1}$	$1.15 \cdot 10^{+1}$
117	1850	2.0 +	5		817000	$1.63 \cdot 10^{+2}$	$2.80 \cdot 10^{+1}$
120	1850	2.0 +	10		862000	$8.62 \cdot 10^{+1}$	$1.48 \cdot 10^{+1}$
122	1800	2.0 +	10		868000	$8.68 \cdot 10^{+1}$	$1.49 \cdot 10^{+1}$
124	1800	2.0 +	2		769000	$3.85 \cdot 10^{+2}$	$6.59 \cdot 10^{+1}$

A.2. Real-Size Prototype

A.2.1. Position Resolution (x,y) Simulation, Relativ Position Error for Floating Point Accuracy

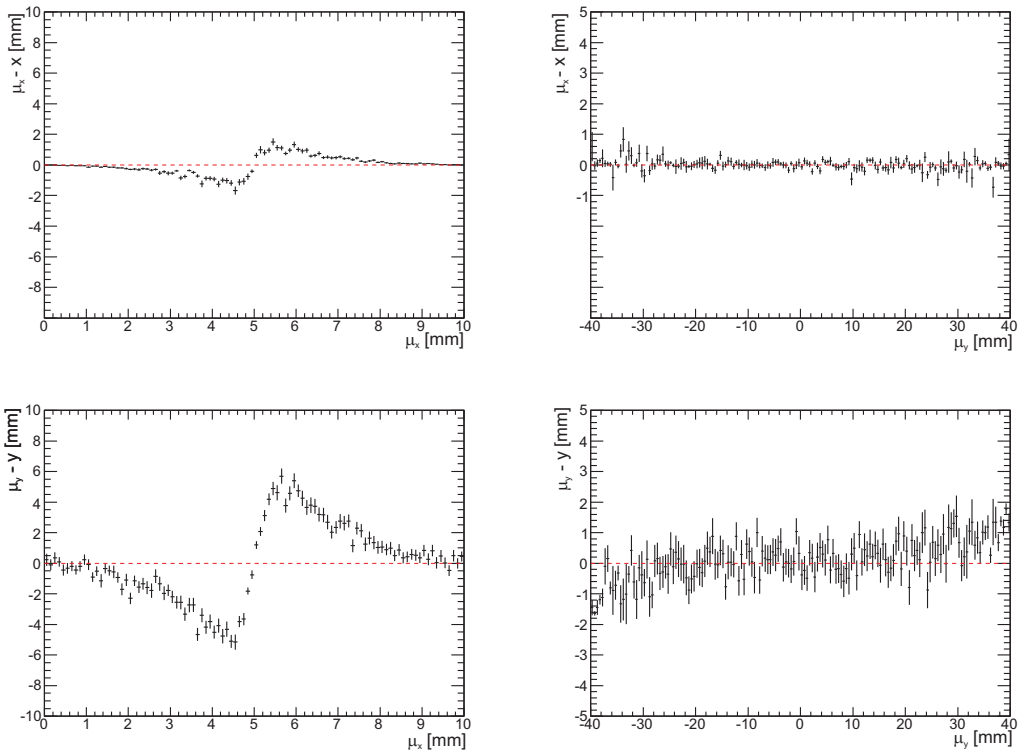

Fig. A.1: Relative position errors for floating point accuracy and pad width $W = 10\,\text{mm}$:
Left up: $(\mu_x - x)$ plotted versus μ_x; **Right up**: $(\mu_x - x)$ plotted versus μ_y;
Left down: $(\mu_y - y)$ plotted versus μ_x; **Right down**: $(\mu_y - y)$ plotted versus μ_y.

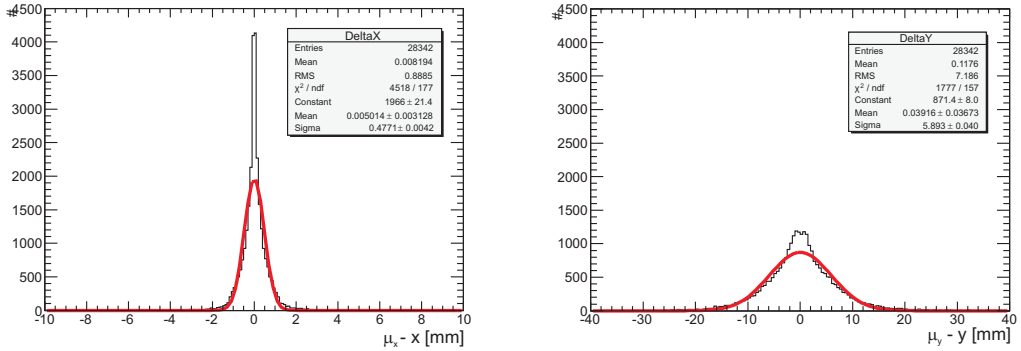

Fig. A.2: Position resolution for floating point accuracy and pad width $W = 10\,\text{mm}$:
Left: x-coordinate; **Right**: y-coordinate

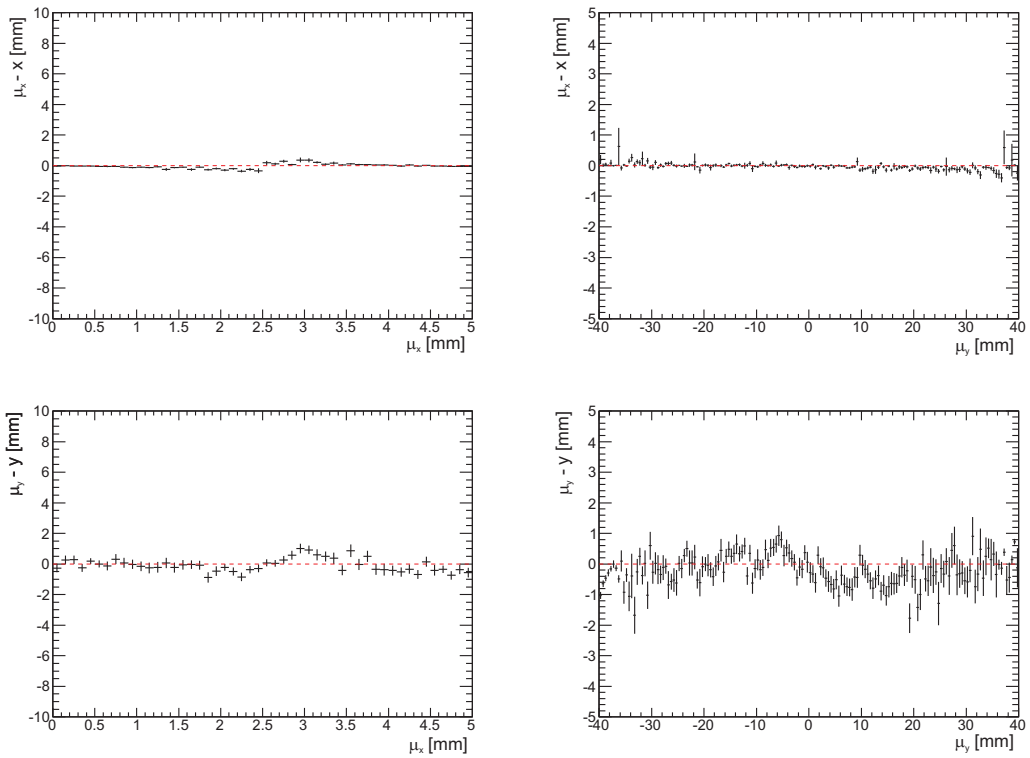

Fig. A.3: Relative position errors for floating point accuracy and pad width $W = 5\,\text{mm}$:
Left up: $(\mu_x - x)$ plotted versus μ_x; **Right up**: $(\mu_x - x)$ plotted versus μ_y;
Left down: $(\mu_y - y)$ plotted versus μ_x; **Right down**: $(\mu_y - y)$ plotted versus μ_y.

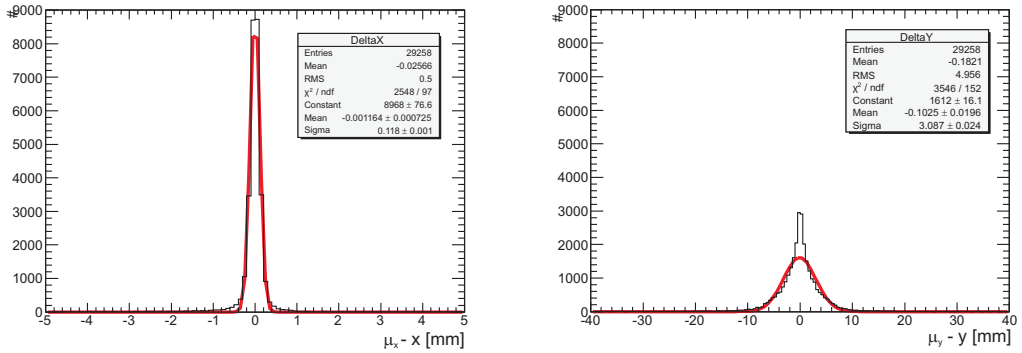

Fig. A.4: Position resolution for floating point accuracy and pad width $W = 5\,\text{mm}$:
Left: x-coordinate; **Right**: y-coordinate

A.2.2. Position Resolution (x,y) Simulation, Relativ Position Error for a Realistic Noise Level and 1024 Bit ADC Digitalization

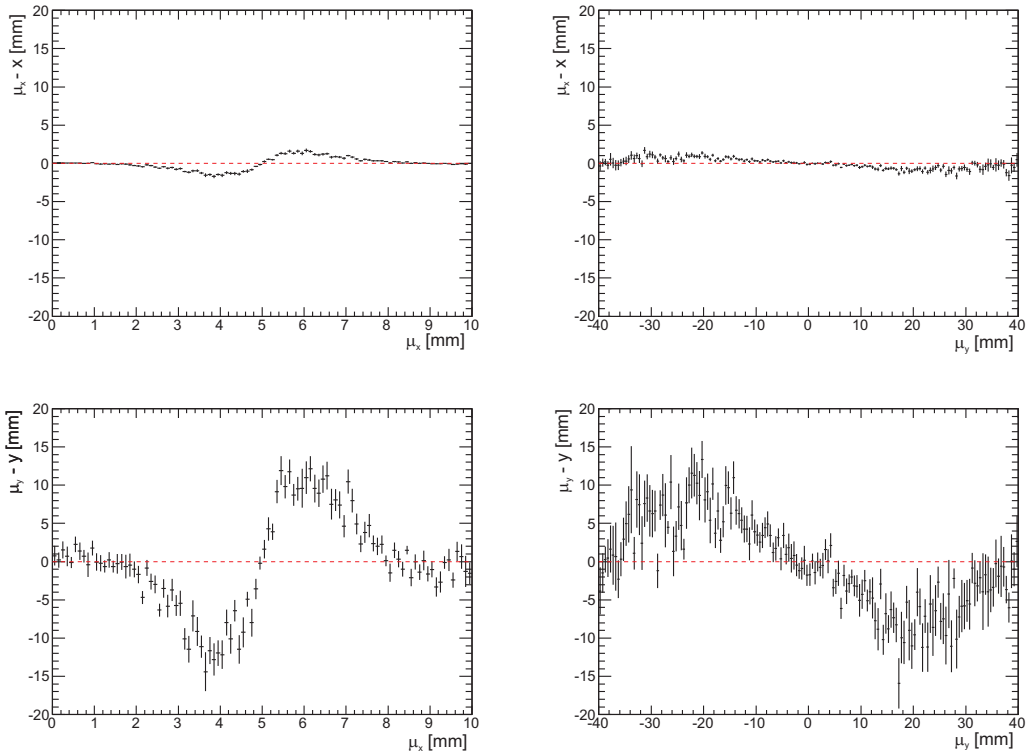

Fig. A.5: Relative position errors for 1024 Bit ADC Signal, last 10 Bits with 2 Bit gaussian distributed noise and pad width $W = 10\,\text{mm}$:
Left up: $(\mu_x - x)$ plotted versus μ_x; **Right up**: $(\mu_x - x)$ plotted versus μ_y;
Left down: $(\mu_y - y)$ plotted versus μ_x; **Right down**: $(\mu_y - y)$ plotted versus μ_y.

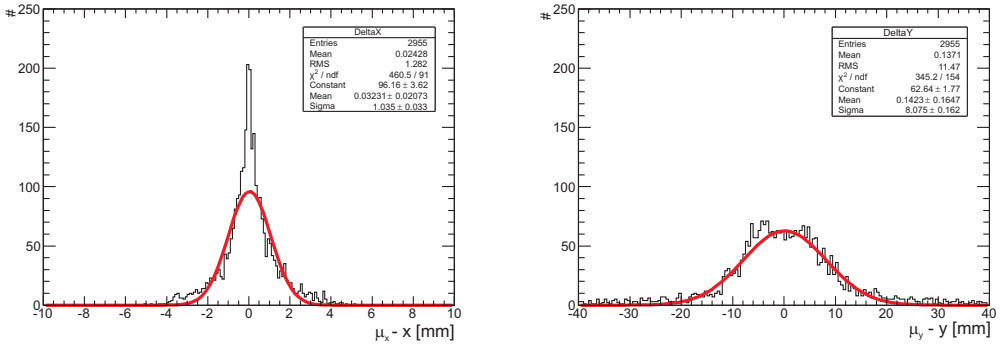

Fig. A.6: Position resolution for 1024 Bit ADC Signal, last 10 Bits with 2 Bit gaussian distributed noise, pad width $W = 10\,\text{mm}$: **Left**: x-coordinate; **Right** y-coordinate

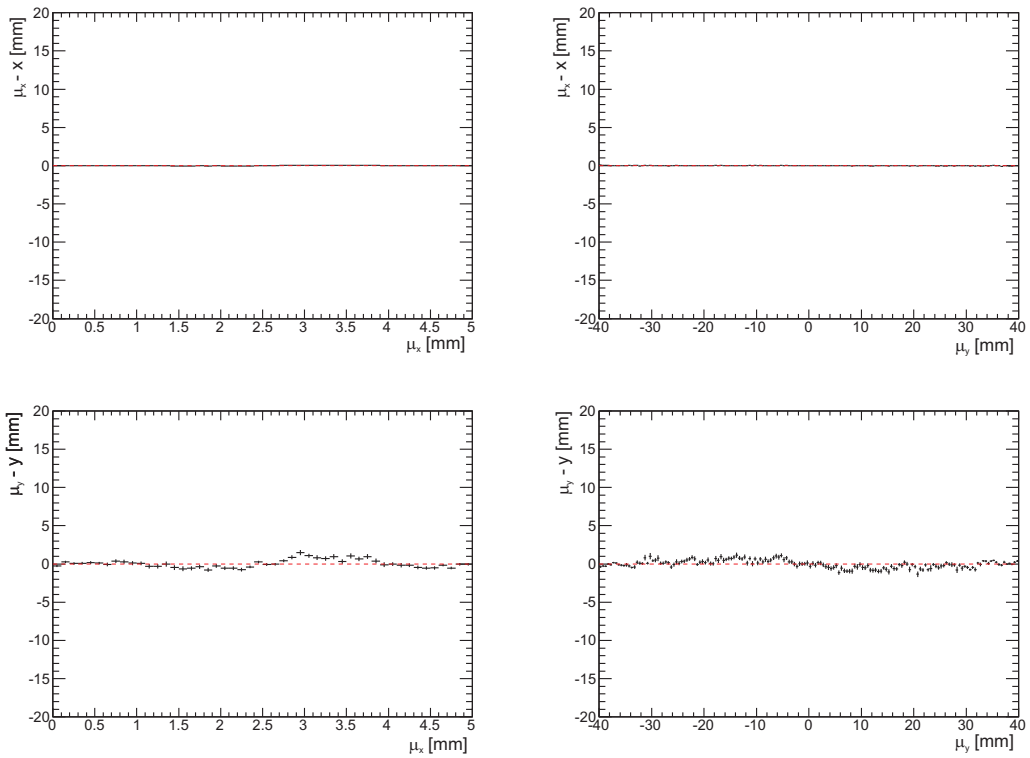

Fig. A.7: Relative position errors for 1024 Bit ADC Signal, last 10 Bits with 2 Bit gaussian distributed noise and pad width $W = 5\,\mathrm{mm}$:
Left up: $(\mu_x - x)$ plotted versus μ_x; **Right up**: $(\mu_x - x)$ plotted versus μ_y;
Left down: $(\mu_y - y)$ plotted versus μ_x; **Right down**: $(\mu_y - y)$ plotted versus μ_y.

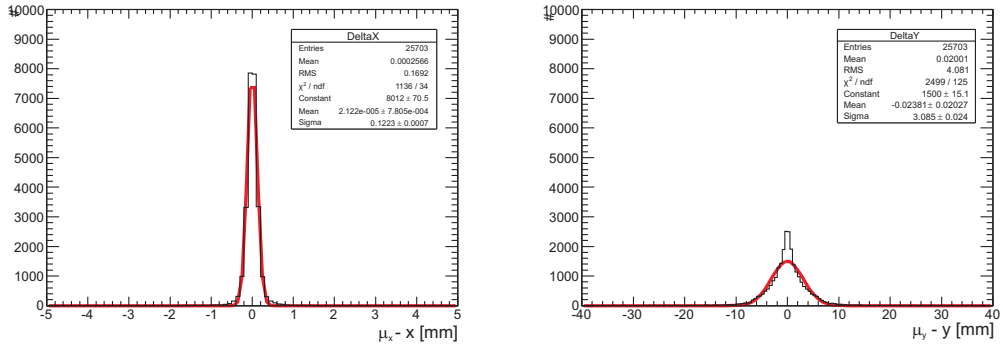

Fig. A.8: Position resolution for 1024 Bit ADC Signal, last 10 Bits with 2 Bit gaussian distributed noise, pad width $W = 5\,\mathrm{mm}$: **Left**: x-coordinate; **Right** y-coordinate

A.2.3. Cluster Position Reconstruction Methods

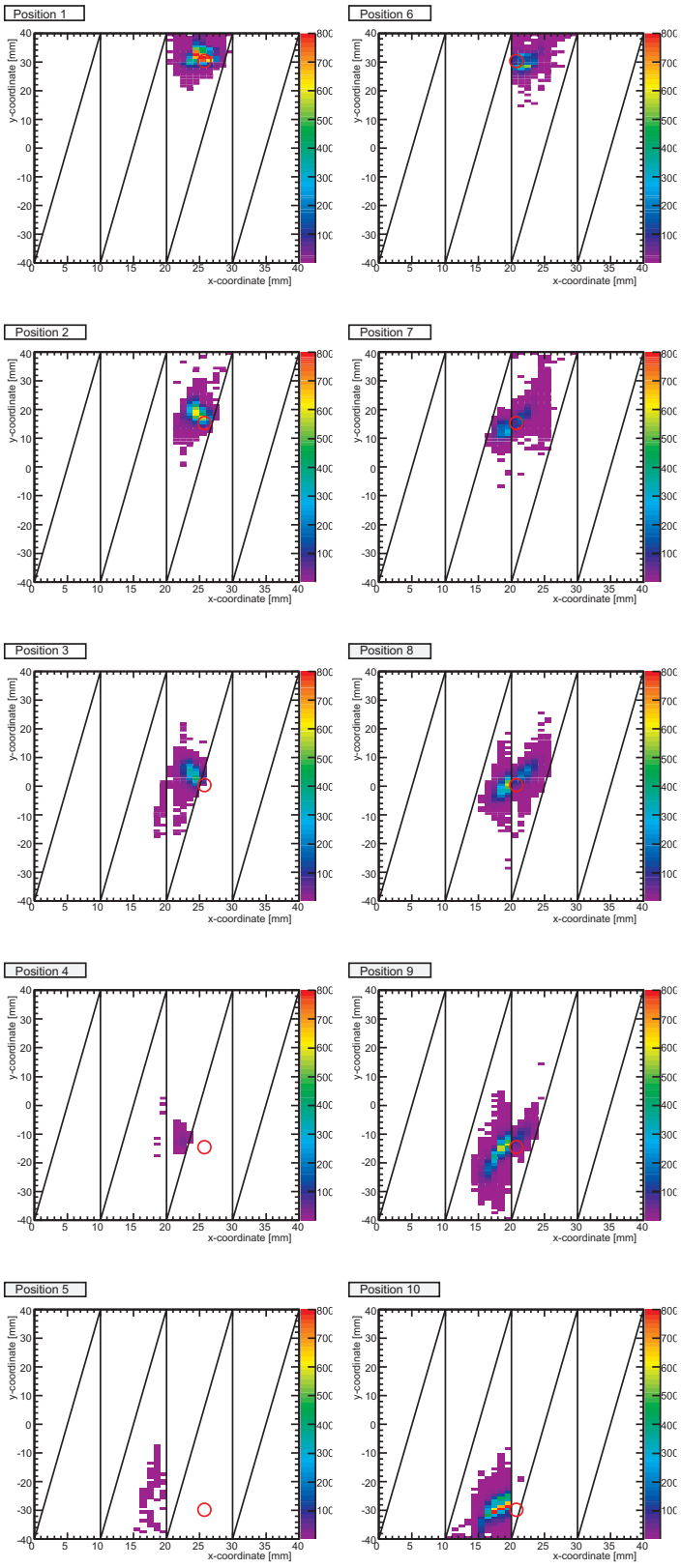

Fig. A.9: Cluster position reconstruction using weighted displacement for collimator positions 1 - 10
○: Theoretical collimator position.

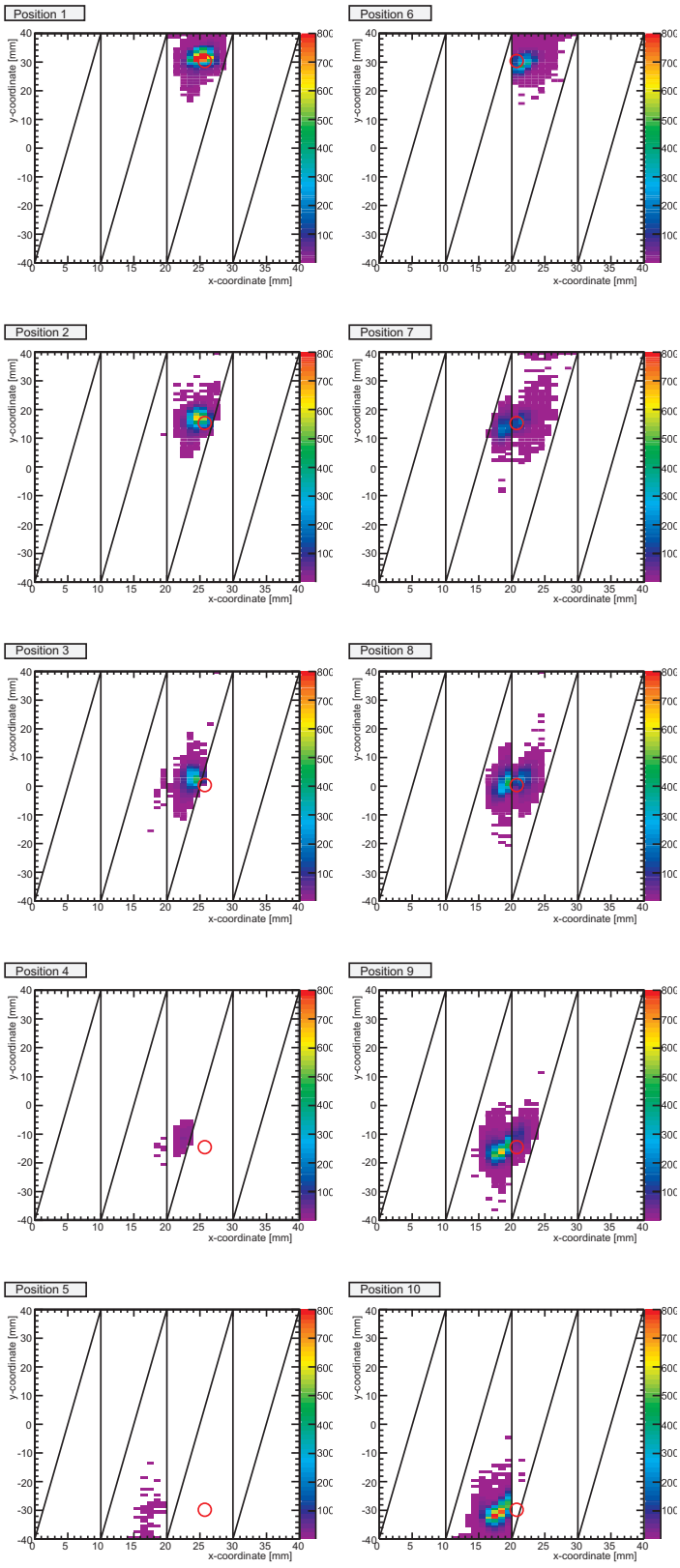

Fig. A.10: Cluster position reconstruction using unweighted displacement for collimator positions 1 - 10
○: Theoretical collimator position.

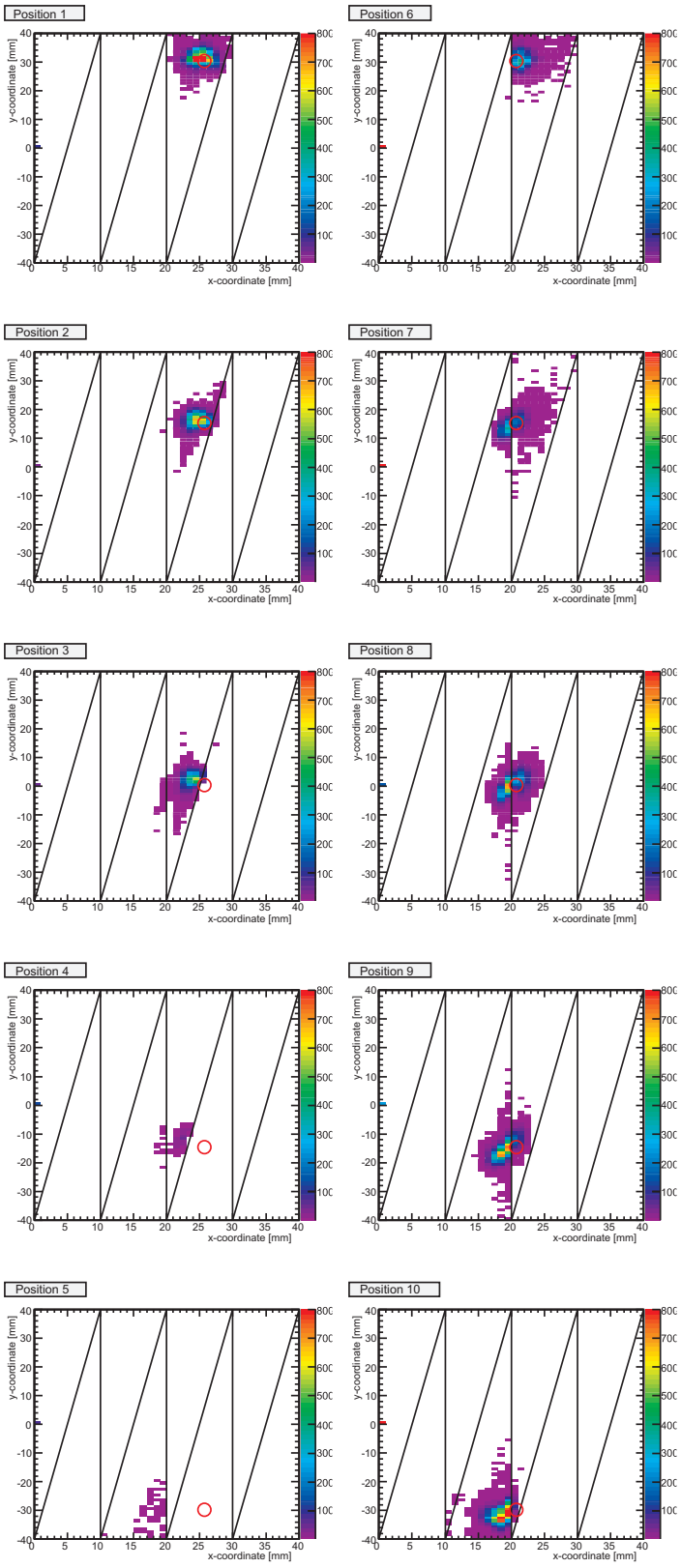

Fig. A.11: Cluster position reconstruction using Equation 2.28 for collimator positions 1 - 10
○: Theoretical collimator position.

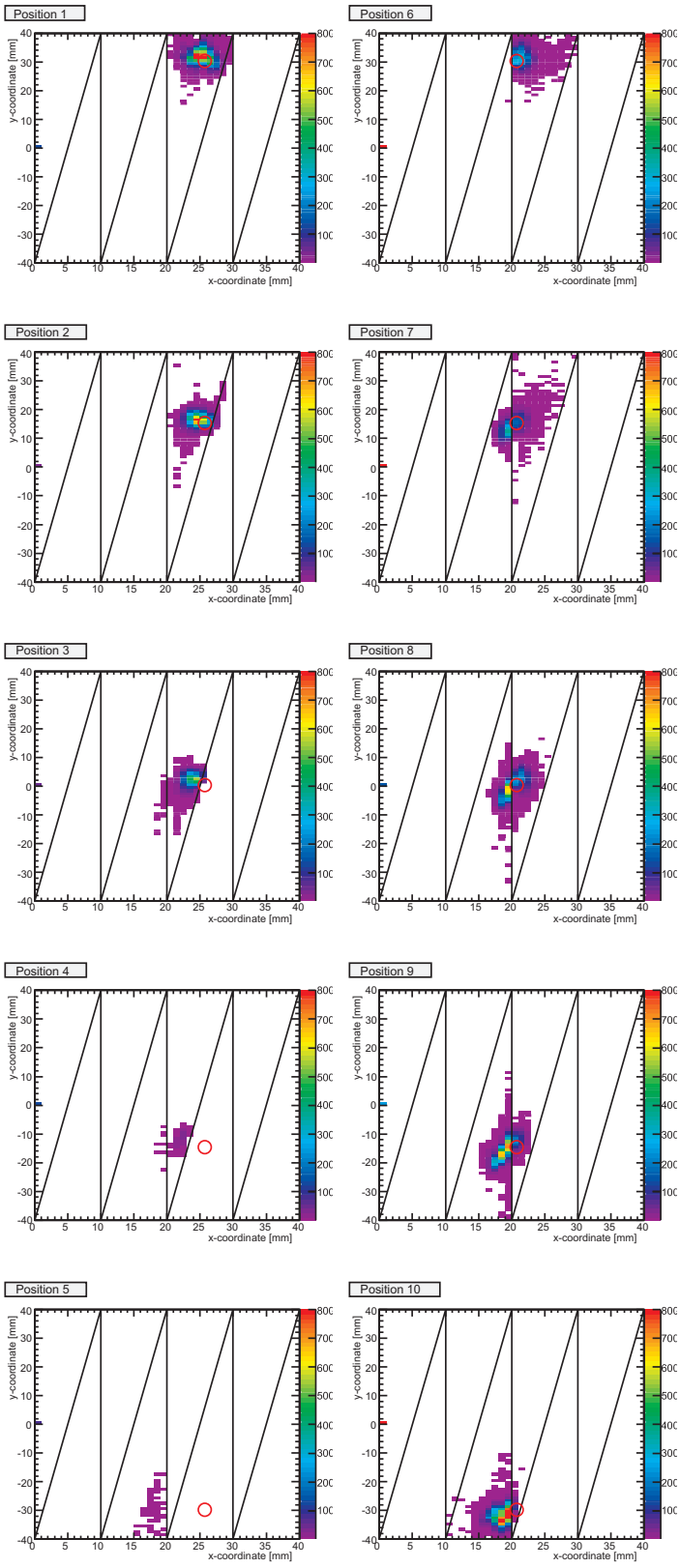

Fig. A.12: Cluster position reconstruction using Equation 2.29 for collimator positions 1 - 10
○: Theoretical collimator position.

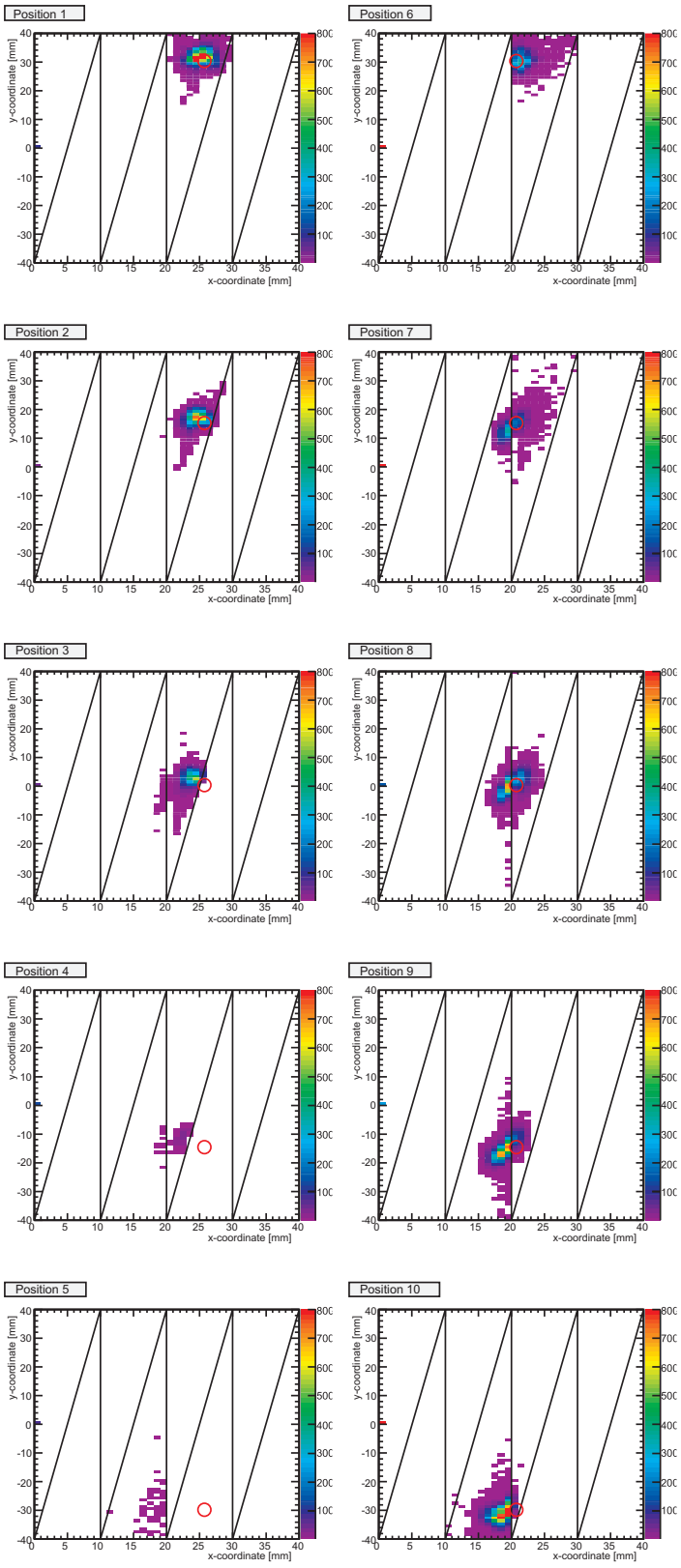

Fig. A.13: Cluster position reconstruction using Equation 2.30 for collimator positions 1 - 10
○: Theoretical collimator position.

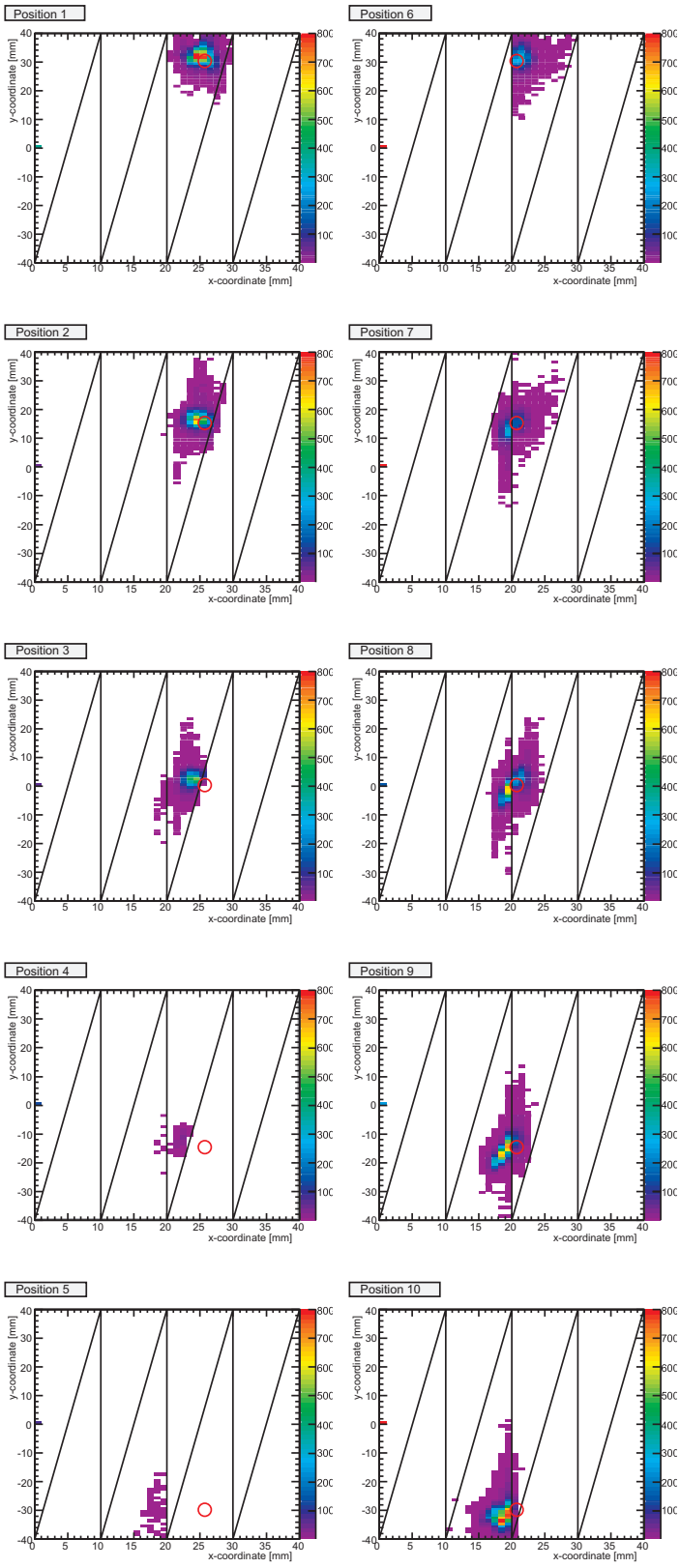

Fig. A.14: Cluster position reconstruction using Equation 2.31 for collimator positions 1 - 10
○: Theoretical collimator position.

B. Blueprints and Photographs

B.1. Real-Size Prototype

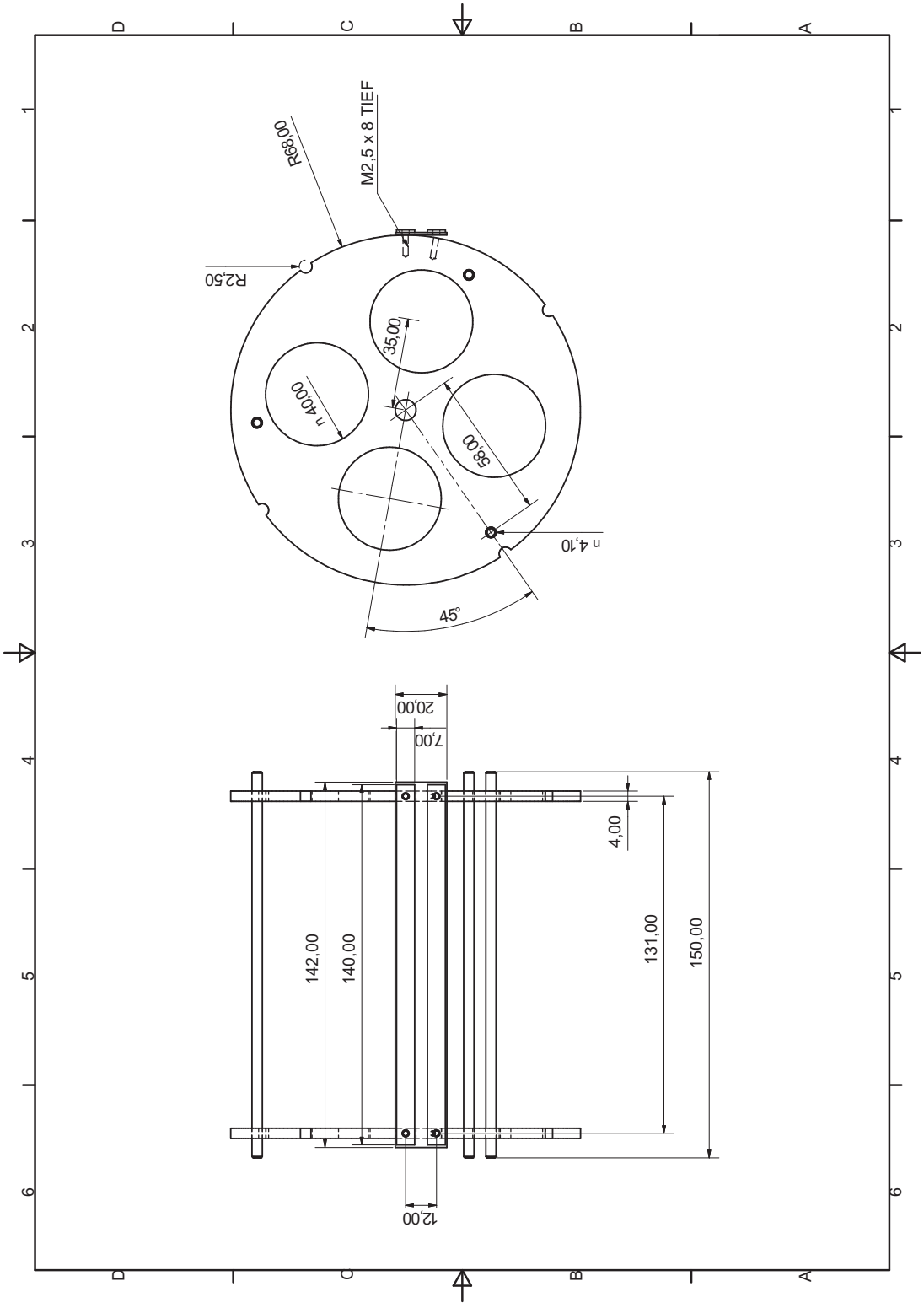

Fig. B.1: Blue print of the castor frame [Hac09]

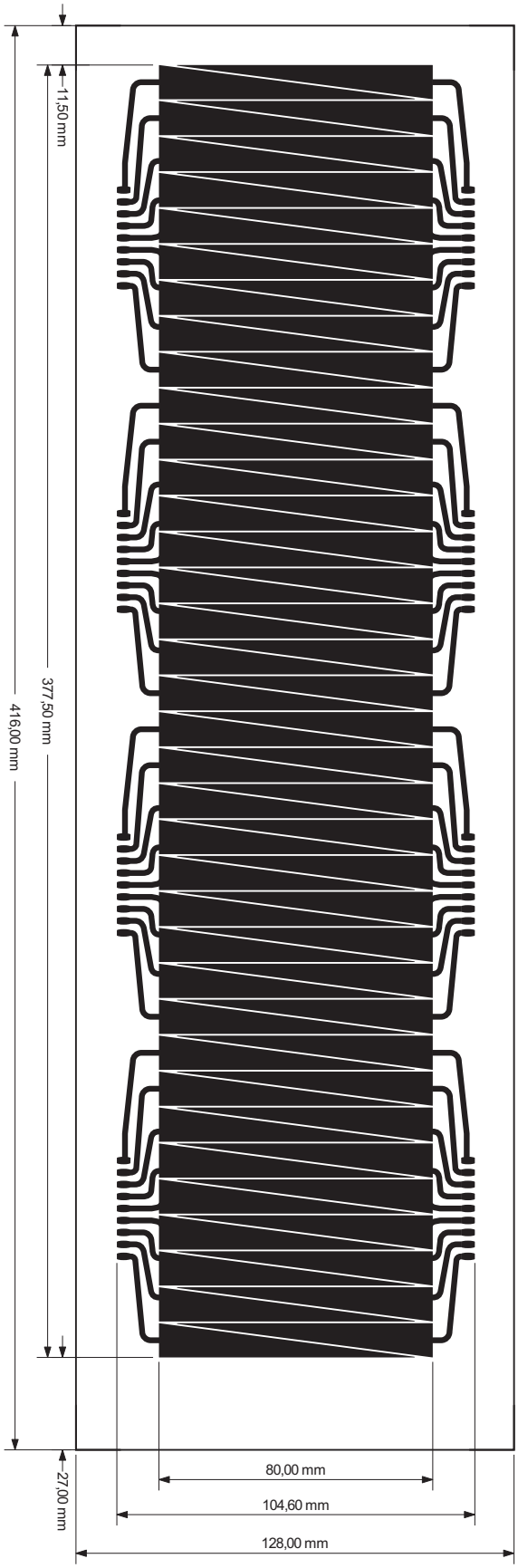

Fig. B.2: Pad structure [Hei09]

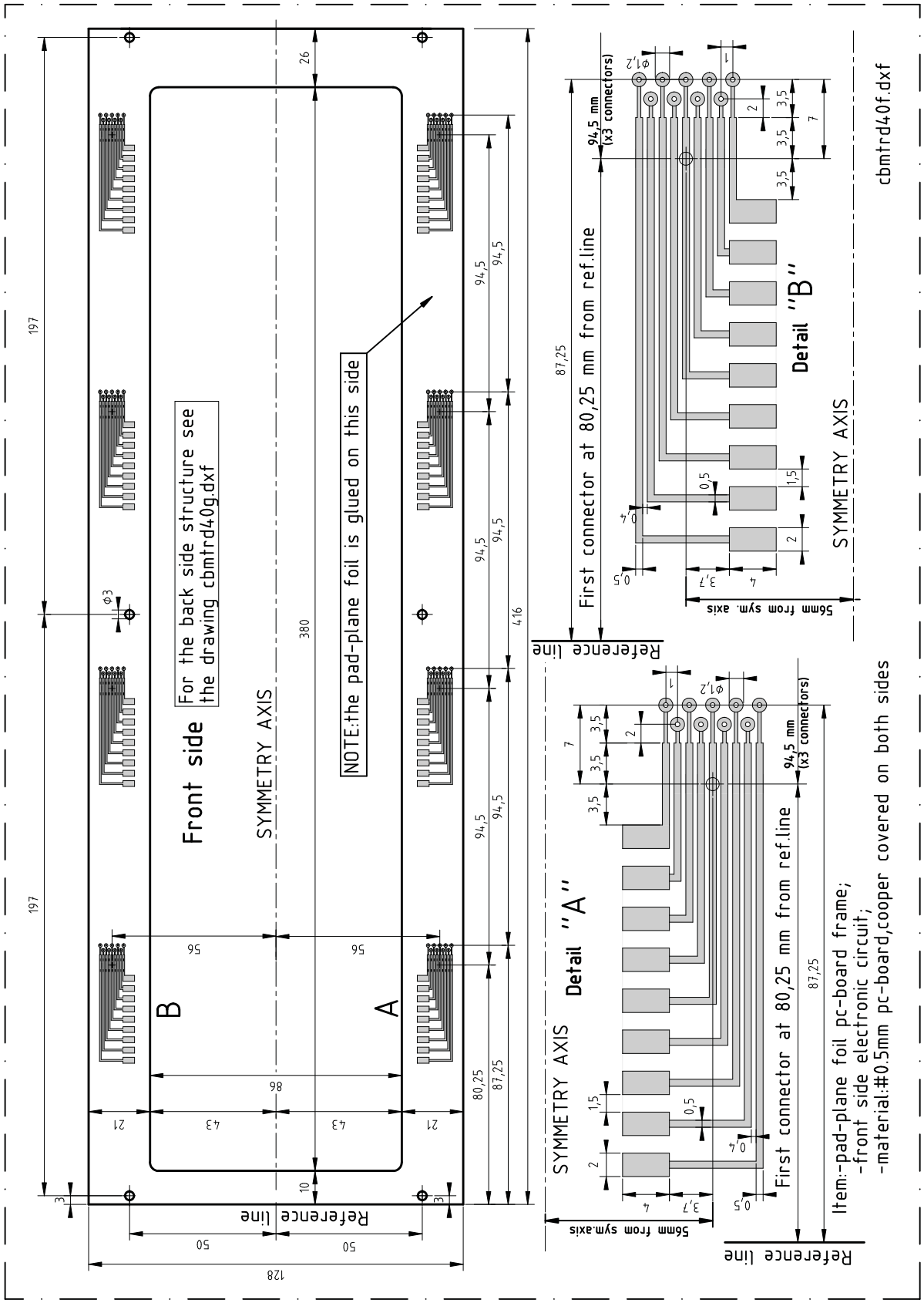

Fig. B.3: Front view of the detector [Sim09]

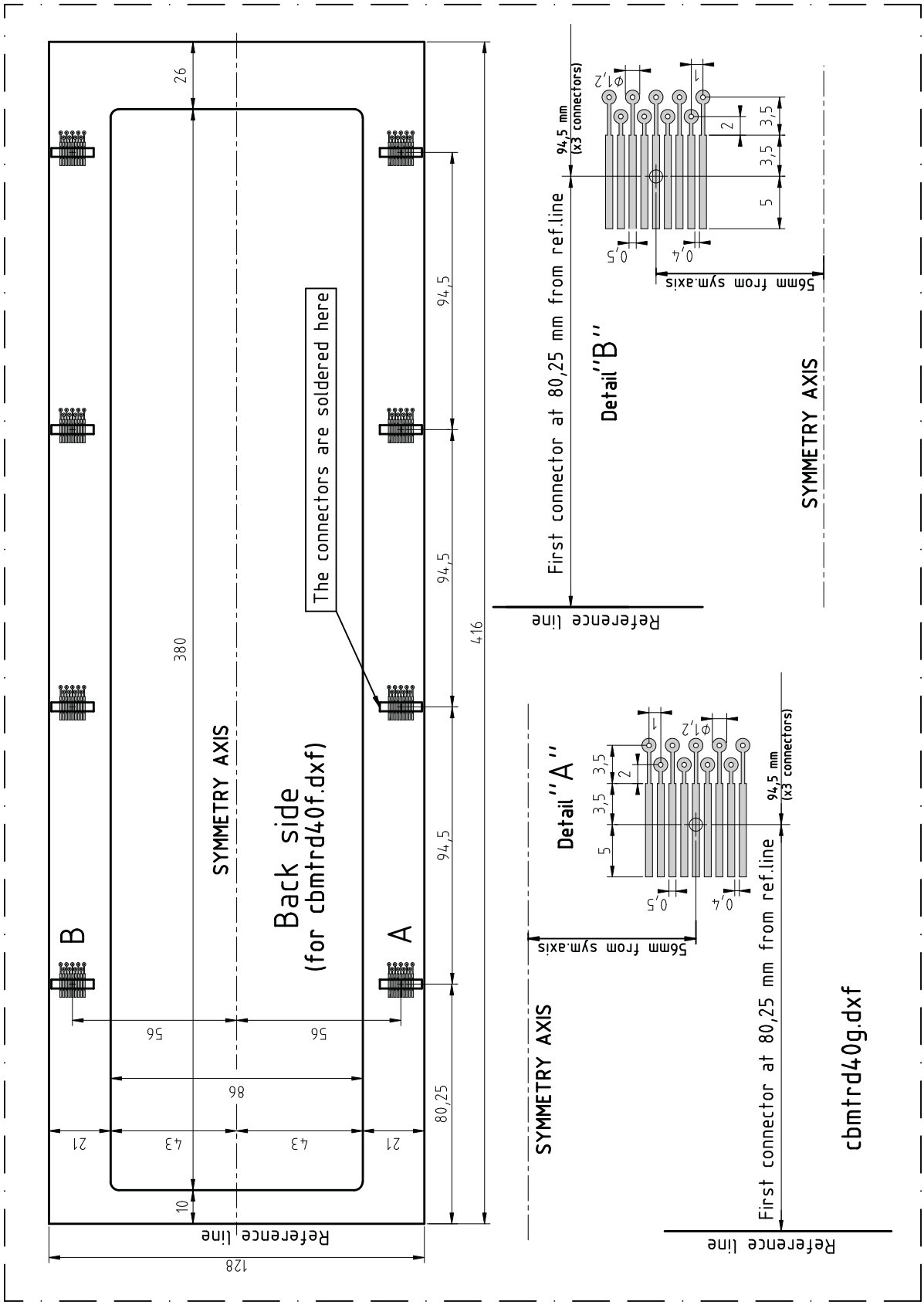

Fig. B.4: Back view of the detector [Sim09]

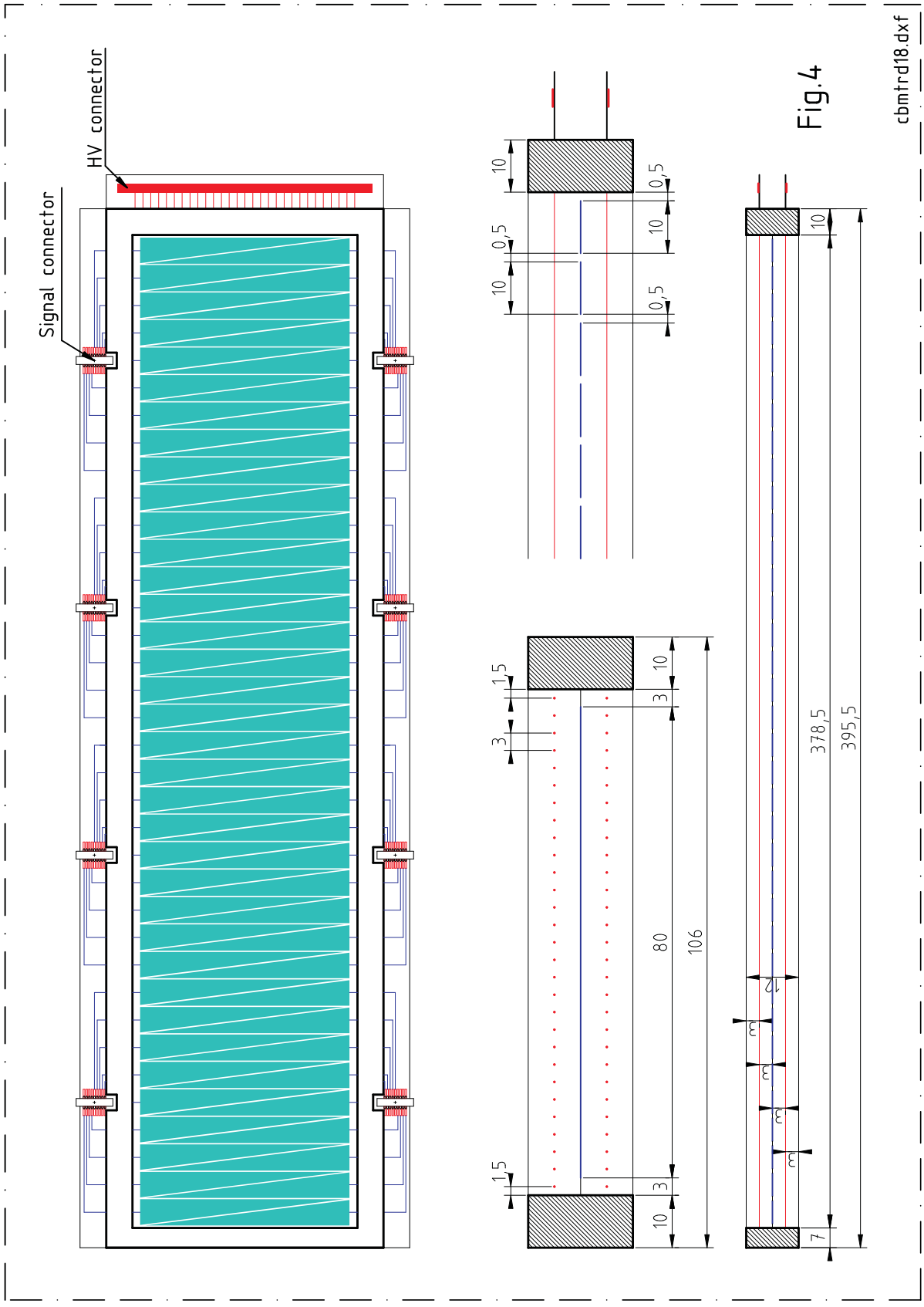

Fig. B.5: Detector with pad plane [Sim09]

B.1.1. Different Production States of the TRD Chamber

Fig. B.6: Anode plane before gluing on the central kapton-alu plane [MP09]

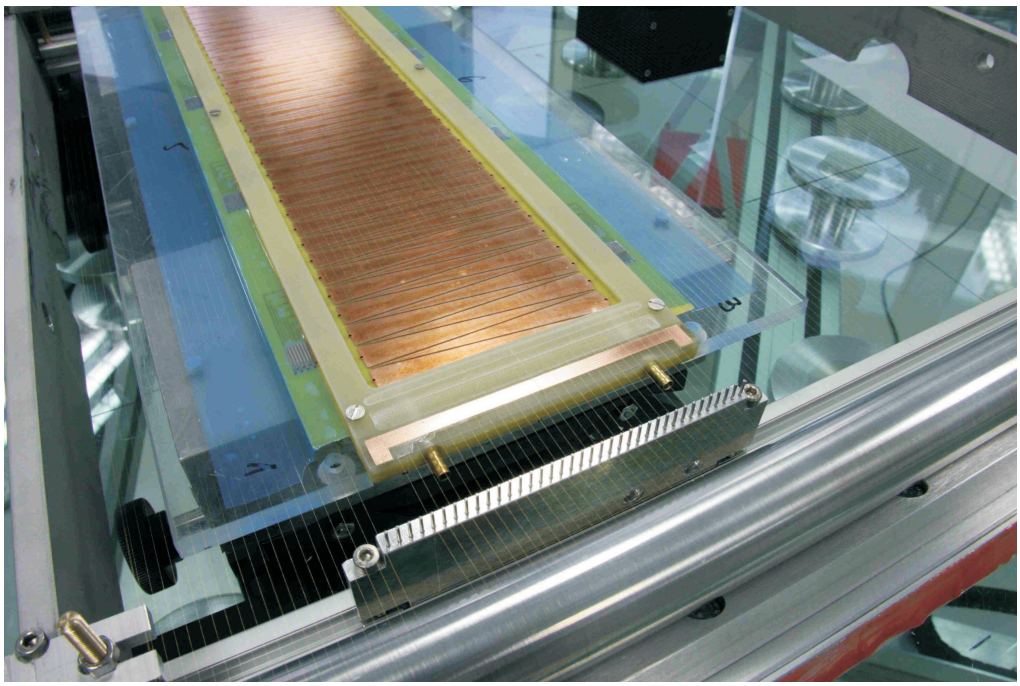

Fig. B.7: Gluing the anode plane on the PCB readout central pad-plane [MP09]

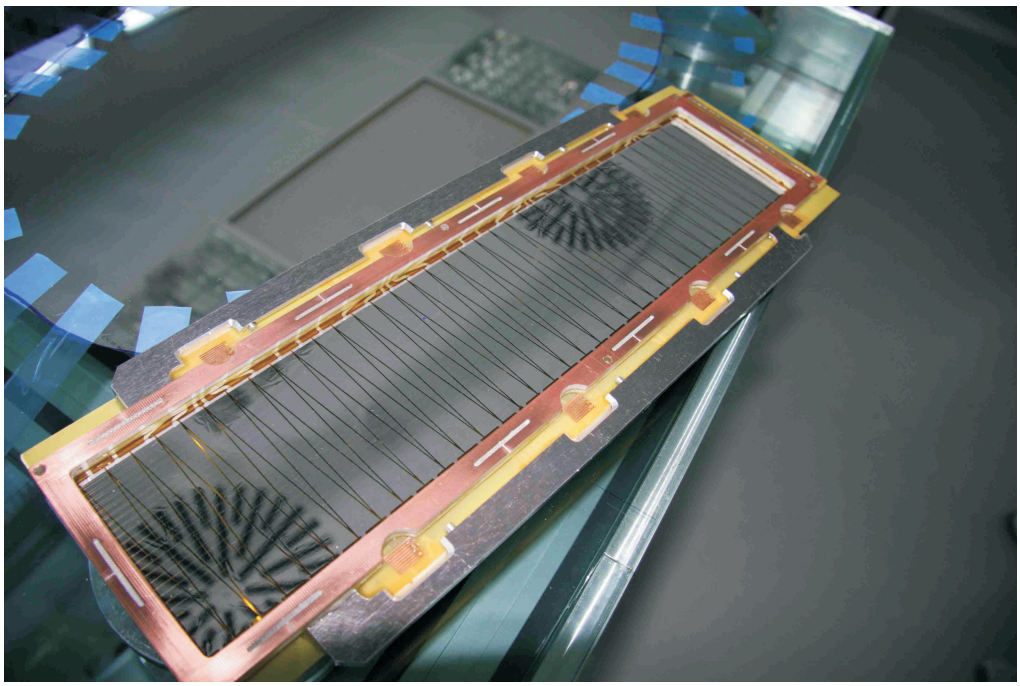

Fig. B.8: After gluing, the same on the other side [MP09]

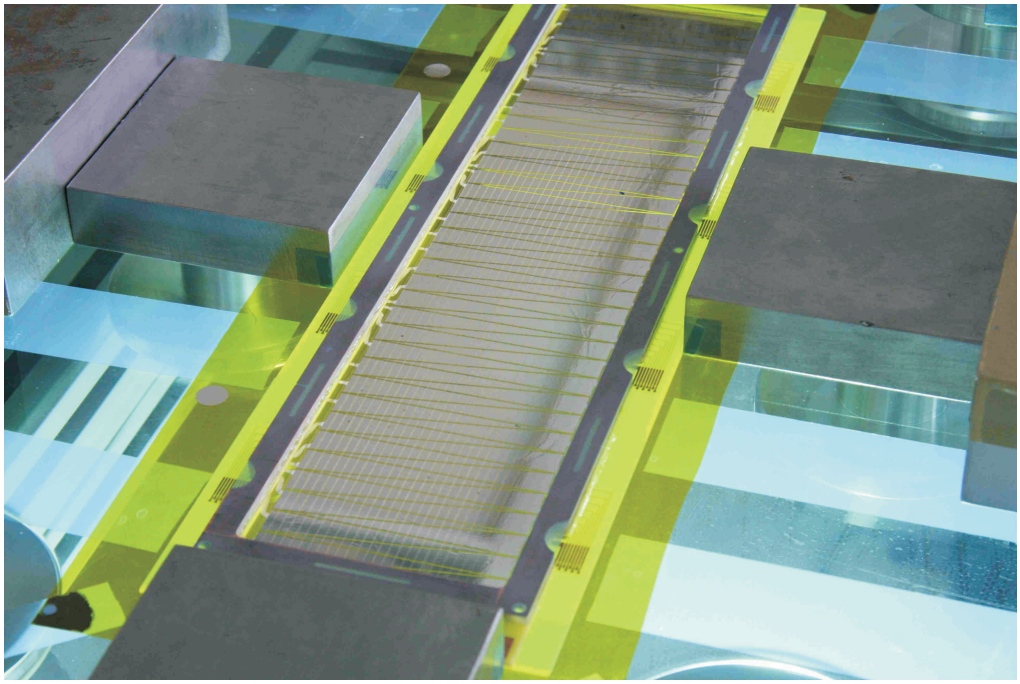

Fig. B.9: Gluing the anode plane on the kapton-alu readout central pad-plane [MP09]

C. Run Summary of the Small Prototype Test Beam 2006 @ GSI

Gray-colored runs are used for histograms shown within this thesis.

Tab. C.1: Run summary of the small prototype test beam 2006 @ GSI [Wil09]

run	U[V]	p[GeV/c]		Spill[s]	Size[MB]	Comments
17	1800	1.0	+	10	372	85% Xe, 15% CO_2
18	1600	1.0	+	10	224	90% Xe, 10% CO_2
19	1800	1.0	+	10	40	short run
20	1800	1.0	+	10		aborted (?)
21	1700	1.0	+	10	249	85% Xe, 15% CO_2
22	1700	1.0	+	10	201	threshold for Pbgl increased
23	1700	1.0	+	10	230	Pbgl off from trigger
24	1700	1.5(?)	+	10	100	momentum (?)
25	1700	1.5(?)	+	10		
26	1700	2.0	+	10	285	
27	1700	1.5	+	10		
28					48	
29	1700	1.5	+	10	203	
30	1700	1.5	+	10		
31	1700	1.5	+	10	203	
32	1700	1.5	+	10	251	
33	1700	1.5	+	5	225	
34	1700	1.5	+	5	250	
35	1700	1.5	+	5	204	Cherenkov online
36	1700	1.5	+	5	174	aborted
37	1700	1.5	+	2	516	
38	0	1.5	+	2		only Cher + Szintillators (?)
39	1700	1.5	+	2		10 MHz clock out
40	1700	1.5	-	10	118	switch to negatives
41	1700	1.5	-	10	207	
42	1700	1.5	-	4(?)	200	foil radiators put in front of B1
43	1700	1.5	-	4	120	foil radiator back to GSI1
44	1700	1.5	-	4	263	Dubna changed HV
45	1700	1.5	-	4	46	
46	1700	1.5	-	4		
47	1800	1.5	-	4	202	
48	1800	1.5	-	4	202	
49	1800	1.0	-	4	170	Pbgl threshold → 60mV, TDC implemented
50	1800	1.0	-	4	200	Pbgl threshold → 70mV
51	1800	1.0	-	4	200	
52	1800	1.0	+	2	200	switch back to positives

continued on next page

continued from previous page

run	U[V]	p[GeV/c]		Spill[s]	Size[MB]	Comments
53	1800	1.0	+	2	135	low rate
54	1800	1.5	+	2	217	low rate
55	1800	1.5	+	2	163	low rate
56	1800	1.5	+	1	129	Pbgl threshold → 120 mV
57	1800	1.5	+	1	241	
58	1800	1.5	+	10	146	
59	1800	1.5	+	10		S2 and Pbgl realigned
60	1800	1.5	+	10	14	
61	1800	1.5	+	1	200	
62	1800	1.5	+	1		noticed different gain for B1 and M1
63	1800	1.5	+	1	290	beam not stable; removed Si
64	1800	1.5	+	1	229	Dubna change HV
65	1800	1.5	+	2	362	
66	1800	1.5	+	5	400	Si back to beam
67	1800	1.5	+	0.7	410	Si removed
68	1800	1.5	+	0.5	363	HV of B1 not stable; problem with ion source
69	1800	1.5	+	0.5		very low intensity
70	1800	1.5	+	0.5		rate vary very strong
71	1800	1.5	+	4	98	M1 no radiator
72	1800	1.5	+	4	157	beam fluctuations; Pbgl off from trigger
73	1800	2.0	+	10	225	
74	1800	2.0	+	10	200	
75	1800	2.0	+	5	202	
76	1800	2.0	+	5	159	low rate
77	1800	2.0	+	5	210	
78	1800	2.0	+	2	198	
79	1800	2.0	+	2	202	
80	1600	2.0	+	2	201	change voltages
81	1600	2.0	+	2	200	
82	1600	2.0	+	5	200	
83	1600	2.0	+	5	206	
84	1600	2.0	+	10	201	
85	1600	2.0	+	10	210	
86	1600	2.0	+	2	203	Si off from DAQ
87	1700	2.0	+	2	94	90% Xe, 10% CO_2; low rate
88	1700	2.0	+	2	200	Dubna change HV
89	1700	2.0	+	2	200	
90	1700	2.0	+	5	201	
91	1700	2.0	+	5	212	
92	1700	2.0	+	10	201	

continued on next page

continued from previous page

run	U[V]	p[GeV/c]		Spill[s]	Size[MB]	Comments
93	1700	2.0	+	10	205	
94	1500	2.0	+	10		Test file for HV (B1,M1,B2)
95	1550	2.0	+	10	204	change HV
96	1550	2.0	+	10	204	
97	1550	2.0	+	5	201	
98	1550	2.0	+	5	201	
99	1550	2.0	+	2	214	
100	1550	2.0	+	2	201	
101	1650	2.0	+	2	555	change HV
102	1650	2.0	+	2	214	
103	1650	2.0	+	2		
104	1650	2.0	+	2	204	
105	1650	2.0	+	2	216	
106	1650	2.0	+	10	219	
107	1650	2.0	+	10	222	
108	1650	2.0	+	10	192	80% Xe, 20% CO_2
109	1650	2.0	+	5	205	
110	1650	2.0	+	5	200	
111	1650	2.0	+	2	200	
112	1850	2.0	+	2	50	HV on GSI?; change HV
113	1850	2.0	+	2	239	
114	1850	2.0	+	2	200	
115	1650	2.0	+	2		change HV
116	1650	2.0	+	2		
117	1850	2.0	+	5	251	change HV
118	1850	2.0	+	5	200	
119	1850	2.0	+	10		
120	1850	2.0	+	10	340	
121	1800	2.0	+	10	133	change angles to 30 deg
122	1800	2.0	+	10	258	
123	1800	2.0	+	10	187	
124	1800	2.0	+	2	258	
125	1800	2.0	+	2	204	remove B1 and B2; GSI at 20 deg
126	1800	2.0	+	2	204	
127	1800	2.0	+	10	214	
128	1800	2.0	+	10	200	
129	1800	2.0	+	2	211	GSI at 10 deg
130	1800	2.0	+	2	200	
131	1800	2.0	+	10	207	
132	1800	2.0	+	10	216	
133	1800	1.5	+	10	210	GSI back to 0 deg; start with GEM scan

continued on next page

continued from previous page

run	U[V]	p[GeV/c]		Spill[s]	Size[MB]	Comments
134	1800	1.5	+	10	204	
135	1800	1.5	+	10	208	
136	1800	1.5	+	5		
137	1800	1.5	+	5	200	
138	1800	1.5	+	5	226	
139	1800	1.5	+	5	200	
140	1800	1.5	+	5	206	
141	1800	1.5	+	5	226	
142	1800	1.5	+	5	203	
143	1800	1.5	+	5	203	
144	1800	1.5	+	5	218	
145	1800	1.5	+	5	204	
146	1800	1.5	+	5	201	
147	1800	1.5	+	10	207	
148	1800	1.5	+	10	205	
149	1800	1.5	+	10	205	
150	1800	1.5	+	10	203	
151	1800	1.5	+	10	201	
152	1800	1.5	+	10	150	
153	1800	1.5	+	2	513	end GEM scan
154	1800	1.5	+	2	266	
155	1800	1.5	+	2		Pbgl back in trigger;
156	1600	2.0	+	10		85% Ar, 15% CO_2; remove Pbgl from trigger; remove radiators
157	1610	2.0	+	10	278	
158	1610	2.0	+	10	244	
159	1610	2.0	+	5	265	low intensity
160	1610	2.0	+	5	320	
161	1610	2.0	+	2	206	
162	1610	2.0	+	2	204	
163	1610	2.0	+	2	234	
164	1700	1.5	+	2	19	85% Xe, 15% CO_2; M1 0 deg, M1 with foil radiator
165	1700	1.5	+	0.5	87	
166	1700	1.5	+	0.5	202	
167	1700	1.5	+	0.5	205	
168	1700	1.5	+	0.75	205	
169	1700	1.5	+	0.75	205	
170	1700	1.5	+	0.75	215	

References

[A+01] A. Andronic et al. Prototype Tests for the ALICE TRD. *IEEE Trans.Nucl.Sci.*, 48:1259–1264, 2001.

[A+08] C. Amsler et al. Review of Particle Physics. *Phys. Lett.*, B667:1, 2008.

[BR94] W. Blum and L. Rolandi. *Particle Detection with Drift Chambers*. Springer, 1994.

[CBM08] CBM. CBM Progress Report 2008. Technical report, CBM, 2008.

[EG+79] H. Okuno P. Semenza E. Gatti, A. Longoni et al. Optimum Geometry for Strip Cathodes on Grids in MWPC for Avalanche Localization Along the Anode Wires. *Nucl. Instr. & Meth.*, 163:83–92, 1979.

[Fab80] H. G. Fabjan, C. W.; Fischer. Particle Detectors. *Reports on Progress in Physics*, 43:1003–1063, 1980.

[FK02] Z. Fodor and D. Katz. Lattice Determination of the Critical Point of QCD at Finite T and μ. *JHEP*, 03:014, 2002.

[FK04] Z. Fodor and D. Katz. Critical Point of QCD at Finite T and μ, Lattice Results for Physical Quark Masses. *JHEP Institute of Physics Publishing for SISSA/ISAS*, 04, 2004.

[Gre00] D. Green. *The Physics of Particle Detectors*. Cambridge University Press, 2000.

[Gru99] C. Grupen. Physics of Particle Detection, 1999.

[Gru09] T. Grund. SEM picture by T.Grund. Private communications, Institut für Planetologie Westfälische Wilhelms-Universität Münster, 2009.

[H+09] B. Henke et al. X-ray Interactions: Photoabsorption, Scattering, Transmission, and Reflection at E=50-30000 eV, Z=1-92, Atomic Data and Nuclear Data Tables Vol. 54 (no.2), 181-342, 1993. `http://henke.lbl.gov/optical_constants`, December 2009.

[Hac09] G. Hackmann. Drawing by G. Hackmann. Private communications, Institut für Kernphysik Westfälische Wilhelms-Universität Münster, 2009.

[Hei09] N. Heine. Drawing by N. Heine. Private communications, Institut für Kernphysik Westfälische Wilhelms-Universität Münster, 2009.

[K+08] A. Kiseleva et al. Di-Muon Measurements with the CBM Experiment at FAIR. *Proceedings of Quark Matter 2008*, 2008.

[Kal06] A. Kalweit. Untersuchung von Hochrateneffekten in Übergangsstrahlungsdetektoren (TRDs) für das CBM-Experiment, 2006.

[Kar99] F. Karsch. Deconfinement and Chiral Symmetry Restoration. *arXiv:hep-lat/9903031v2*, 1999.

[KB05] C. Klein-Bösing. *Production of Neutral Pions and Direct Photons in Ultra-Relativistic Au+Au Collisions*. PhD thesis, Institut für Kernphysik, Westfälische Wilhelms-Universität Münster, 2005.

[KB09] M. Klein-Bösing. *Development of a Transition Radiation Detector and Reconstruction of Photon Conversions in the CBM Experiment*. PhD thesis, Institut für Kernphysik, Westfälische Wilhelms-Universität Münster, 2009.

[Leo87] W. Leo. *Techniques for Nuclear and Particle Physics Experiments*. Springer-Verlag, 1987.

[Mat88] E. Mathieson. Cathode Charge Distributions in Multiwire Chambers. *Nuclear Instruments and Methods in Physics Research A270*, pages 602–603, 1988.

[MM85] T. Sakae H. Kametani H. Ijiri T. Shintake M. Matoba, T. Hirose. Three Dimensional Monte Carlo Simulation of the Electron Avalanche Around an Anode Wire of a Proportional Counter. *IEEE Trans. on Nucl. Science*, NS-32 1:541–544, 1985.

[MP09] M. Petrovici M. Petris. Photo by M. Petris. Private communications, IFIN-HH Bucharest, Romania, 2009.

[RCH04] Xin-Nian Wang R. C. Hwa. *Quark-Gluon Plasma 3*. World Scientific Pub Co, 2004.

[Sau77] F. Sauli. Principles of Operation of Multiwire Proportional and Drift Chambers, 1977. Lectures given in the Academic Training Programme of CERN, 1975- 1976.

[Sen06] P. Senger. The CBM Experiment at FAIR. *Journal of Physics: Conference Series*, 50:357–360, 2006.

[Sen09] P. Senger. Status of the CBM Experiment at FAIR. Technical report, CBM Progress Report, 2008,2009.

[Sim01] H. Simon. The Phase Diagram of QCD. *Contemp. Phys.*, 42:209–225, 2001.

[Sim09] V. Simeon. Drawing by V. Simeon. Private communications, IFIN-HH Bucharest, Romania, 2009.

[VEA00] V. Saveliev V. Egorytchev and S. J. Aplin. Particle Identification via Transition Radiation and Detectors. *Nuclear Instruments and Methods in Physics Research Section A: Accelerators, Spectrometers, Detectors and Associated Equipment*, 453:346–352(7), 2000.

[Wil04] A. Wilk. Elektronen- Pionen- Separation im ALICE TRD, 2004.

[Wil09] A. Wilk. Fast TRD Experiment Logbook - February, 2006. `http://www-linux.gsi.de/~andronic/cbm/trd/06/short_logbook.txt`, Dezember 2009.